

UCSF

UC San Francisco Electronic Theses and Dissertations

Title

Localization and assessment of subcortical white matter pathways with diffusion tensor magnetic resonance imaging

Permalink

<https://escholarship.org/uc/item/4nq1b562>

Author

Berman, Jeffrey Ira

Publication Date

2005

Peer reviewed|Thesis/dissertation

**Localization and Assessment of Subcortical White Matter
Pathways with Diffusion Tensor Magnetic Resonance Imaging**

by

Jeffrey Ira Berman

DISSERTATION

Submitted in partial satisfaction of the requirements for the degree of

DOCTOR OF PHILOSOPHY

in

BIOENGINEERING

in the

GRADUATE DIVISIONS

of the

UNIVERSITY OF CALIFORNIA SAN FRANCISCO

and

UNIVERSITY OF CALIFORNIA BERKELEY



Date

University Librarian

Degree conferred:.....

Copyright 2005

by

Jeffrey Ira Berman

Acknowledgements

Numerous people were involved with my training and helped me during the completion of this dissertation project. I am extremely grateful to the following people.

Roland Henry, my primary thesis advisor, for his enthusiastic support and guidance. His help has been indispensable.

Daniel Vigneron for his valuable guidance during the entirety of my project and for serving as my qualifying exam committee chair and thesis committee member.

Pratik Mukherjee, Orit Glenn, and Sri Nagarajan for their advice on choosing exciting and important projects.

Mitchel Berger for his incredible support of our efforts to clinically apply my research.

Sharmila Majumdar for her help in navigating graduate school as my academic advisor and thesis committee member.

Jim Barkovich for his advice and support of my research and for serving on my thesis committee.

Joseph McGowan for introducing me to MRI research at the University of Pennsylvania.

Members of my qualifying exam committee, **John Kurhanewicz, Bruce Hasegawa,** and **Marian Diamond**, for their help with planning my thesis project.

SungWon Chung for continuing some of the work in this thesis.

Susanne Honma and Ann Findlay of the biomagnetic imaging laboratory for their help in coordinating our efforts.

SarahJane Taylor for helping the Bioengineering students get the most out of UC San Francisco and UC Berkeley.

Evelyn Proctor and Niles Bruce for their help in operating our scanners.

And most importantly, my **parents** and **brother** for their unending support.

Grant support was provided by the National Institutes of Health (R01 NS40117, R21 NS40382, P50 NS35902, R01 NS46432, and K01 CA76998).

Abstract

Localization and Assessment of Subcortical White Matter Pathways with Diffusion Tensor Magnetic Resonance Imaging

by

Jeffrey Berman

Improved techniques for studying the human brain are necessary for advancing our understanding of brain structure, function, and development. For this dissertation project, I developed magnetic resonance imaging (MRI) tools for studying the brain's white matter and then clinically applied these tools. Diffusion tensor MRI (DTI) is a non-invasive technique that uses the Brownian motion of water to probe the brain's structure and organization. DTI fiber tracking uses the observed pattern of water diffusion to infer axonal connectivity and delineate white matter pathways in three dimensions. This bioengineering thesis project involved acquiring DTI data, implementing a DTI fiber tracking algorithm, performing feasibility and validity studies, performing patient studies, and transitioning DTI fiber tracking into a routinely used surgical planning tool.

A bootstrap based model of the uncertainty in the primary eigenvector's orientation was implemented. Understanding the primary eigenvector's measurement error is important for assessing the accuracy of DTI fiber tracking.

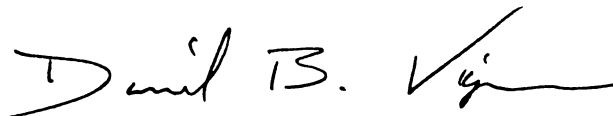
Software tools were developed for generating DTI fiber tracks and making tract-specific measurements. These analysis tools were used in a study of patients with congenital hemiplegia. It was determined that DTI fiber tracking could be used to quantitatively detect structural differences in motor tracts affected by hemiplegia.

Intraoperative cortical and subcortical motor stimulation sites were used to validate the spatial distribution of DTI fiber tracks. These studies showed that DTI fiber tracking could accurately follow the motor tract between functional cortex and the cerebral peduncle in brain tumor patients. Based on these findings, a presurgical DTI fiber tracking protocol was developed and used routinely for surgical planning.

The tools and results from this dissertation were used in a clinical study of white matter development. DTI fiber tracking was performed on premature infants undergoing early phases of white matter maturation. Age related changes in DTI parameters were observed in both the sensory and motor tracts. DTI parameters within different regions of the sensorimotor white matter pathways were observed to be heterogeneous.

The findings of this dissertation project show the scientific and clinical utility of DTI fiber tracking. In the future, improved fiber tracking techniques will enable additional clinical applications.

Approved:

 10/28/05

Daniel Vigneron, Ph.D. Date

Table of Contents

Chapter 1:	Introduction	1
Chapter 2:	Human Brain Basics	5
2.1	Overview	5
2.2	Brain Organization	5
2.2.1	The Neuron	6
2.2.2	White Matter Pathways	7
2.2.3	Functional Organization of the Brain	7
2.3	Populations Included in this Project	10
2.3.1	Congenital Hemiplegia	10
2.3.2	Brain Tumor	10
2.3.3	Premature Infants	11
2.4	Functional Mapping Techniques	12
2.4.1	Intraoperative Stimulation Mapping	13
2.4.2	Magnetic Source Imaging	14
2.5	References	16
Chapter 3:	Diffusion Tensor Imaging	18
3.1	Magnetic Resonance Imaging	18
3.1.1	The Proton	18
3.1.2	Precession and the MR Signal	19
3.1.3	Relaxation	22
3.1.4	Echo Planar Imaging	23
3.2	Diffusion Basics	26
3.2.1	Fundamental Diffusion Equations	26
3.2.2	Water as a Probe of Microstructure	27
3.3	Diffusion Tensor MRI	30
3.3.1	Diffusion Tensor Parameters	33
3.4	Axonal Fiber Tracking with Diffusion Tensor MRI	36
3.4.1	Deterministic Fiber Tracking	37
3.5	References	39
Chapter 4:	Parameterization of Bootstrap Analysis for Prediction of the Primary Eigenvector's Distribution	41
4.1	Motivation	41
4.2	Introduction	42

4.3	Methods	43
4.3.1	Bootstrap Acquisition	43
4.3.2	Histogram Analysis	43
4.4	Results	46
4.4.1	Bootstrap Histograms	46
4.4.2	Elliptical Fit of Histograms	47
4.5	Discussion	49
4.6	References	50
 Chapter 5: Quantitative DTI Fiber Tracking of the Corticospinal Tract in Patients with Congenital Hemiplegia		51
5.1	Motivation	51
5.2	Methods	52
5.2.1	DTI acquisition	52
5.2.2	Patient and Control Population	52
5.3	Fiber Tracking	53
5.3.1	Selection of fiber tracking ROIs	54
5.3.2	Quantitation of DTI Parameters	54
5.4	Results	55
5.4.1	Qualitative Analysis	55
5.4.2	Asymmetry in Patients	57
5.4.3	Anisotropy Changes with Age	58
5.5	Discussion	59
5.6	References	60
 Chapter 6: DTI Fiber Tracking from Motor Points Defined by Intraoperative Cortical Stimulation		62
6.1	Abstract	62
6.2	Introduction	63
6.3	Methods	64
6.3.1	MR Imaging	64
6.3.2	Cortical Stimulation and Stereotactic Registration	65
6.3.3	Fiber Tracking	66
6.4	Results	68
6.4.1	Motor Pathway Delineated with Diffusion Tensor Fiber Tracking	68
6.4.2	Fiber Tracking and Crossing Neuronal Fibers	72
6.4.3	Fiber Tracking and Edema	73
6.5	Discussion	74
6.5.1	Delineation of a Functionally Specific White Matter Pathway	74

UCSF LIBRARY

6.5.2	Limitations of the DTI Fiber Tracking Technique	76
6.5.3	Use of DTI Fiber Tracking for Surgical Planning	78
6.6	Conclusions	79
6.7	References	80
Chapter 7: Accuracy of Diffusion Tensor MRI Tractography Assessed with Subcortical Intraoperative Stimulation		82
7.1	Abstract	82
7.2	Introduction	83
7.3	Methods	85
7.3.1	Imaging	85
7.3.2	DTI Fiber Tracking	86
7.3.3	Subcortical Stimulation	88
7.4	Results	89
7.4.1	DTI Fiber Tracking	89
7.4.2	MSI Correlation with DTI Fiber Tracks	91
7.5	Discussion	93
7.6	Conclusion	99
7.7	References	99
Chapter 8: Presurgical DTI Fiber Tracking Protocol		102
8.1	Motivation	102
8.2	Introduction	102
8.3	Constraints	103
8.3.1	Timing	103
8.3.2	Interference of Overlaid Fiber Tracks with Underlying Anatomy	104
8.3.3	Registration of MR Volumes	104
8.3.4	Image Accuracy and Quality Assurance	105
8.4	Technique Methods	105
8.4.1	Medical Center Image Network	106
8.4.2	DTI Processing and Fiber Tracking	107
8.4.3	Fusion of Anatomical Images and DTI Fiber Tracks	110
8.4.4	Transmission of Images to PACS	112
8.5	Use of DTI in the OR	115
8.6	References	115

UCSF LIBRARY

Chapter 9: Quantitative DTI Fiber Tracking of the Preterm Infant's Sensorimotor Tracts	117
9.1 Abstract	117
9.2 Introduction	118
9.3 Methods	120
9.3.1 Patient Population	120
9.3.2 Imaging	121
9.3.3 DTI Fiber Tracking	123
9.4 Results	126
9.4.1 Tract-Specific Measurements	129
9.4.2 Region-Specific Measures	132
9.5 Discussion	134
9.5.1 ROIs Based on DTI Fiber Tracking	134
9.5.2 Measurements of Developing Sensorimotor Tracts	136
9.5.3 Comparison of Fiber Tracking Methods	137
9.5.4 Region Specific Characteristics	139
9.6 Conclusion	141
9.7 References	141
Chapter 10: Main Findings and Conclusions	145

UCSF LIBRARY

List of Figures

Figure 2-1: The neuron.	6
Figure 2-2: Brodmann's cytoarchitectural map of the human brain.	8
Figure 2-3: The Ojemann stimulator with bipolar electrode.	14
Figure 3-1: Precession of a magnetic moment.	20
Figure 3-2: A 90 degree flip of the magnetic moment to the x-y plane.	21
Figure 3-3: Echo planar pulse sequence.	23
Figure 3-4: The k-space trajectory of an echo planar pulse sequence.	24
Figure 3-5: Types of diffusion.	29
Figure 3-6: Pulsed-gradient spin echo diffusion sequence.	30
Figure 3-7: Diffusion tensor parameters.	35
Figure 3-8: FACT algorithm in action.	37
Figure 3-9: Illustrative example of deterministic FACT algorithm.	38
Figure 4-1: Schematic of DTI bootstrap analysis.	42
Figure 4-2: Histogram of primary eigenvectors' directions.	44
Figure 4-3: Example distributions of the primary eigenvector in three voxels.	47
Figure 4-4: 2D elliptical Gaussian fit maps.	48
Figure 5-1: Fiber tracks of the motor pathway in a hemiparetic patient.	56
Figure 5-2: 3D fiber tracks of a hemiparetic patient.	56
Figure 5-3: DTI parameters in hemiparetic and control subjects.	57
Figure 5-4: Asymmetry related to degree of hemiparesis.	58
Figure 5-5: Relative anisotropy as a function of age.	59
Figure 6-1: Exposed human brain cortex.	64
Figure 6-2: Fiber tracking from stereotactically identified motor site.	66
Figure 6-3: Subcortical organization of DTI fiber tracks.	71
Figure 6-4: Fiber tracks encountering crossing fibers.	72
Figure 6-5: Fiber track divergence in edema.	74
Figure 7-1: DTI fiber tracks overlaid on EPI, FSE and SPGR volumes.	87
Figure 7-2: Arm motor subcortical stimulation site and DTI fiber tracks.	90
Figure 7-3: Distances between stimulation sites and DTI fiber tracks.	91
Figure 7-4: Juxtaposition of subcortical motor sites, fiber tracks, and MSI.	92
Figure 7-5: Compression of the motor and sensory tracts.	93
Figure 7-6: A subcortical thumb motor site localized to temporal lobe.	97
Figure 8-1: Flowchart of medical center systems.	106
Figure 8-2: Timing of presurgical DTI protocol.	107
Figure 8-3: Starting and target ROIs for fiber tracking.	109
Figure 8-4: Presurgical DTI fiber tracks of the corticospinal tract.	110
Figure 8-5: DTI fiber tracks of the motor tract overlaid on anatomical images.	111
Figure 8-6: Stereotactic navigation system.	113
Figure 8-7: Screen capture from the surgical navigation system.	114
Figure 9-1: Starting and target regions for DTI fiber tracks in an infant.	125
Figure 9-2: Axial cross sections of deterministic DTI fiber tracks in an infant.	127
Figure 9-3: Axial cross sections of probabilistic DTI fiber tracks in an infant.	128

UCSF LIBRARY

Figure 9-4: 3D rendering of DTI fiber tracks and infant head.	129
Figure 9-5: 3D tract-specific measurements from deterministic fiber tracking.	130
Figure 9-6: 3D tract-specific measurements from probabilistic fiber tracking.	131
Figure 9-7: Diffusion parameters measured along motor and sensory tracts.	133
Figure 9-8: White matter complexity increases during development.	140

1107 110711071

List of Equations

Equation 3-1: Proton energy.	18
Equation 3-2: Energy gap in presence of magnetic field.	19
Equation 3-3: Number of spins parallel and anti-parallel to magnetic field.	19
Equation 3-4: Equilibrium magnetic dipole.	19
Equation 3-5: Larmor frequency.	19
Equation 3-6: Precession of the magnetic moment.	19
Equation 3-7: Flux of magnetic field through a surface.	20
Equation 3-8: Faraday's law of induction.	20
Equation 3-9: Excitation radio frequency pulse.	20
Equation 3-10: Bloch equation.	21
Equation 3-11: MR signal equation.	23
Equation 3-12: Fick's first law of diffusion.	26
Equation 3-13: Fick's second law of diffusion.	26
Equation 3-14: Diffusion coefficient.	27
Equation 3-15: Diffusion displacement probability.	27
Equation 3-16: Mean displacement.	28
Equation 3-17: Anisotropic diffusion flow.	28
Equation 3-18: Echo planar dephasing.	31
Equation 3-19: Anisotropic diffusion displacement probability.	32
Equation 3-20: Signal equation including diffusion tensor.	32
Equation 3-21: Bloch-Torrey equation.	32
Equation 3-22: Signal equation from solved Bloch-Torrey equation.	32
Equation 3-23: Expression for k-space position	32
Equation 3-24: Signal attenuation in a diffusion MR experiment.	33
Equation 3-25: Expression for b value.	33
Equation 3-26: Eigenvectors of the diffusion tensor.	33
Equation 3-27: Eigenvectors and eigenvalues.	34
Equation 3-28: Directionally averaged diffusion coefficient.	34
Equation 3-29: Fractional anisotropy.	35
Equation 3-30: Relative anisotropy.	35
Equation 4-1: Rotation matrix #1.	44
Equation 4-2: Rotation matrix #2.	44
Equation 4-3: Combined rotation matrix.	45
Equation 4-4: Rotation of eigenvector into histogram coordinate system.	45
Equation 4-5: Histogram bin assignment.	45
Equation 4-6: 2D elliptical Gaussian.	46

UCSF LIBRARY

List of Tables

Table 4-1: Regression of DTI parameters to 2D elliptical Gaussian fit.	49
Table 5-1: Hemiplegic patient population.	53
Table 6-1: Summary of brain tumor cases and fiber tracking results.	70
Table 7-1: Brain tumor patients with subcortical motor stimulations.	86
Table 9-1: Signal to noise ratios of echo planar images.	122

UCSF LIBRARY

Chapter 1: Introduction

Many techniques exist to investigate the anatomy and physiology of the brain. These techniques range in scope from single neuron electrical recordings to a psychological examination by a psychiatrist. Some techniques are invasive such as cortical stimulation, while other methods including magnetic resonance imaging (MRI) are non-invasive. Magnetoencephalography is appropriate for humans while chemical tracer studies are only performed in animals. Each technique provides different insights into an aspect of brain function, however each method has inherent limitations. Information from these research techniques complement each other and can be used to advance our understanding of the brain.

This thesis project used magnetic resonance imaging (MRI) to study the white matter pathways of the human brain. MRI is safe, non-invasive, and can be performed on patient and control populations. Diffusion tensor imaging (DTI) is an MRI technique that is sensitive to the Brownian motion of water. DTI can probe the 3D diffusion pattern of water within the human brain. The assumption is made that the measured diffusion pattern can be used to determine the brain's microstructure. DTI fiber tracking is a technique which uses anisotropic diffusion patterns to delineate specific white matter pathways. This bioengineering thesis project involved acquiring DTI data, implementing a DTI fiber tracking algorithm,

performing feasibility and validity studies, performing patient studies, and transitioning DTI fiber tracking into a routinely used surgical planning tool.

Chapter 2 and chapter 3 present the basics of brain anatomy, physiology, and MR physics necessary for interpreting the research performed in this thesis project. The brain's white matter pathways are extremely complex but at the same time, highly organized. DTI fiber tracking takes advantage of coherently arranged axons to determine brain structure and connectivity.

For chapter 4, I implemented a bootstrap based model of the uncertainty in the primary eigenvector's orientation. DTI fiber tracking assumes that the primary eigenvector reflects the orientation of axonal bundles. Understanding the primary eigenvector's measurement error is important for assessing the accuracy of DTI fiber tracking.

In chapter 5 of this thesis project, tools were developed for generating DTI fiber tracks and making tract-specific measurements. These analysis tools were used in a study of patients with congenital hemiplegia. It was determined that DTI fiber tracking could be used to quantitatively detect structural differences in motor tracts affected by hemiplegia. However, the measurements of this study were restricted to a region of the motor tract least susceptible to fiber tracking errors. The next chapters in this thesis project address the validity of using DTI fiber tracking to delineate the entire cerebral motor tract.

In chapter 6, I used intraoperative cortical stimulation sites to launch DTI fiber tracks of the descending motor pathway. This study showed that DTI fiber tracking could follow the motor tract between functional cortex and the cerebral peduncle in brain tumor patients. However, I identified limitations in the DTI fiber tracking technique caused by crossing axonal fiber populations in the centrum semiovale.

Chapter 7 builds upon the results in chapter 6 by determining the accuracy of DTI fiber tracks within deep white matter structures. I generated DTI fiber tracks of the motor tract in patients prior to tumor resection. The DTI fiber tracking data was visualized on a stereotactic navigation system during the brain surgery. After the surgery, I compared the location of subcortical motor stimulation sites to the DTI fiber tracks. The results showed that DTI fiber tracks were within the application error of stereotactic localization and were thus useful in surgical planning.

Chapter 8 describes the presurgical DTI fiber tracking protocol that I developed in response to the technique being requested by the neurosurgeons for a great number of brain tumor cases. The protocol involves DTI acquisition, generation of DTI fiber tracks, fusion of the data with anatomical images, and delivery of the final images to the surgical staff. The protocol was designed to ensure patient safety and be robust enough for routine use. I have successfully used the

protocol to provide DTI fiber tracks for approximately one hundred surgical cases.

Chapter 10 applied the tools and results from the prior chapters to a clinical study of white matter development. DTI was performed on premature infants undergoing early phases of white matter maturation. I used DTI fiber tracking to make tract-specific measurements of the motor and sensory tracts. Age related changes in DTI parameters were observed. DTI fiber tracking allowed me to analyze the heterogeneity of DTI parameters within different regions of the sensorimotor white matter pathways.

UCSF LIBRARY

Chapter 2: Human Brain Basics

2.1 Overview

This chapter presents the biological foundation for the research conducted in this project. The basics of neuroanatomy and brain organization are presented. In addition, this chapter includes a brief description of the patient populations and functional mapping techniques used in this thesis project.

2.2 Brain Organization

The workings of the human brain are not well understood. Diffusion magnetic resonance imaging (DTI) provides information on the microstructure of brain tissue by examining the diffusion patterns of water. However, the challenge is to translate these diffusion patterns into biologically relevant information such as white matter structure, integrity, or connectivity. This section provides some fundamental information on brain anatomy and physiology necessary for interpreting the results of diffusion MR experiments. The following sections include a description of neurons and how neurons are organized into white matter pathways. Much of this thesis project focused on the corticospinal tract, so the anatomy of the motor system is described.

UCSF LIBRARY

2.2.1 The Neuron

The neuron is the cellular unit comprising the functional building block of the brain (Figure 2-1). The soma, dendrites and synapses of the neuron are found in the grey matter of the brain. The axons comprise the brain's white matter structures. The input to a typical neuron is another neuron synapsing on the dendrites. The neuron transmits information with electrical pulses called action potentials. Incoming postsynaptic currents cause the axon hillock to depolarize. Once the threshold membrane voltage is reached, an action potential is triggered which travels in one direction down the axon. The axon is wrapped in myelin, enabling saltatory conduction of the action potential over long distances. Saltatory conduction occurs in fast leaps between gaps in the myelin sheath called nodes of Ranvier. The action potential reaches the synaptic terminals, which chemically signal the dendrites of the next neuron (7).

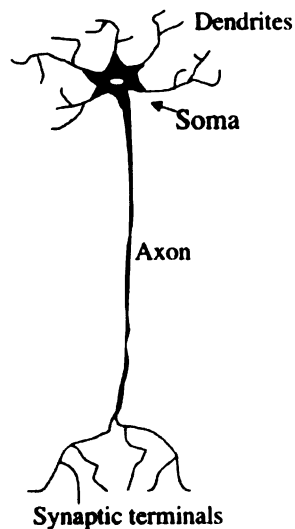


Figure 2-1: The neuron. Information is carried from the dendrites to the synaptic terminals.

UCSF LIBRARY

2.2.2 White Matter Pathways

There are more than 100 billion neurons in the central nervous system (7). White matter pathways are bundles of axons connecting different regions of the central nervous system. There are three general types of white matter pathways in the brain. Association pathways, such as the arcuate fasciculus, connect two grey matter regions within the same hemisphere. Commissural pathways, such as the corpus callosum, connect the left and right sides of the brain. Projectional pathways, such as the corticospinal tract, connect the cerebrum to the spinal cord or brainstem.

2.2.3 Functional Organization of the Brain

White matter pathways comprise the brain's point to point wiring. However, data processing occurs in the brain's grey matter. A single neuron may receive input from thousands of neurons and in turn synapse onto thousands of other neurons. Neuronal circuitry can be extremely complex, however, neurons with similar functions tend to be grouped together in both the cortex and white matter.

Diffusion tensor imaging relies upon a certain degree of organization within white matter pathways. The voxels comprising an MR image are of finite size. If the billions of axons in the brain were randomly arranged, water diffusion would not be anisotropic when integrated over the volume of a voxel. However, since white matter pathways are typically comprised of coherently oriented axons, diffusion

UCSF LIBRARY

tensor imaging can be used to determine the orientation and microstructural properties of axonal bundles.

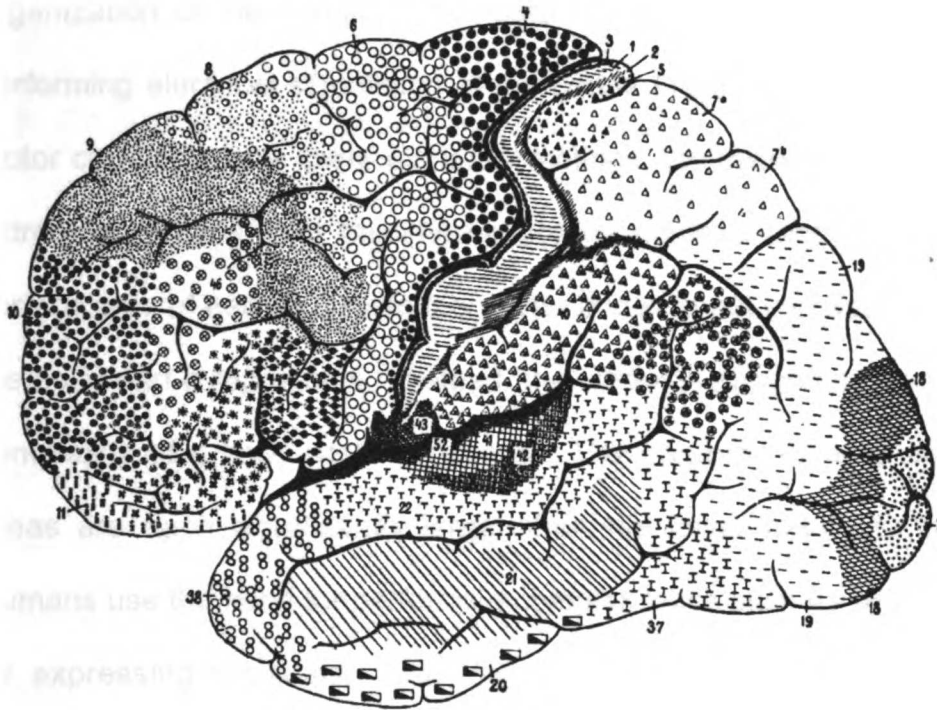


Figure 2-2: Brodmann's cytoarchitectural map of the human brain.

In 1909, Brodmann published a map of the human cortex showing histologically distinct regions (Figure 2-2) (3). These regions are often separated by sulci. For example, Brodmann area 4 is within the precentral gyrus and comprises the primary motor cortex. The motor cortex is the origin of the motor tract, which controls voluntary movements. Axons from the pyramidal cells within the motor cortex descend through the corona radiata, posterior limb of the internal capsule, and cerebral peduncle before innervating motor nerves. These anatomical landmarks can be seen on MR images and were used in this thesis to judge the accuracy of diffusion MR fiber tracking.

The primary motor cortex is further organized somatotopically. The topological organization of the human motor cortex has been shown by neurosurgeons performing electrical stimulation of the cortex (14). The superior region of the motor cortex controls lower extremity motions, the middle region controls upper extremity motions, and the inferior portion controls face motor. The relative surface area of each subsection of motor cortex is not correlated with the size of the body part it represents. Instead, the cortex is apportioned according to the complexity of a body part's functions. The hand motor area and face motor areas are each significantly larger than the lower extremity cortical areas. Humans use the hand for performing complex tasks such as writing and the face for expressing emotions. The lower extremities perform simpler, repetitive functions such as walking.

The logical organization of the brain's cortex is coupled with the orderly arrangement of white matter pathways. White matter tracts follow paths that minimize distance and avoid sharp angles. Large white matter fasciculi often share a common function. The white matter bundles themselves may be functionally organized. For example, the corpus callosum and superior longitudinal fasciculus are large white matter bundles that can be further subdivided into regions having common destinations and functions. The motor tract maintains its somatotopic organization as it descends through the internal capsule and into the cerebral peduncle (10). In this thesis project, DTI fiber

tracks of the motor tract were shown to exhibit the expected anatomical placement and somatotopic organization.

2.3 Populations Included in this Project

2.3.1 Congenital Hemiplegia

Congenital hemiplegia refers to a range of motor deficits caused by perinatal brain injury damaging the motor tract. Symptoms may include decrease in strength, spasticity, or poor coordination. Patients with congenital hemiplegia only have motor deficits on one side of the body. Thus, it is expected that damage to the motor tract is restricted to the side of the brain controlling the affected muscle groups (2, 6). This project includes a study which investigated the ability of DTI fiber tracking to measure differences between the left and right motor tracts in hemiplegic patients. This patient population is ideal for developing quantitative DTI fiber tracking techniques because the unaffected side of the brain serves as an internal control, eliminating the effect of inter-subject variability.

2.3.2 Brain Tumor

Brain tumors are rapidly reproducing cellular masses that apply pressure to surrounding tissue and thereby can disrupt or displace adjacent white matter tracts (1, 15). Common symptoms include seizure, headache, and motor deficit. Treatment options include surgery, radiation therapy, chemotherapy, and

immunotherapy. During surgical resection, the surgeon will usually try to avoid cutting through and damaging functional motor cortex. Brain tumor patients are a unique population because they undergo diffusion MR in addition to a battery of invasive and non-invasive functional mapping techniques. This thesis project used intraoperative functional mapping data to validate DTI fiber tracking. Invasive motor stimulation can not be performed on control subjects, but is routinely performed on brain tumor patients. This thesis project helped establish DTI fiber tracking of the motor tract as a feasible and clinically useful tool to identify the position of eloquent fibers near a tumor.

2.3.3 Premature Infants

The preterm human infant brain undergoes rapid structural and functional development. Before birth, 100 billion neurons are produced through mitotic division (5). These neurons mature during gestation, after birth, and continue to change in structure and function through adolescence. During preterm development, chemical signals guide the sequential migration of the brain's neurons and neuroglia into the brain's axonal connections necessary for normal function (8). As the complexity of neuronal architecture increases, the hemispheres, lobes, and sulci form. The preterm brain is largely unmyelinated. Myelination occurs first in the spinal cord and hindbrain. In term-equivalent aged infants, some cerebral pathways such as the pyramidal tract have begun to myelinate. The prefrontal lobe is the last to fully myelinate and matures through adolescence.

UCSF LIBRARY

During the critical first weeks of development prior to term age, the neonate is susceptible to white matter injury and multiple life-long disorders with a neurodevelopmental origin. Understanding the course of brain development is important for early intervention to improve prognosis. Diffusion MR is a non-invasive method of monitoring the changing structure of the preterm infant brain. In this thesis project, I have applied DTI fiber tracking to the study of infant brain development.

2.4 Functional Mapping Techniques

This thesis project involved correlating DTI fiber tracking with functional mapping techniques. DTI fiber tracking provides information on the structure of brain tissue but does not inherently provide any functional information. Functional mapping refers to any technique that localizes regions of the brain based on physiological changes that are invoked or measured. Functional mapping is generally restricted to grey matter. Active functional mapping involves invoking a response by stimulating part of the brain and passive functional mapping techniques measure physiological changes which occur during normal brain usage. Transcranial magnetic stimulation and intraoperative stimulation are active and invasive techniques which use electric or magnetic fields to depolarize neurons. Magnetic source imaging (MSI) and functional MR (fMRI) are non-invasive mapping techniques which measure magnetic field or blood flow

changes during specific tasks. The following is a brief overview of the functional mapping methods used in this thesis project.

2.4.1 Intraoperative Stimulation Mapping

Intraoperative stimulation mapping is an invasive technique used by neurosurgeons during brain surgery to precisely identify regions of the brain controlling various functions. Stimulation mapping can be used to identify motor, sensory, or language sites (13, 14). Bipolar and monopolar stimulation are both possible, however bipolar stimulation is typically used because the current is restricted to a smaller region (9, 11, 19). The Ojemann bipolar stimulator used by neurosurgeons for this project has two steel conducting electrodes located 5mm apart (Figure 2-3) (Integra Lifesciences Corporation, Plainsboro, NJ). During stimulation, a 60Hz square wave is passed between the electrodes with current up to 20mA. The level of current can be controlled and the lowest current which produces a response is used. Typical current amplitudes are in the range of 4-10mA. Higher currents are typically required in anesthetized patients. Bipolar stimulation can be performed either cortically or subcortically. Subcortical stimulation is the only method of functionally mapping the white matter in humans.

UCSF LIBRARY



Figure 2-3: The Ojemann stimulator with bipolar electrode.

Bipolar stimulation of the brain can either excite or inhibit activity in neurons (16). In awake patients performing language tasks, stimulation has been described as behaving like a temporary lesion and inhibits language function (12). When the primary motor cortex is stimulated, specific muscle groups are activated on the contralateral side of the body. This thesis project used intraoperative motor stimulation to validate DTI fiber tracking.

2.4.2 Magnetic Source Imaging

Magnetic source imaging (MSI) localizes regions of functional cortex by detecting the magnetic field associated with the electrical currents traveling through neurons (4, 20). Post-synaptic potentials traveling along dendrites are believed to be primary source of the magnetic field. Hundreds of thousands of parallel dendrites are necessary to generate a magnetic field large enough to be detected. The electrical currents within the neurons generate a magnetic flux

according to the right hand rule. Magnetic fields, unlike electric fields, are not greatly distorted or attenuated by the brain, skull, or air. However, MSI is most sensitive to currents parallel to the skull. This restriction causes most MSI sites to be located in cortices beneath the surface of the brain. To aid in detecting the small magnetic flux associated with functioning cortex, a superconducting quantum interference device (SQUID) is required for measurements. The SQUID is a superconducting receiving coil that is cooled in liquid helium. Typical MSI instruments use dozens of SQUIDs placed adjacent to the subject's skull. The entire MSI instrument and subject must be inside a faraday cage to shield the experiment from electromagnetic noise. The patient performs either a sensory or motor task during the examination. A typical MSI examination is between 2 and 3 hours long. The signal from each of the sensors is combined and a source localization algorithm is used to determine the coordinates of the active cortex.

MSI is routinely performed presurgically for patients with brain tumors near eloquent cortices. Localization of sensorimotor cortices is important for surgical planning and can help reduce post-operative morbidity (17, 18). In this thesis project, MSI localization was compared with results from DTI fiber tracking. MSI dipoles are restricted to the cortex, however, their proximity to the endpoints of fiber tracks can confirm the accuracy of DTI fiber tracking.

2.5 References

1. Berger MS, Wilson CB: *The Gliomas*. Elsevier Science, 1999.
2. Bouza H, Dubowitz LM, Rutherford M, Pennock JM: Prediction of outcome in children with congenital hemiplegia: a magnetic resonance imaging study. **Neuropediatrics** 25:60-66, 1994.
3. Brodmann K: *Vergleichende localisationslehre der grosshirnrinde in ihren principien dargestellt auf grund des zellenbaues*. Leipzig, Barth, 1909.
4. Cohen D: Magnetoencephalography: detection of the brain's electrical activity with a superconducting magnetometer. **Science** 175:664-666, 1972.
5. Diamond MC, Scheibel AB, Elson LM: *The Human Brain Coloring Book*. New York, Harper Collins, 1985.
6. Duque J, Thonnard JL, Vandermeeren Y, Sebire G, Cosnard G, Olivier E: Correlation between impaired dexterity and corticospinal tract dysgenesis in congenital hemiplegia. **Brain** 126:732-747, 2003.
7. Guyton AC, Hall JE: *Textbook of Medical Physiology*. Philadelphia, W.B. Saunders, 1996.
8. Kandel ER, Schwartz JH, Jessel TM: *Principles of Neural Science*. McGraw-Hill Medical, 2000.
9. Kombos T, Suess O, Kern BC, Funk T, Hoell T, Kopetsch O, Brock M: Comparison between monopolar and bipolar electrical stimulation of the motor cortex. **Acta Neurochir (Wien)** 141:1295-1301, 1999.
10. Martin JH: *Neuroanatomy : text and atlas*. Stamford, Conn., Appleton & Lange, 1996.
11. Nathan SS, Sinha SR, Gordon B, Lesser RP, Thakor NV: Determination of current density distributions generated by electrical stimulation of the human cerebral cortex. **Electroencephalogr Clin Neurophysiol** 86:183-192, 1993.
12. Ojemann G: Brain organization for language from the perspective of electrical stimulation mapping. **The Behavioral and Brain Sciences** 6:189-230, 1983.
13. Ojemann G, Ojemann J, Lettich E, Berger M: Cortical language localization in left, dominant hemisphere. An electrical stimulation mapping investigation in 117 patients. **J Neurosurg** 71:316-326, 1989.
14. Penfield W, Rasmussen T: *The cerebral cortex of man : a clinical study of localization of function*. New York, Macmillan, 1950.
15. Prados M: *Brain Cancer*. London, BC Decker Inc, 2002.
16. Ranck JB, Jr.: Which elements are excited in electrical stimulation of mammalian central nervous system: a review. **Brain Res** 98:417-440, 1975.
17. Schiffbauer H, Berger MS, Ferrari P, Freudenstein D, Rowley HA, Roberts TP: Preoperative magnetic source imaging for brain tumor surgery: a quantitative comparison with intraoperative sensory and motor mapping. **J Neurosurg** 97:1333-1342, 2002.

UCSF LIBRARY

18. Schiffbauer H, Ferrari P, Rowley HA, Berger MS, Roberts TP: Functional activity within brain tumors: a magnetic source imaging study. **Neurosurgery** 49:1313-1320; discussion 1320-1311, 2001.
19. Stark P, Fazio G, Boyd ES: Monopolar and bipolar stimulation of the brain. **Am J Physiol** 203:371-373, 1962.
20. Wheless JW, Castillo E, Maggio V, Kim HL, Breier JI, Simos PG, Papanicolaou AC: Magnetoencephalography (MEG) and magnetic source imaging (MSI). **Neurologist** 10:138-153, 2004.

UCSF LIBRARY

Chapter 3: Diffusion Tensor Imaging

3.1 Magnetic Resonance Imaging

Magnetic resonance imaging (MRI) is a safe, non-invasive medical imaging modality that provides a wealth of diagnostic and scientific information on the anatomy and physiology of the human body. The basic components necessary for an MR experiment are a strong magnetic field, a radiofrequency transmit-receive coil, magnetic field gradients, and a human filled with water. In this thesis project, MRI acquisitions sensitive to the diffusion of water were used to study white matter pathways. This chapter describes the basic principles of MRI, molecular diffusion, and diffusion MR.

3.1.1 The Proton

The origin of the signal in MRI is the hydrogen proton (8, 15, 22). Nuclear spin is a property of protons that creates a small magnetic moment associated with each proton. When a proton is placed in a large magnetic field, \mathbf{B}_0 , the spins' magnetic moments will be oriented either parallel or anti-parallel to \mathbf{B}_0 . Protons with spins parallel to \mathbf{B}_0 are in a lower energy state, E , than spins anti-parallel to \mathbf{B}_0 .

$$E = \hbar \gamma m_s B_0 \quad \text{Equation 3-1}$$

The m_s variable indicates if the spin is aligned with \mathbf{B}_0 and can have values of $\pm 1/2$. The γ constant is the gyromagnetic constant, which is 42.58 Mhz/Tesla for

protons. The energy difference, ΔE , between the two proton spin states is dependant on B_0 .

$$\Delta E = \hbar\gamma B_0 \quad \text{Equation 3-2}$$

The number of spins parallel to the magnetic field, N_\uparrow , exceeds the number anti-parallel, N_\downarrow , according to the Boltzmann probability distribution.

$$\frac{N_\downarrow}{N_\uparrow} = e^{\frac{-\Delta E}{kT}} \quad \text{Equation 3-3}$$

The excess number of spins parallel to the magnetic field is very small, however, if B_0 and the proton density are high enough, an equilibrium magnetic dipole, M_0 , is large enough to be detected.

$$M_0 = \frac{\rho_0 \hbar^2 \gamma^2 B_0}{4kT} \quad \text{Equation 3-4}$$

3.1.2 Precession and the MR Signal

In the presence of a magnetic field, the magnetic moment precesses at the Larmor frequency, ω_0 .

$$\omega_0 = \gamma B_0 \quad \text{Equation 3-5}$$

The movement of the magnetic moment, \mathbf{M} , is described by the cross product of \mathbf{M} and \mathbf{B}_0 .

$$\frac{d\mathbf{M}}{dt} = \gamma \mathbf{M} \times \mathbf{B}_0 \quad \text{Equation 3-6}$$

UCSF LIBRARY

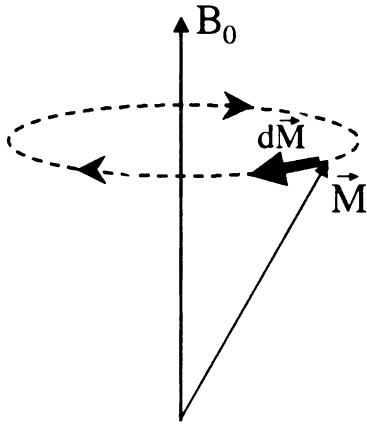


Figure 3-1: Precession of a magnetic moment about an external magnetic field.

Precession can be employed to create a measurable signal related to the magnitude of \mathbf{M} . Faraday's law of induction relates a changing magnetic flux, Φ , passing through a receiving coil's area, S , to an electromotive force, V .

$$\Phi = \int_S \mathbf{M} \cdot d\mathbf{s} \quad \text{Equation 3-7}$$

$$V = -\frac{d\Phi}{dt} \quad \text{Equation 3-8}$$

However, the equilibrium magnetic moment, \mathbf{M}_0 , is parallel to the external field and static. In an MR experiment, \mathbf{M}_0 is first rotated to the transverse plane with an excitation radio frequency pulse, \mathbf{B}_1 .

$$\mathbf{B}_1(t) = B_1(t)(\cos(\omega_0 t)\hat{x} - \sin(\omega_0 t)\hat{y}) \quad \text{Equation 3-9}$$

According to Equation 3-9, \mathbf{B}_1 is made to rotate in the x-y plane at the Larmor frequency. By using a coordinate system, (x', y', z) , rotating at the Larmor frequency, \mathbf{B}_1 remains along the \hat{x}' direction and \mathbf{M}_0 rotates about x' . After \mathbf{B}_1 is turned off, the transverse magnetization, \mathbf{M}_{xy} , precesses at the Larmor

frequency within the x-y plane. This rotating magnetic moment can be detected with an RF receive coil oriented perpendicular to the x-y plane.

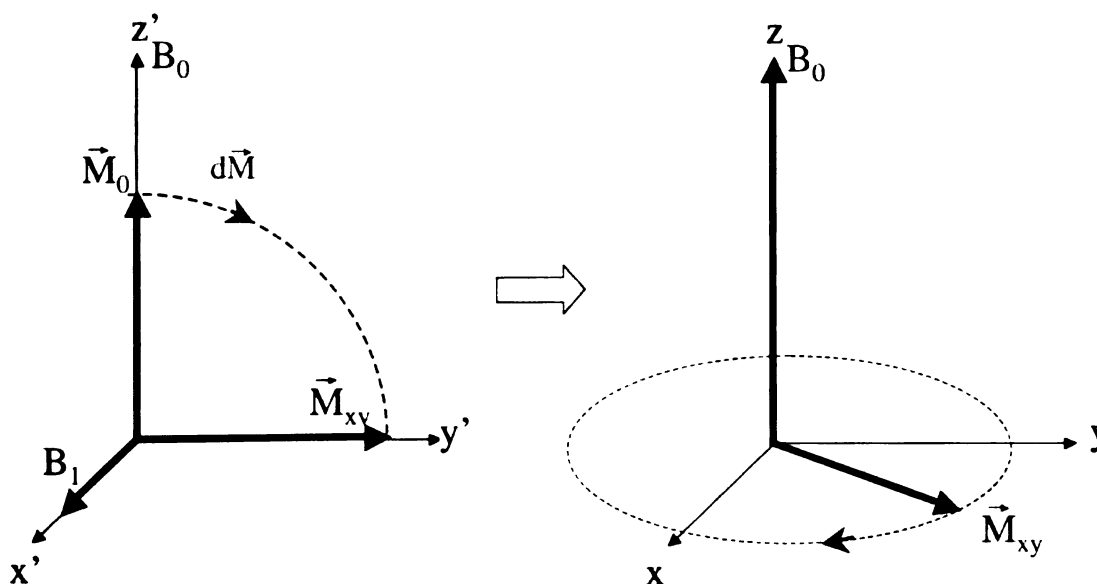


Figure 3-2: A 90 degree flip excitation of the magnetic moment to the x-y plane. Once the magnetic moment is within the x-y plane, M_{xy} precesses about the external magnetic field.

The Bloch equation is a general description of the interaction of a magnetic dipole, \mathbf{M} , with an external magnetic field (Equation 3-10). In addition to the precession term, the Bloch equation also includes terms that describe how the longitudinal magnetization (M_z) and the transverse magnetization (M_{xy}) return to equilibrium. The spin-lattice relaxation time constant, T_1 , describes the growth of M_z back to equilibrium. The spin-spin relaxation time constant, T_2 , describes the decay of the transverse magnetization.

$$\frac{\partial \mathbf{M}(t)}{\partial t} = \gamma \mathbf{M}(t) \times \mathbf{B} + \frac{1}{T_1} (\mathbf{M}_0 - M_z(t)) \hat{z} - \frac{1}{T_2} \mathbf{M}_{xy}(t) \quad \text{Equation 3-10}$$

3.1.3 Relaxation

After excitation, the protons are placed in higher energy states. Relaxation refers to how the proton population returns to equilibrium. The rate of relaxation is controlled by local molecular structure and interactions. In MRI, contrast is achieved because different tissues have different relaxation times and thus different MR signals (11).

T_1 relaxation occurs when protons lose energy to the environment, termed the lattice. In order for energy to be effectively exchanged, a nearby molecule must be rotating at a rate close to the Larmor frequency. The growth of the longitudinal magnetization is described by T_1 .

T_2 relaxation is also caused by molecular interactions. The T_2 relaxation time is always less than or equal to T_1 . Moving protons cause a local change in the magnetic field. These inhomogeneities in the local magnetic field cause each proton to precess at slightly different frequencies and dephase. As the individual magnetic dipoles become out of phase, the net transverse magnetization decreases in magnitude at a rate described by T_2 . Inhomogeneities in the main magnetic field also cause dephasing of the transverse magnetization. This additional dephasing, combined with T_2 relaxation constitutes T_2^* relaxation (15).

LIBRARY
UNIVERSITY OF
SOUTH ALABAMA

3.1.4 Echo Planar Imaging

The imaging equation for MR relates the received signal, $s(\mathbf{k})$, to the net transverse magnetization, $\rho(\mathbf{r})$, by a Fourier transform (Equation 3-11). G_i is the magnitude of the magnetic gradient in the i direction.

$$s(k_x, k_y, k_z) = \iiint \rho(x, y, z) e^{-i2\pi(k_x x + k_y y + k_z z)} dx dy dz$$

$$k_i(t) = \gamma \int_0^t G_i(\tau) d\tau \quad \text{Equation 3-11}$$

There are many techniques for sampling $s(\mathbf{k})$ sufficiently to construct an image. The diffusion MR images acquired in this project rely on echo planar imaging (EPI). EPI is a rapid imaging method which acquires an entire 2D image after one excitation and within one repetition time (18). The pulse sequence and k-space coverage for spin-echo echo planar imaging are shown in Figure 3-3 and Figure 3-4.

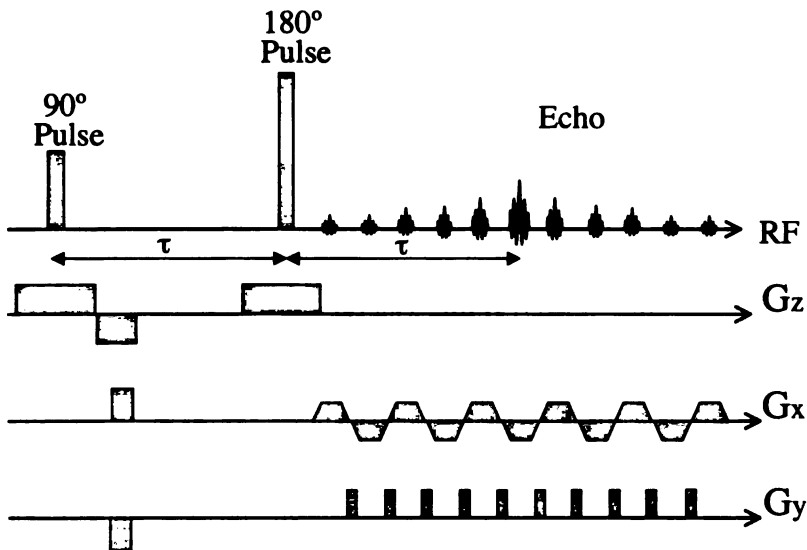


Figure 3-3: Echo planar pulse sequence.

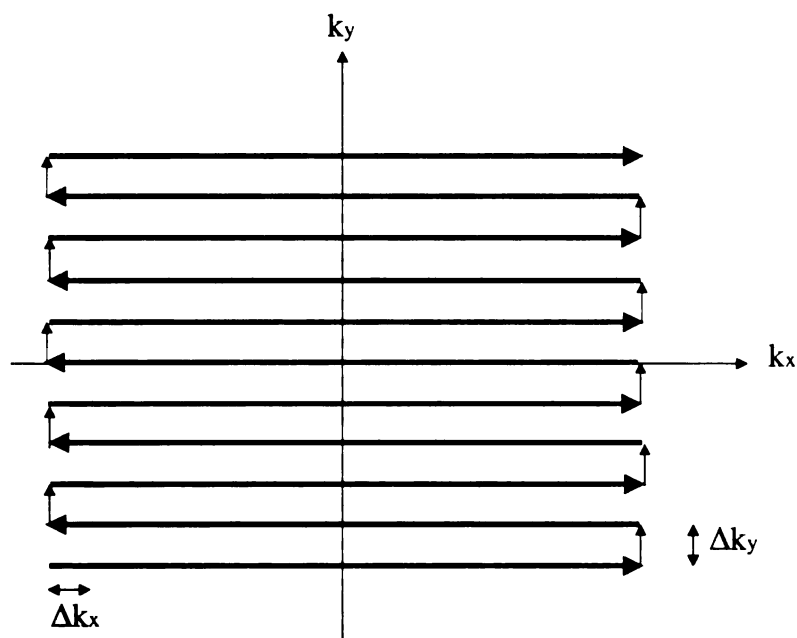


Figure 3-4: The k-space trajectory of an echo planar pulse sequence.

Each k_x line of k-space is acquired while the G_x frequency encoding readout gradient is applied. Between readout gradients, a G_y phase encoding “blip” is applied to advance to the next line of k-space. The spin-echo signal is greatest at $TE=2\tau$. Since the center of k-space is most important for overall image contrast, the pulse sequence is designed such that the center of k-space is filled at $t=2\tau$.

A fast acquisition method like echo-planar imaging is necessary to reduce motion during diffusion MR acquisition. An entire echo planar image can be acquired in approximately 100ms, which is fast enough to be insensitive to most sources of patient motion. However, the readout gradient reversals and long read out times contribute to ghosting and off-resonance artifacts (23).

Eddy currents and the back and forth k-space trajectory cause a variation in phase from line to line in k-space. This phase modulation manifests as N/2 ghosting in the reconstructed image. A ghost image is superimposed on the image matrix, but shifted half a field of view.

The sampling rate in the frequency encoding direction is fast, however the sampling rate and bandwidth are low in the phase encoding direction. The low bandwidth in the phase encoding direction can cause significant chemical shift artifacts. Fat and water at the same position may be separated by several voxels on the reconstructed image. At higher magnetic field strengths, the difference in fat and water precession frequency is greater, causing an even larger chemical shift artifact. To attenuate the shifted fat image, a fat suppression RF pulse is applied.

The low bandwidth in the phase direction also causes susceptibility artifacts. Magnetic susceptibility is a material property describing how a magnetic field passing through a material is either diverged or concentrated. Tissue and air have different susceptibilities, causing inhomogeneities in the magnetic field. These field inhomogeneities can cause the transverse magnetization to dephase resulting in signal elimination. Alternatively, the inhomogeneities may cause a phase shift which will geometrically distort the reconstructed image. These susceptibility artifacts are often found in the temporal lobe and in the prefrontal lobe. Fortunately, these regions of brain are outside the white matter tracts of interest in this project.

UCSF LIBRARY

3.2 Diffusion Basics

In the summer of 1827, Robert Brown used a microscope to observe the irregular motion of pollen grains suspended in water (9). While Brown did not offer an explanation for this motion, he asserted that it was not a result of bulk flow, evaporation, or the pollen being alive. In fact, the phenomenon that Brown observed was the kinetic energy of randomly moving water molecules being transferred to the pollen grain. The theory and governing equations of Brownian motion and diffusion were later developed by others including Albert Einstein (12).

3.2.1 Fundamental Diffusion Equations

Adolf Fick adapted Fourier's description of the transfer of heat into a relationship describing the diffusive flow of particles down a concentration gradient (13).

$$J = -D \frac{\partial C}{\partial x} \quad \text{Equation 3-12}$$

$$\frac{\partial C}{\partial t} = D \frac{\partial^2 C}{\partial x^2} \quad \text{Equation 3-13}$$

Equation 3-12 and Equation 3-13 comprise Fick's first and second laws of diffusion, respectively. These equations were developed empirically by Fick and state that the net flux of particles, J , is related to the concentration gradient, C . The diffusion coefficient, D , is a scalar and has units of $\text{length}^2/\text{time}$. Fick's first

UCSF LIBRARY

law, when combined with the conservation of mass principle leads to Fick's second law of diffusion.

Einstein proved that the diffusion coefficient is related to the gas constant, R, temperature, T, Avogadro's number, N, viscosity, k, and the radius of the molecules, P (12).

$$D = \frac{RT}{6\pi kPN} \quad \text{Equation 3-14}$$

The diffusion equations can be solved to express the probability that a molecule initially at position r_0 will have moved to position r after time t . The equation takes the form of a symmetric, zero mean Gaussian (Equation 3-15).

$$P(r | r_0, t) = \frac{1}{(4\pi Dt)^{\frac{3}{2}}} e^{-\frac{(r-r_0)^2}{4Dt}} \quad \text{Equation 3-15}$$

Furthermore, the mean displacement, λ_r , can be described in the case of unrestricted diffusion (Equation 3-16).

$$\lambda_r = \sqrt{6Dt} \quad \text{Equation 3-16}$$

3.2.2 Water as a Probe of Microstructure

Robert Brown and others observed individual pollen grains with the goal of learning about water diffusion. In diffusion MRI, we reverse Brown's experiment. Instead of observing macromolecules to learn about water diffusion, we study water diffusion to learn about brain structure.

Diffusion MRI aims to observe the apparent diffusion of water in biological tissue and then infer the tissue's microstructure. The diffusion coefficient, as described by Einstein, is a scalar related to environmental and material properties. The diffusion coefficient accurately describes the random movement of unrestricted water molecules. In the case of restricted diffusion, barriers will block water mobility and the mean square displacement will be reduced. The apparent diffusion coefficient, D_{eff} , combines the physical properties of the solute as described in Equation 3-14 and the nature of the barriers restricting diffusion. Water movement in brain tissue is restricted by myelin, membranes, proteins, neurofilaments, microtubules, organelles, and anything else interacting with water (4, 6, 7, 24). These barriers cause the measured apparent water diffusivity in brain tissue to be lower than the diffusivity of unrestricted water.

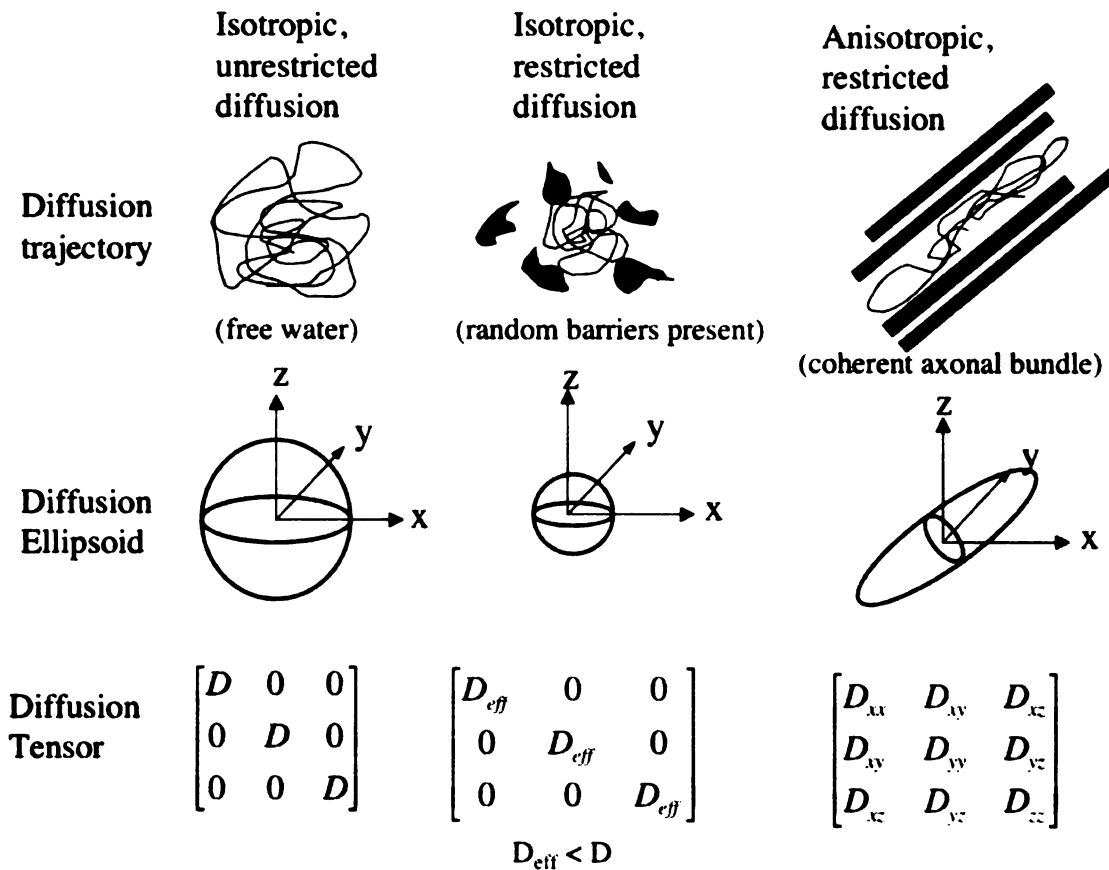
In coherently structured brain tissue, diffusion can be anisotropic, with D_{eff} being directionally dependant (1). Thus, a scalar D_{eff} cannot accurately describe the diffusion pattern of water in brain tissue. Instead, water diffusion can be modeled with the apparent diffusion tensor model.

$$\mathbf{J} = -\mathbf{D}_{\text{eff}} \nabla C$$

expanded,
$$\begin{bmatrix} J_x \\ J_y \\ J_z \end{bmatrix} = - \begin{bmatrix} D_{xx} & D_{xy} & D_{xz} \\ D_{yx} & D_{yy} & D_{yz} \\ D_{zx} & D_{zy} & D_{zz} \end{bmatrix} \cdot \begin{bmatrix} \frac{\partial C}{\partial x} \\ \frac{\partial C}{\partial y} \\ \frac{\partial C}{\partial z} \end{bmatrix}$$

Equation 3-17

Equation 3-17 and Figure 3-5 provide insight into how the diffusion tensor, D_{eff} , translates a concentration gradient into flow. In unrestricted diffusion, the off-diagonal elements of D_{eff} are zero. When diffusion is anisotropic and restricted, the off-diagonal elements describe how the concentration gradient in each direction contributes to flow in an orthogonal direction.



UCSF LIBRARY

Figure 3-5: Types of diffusion. Isotropic diffusion can be described by a scalar diffusion coefficient. Anisotropic diffusion is modeled with the diffusion tensor.

The diffusion ellipsoid is a shape that describes the mean displacement of water molecules in each direction at a particular time. For isotropic diffusion, the diffusion ellipsoid is a sphere. Anisotropic diffusion is modeled with an elongated

ellipsoid. The longest axis describes diffusivity in the direction with greatest mean water displacement.

3.3 Diffusion Tensor MRI

Diffusion tensor imaging (DTI) measures Brownian motion by tagging populations of water molecules and observing their movement. The DTI experiment is analogous to a simple diffusion experiment where a drop of dye is placed in a bowl of water. Using the Fick and Einstein equations for diffusion, the observed change in the dye's concentration can be used to calculate the diffusion coefficient of the liquid. MRI techniques sensitive to diffusion work in much the same way. A known concentration gradient of spin-labeled water molecules is established and then changes in concentration are measured over time. A gradient of spin phases is established with the diffusion spin echo pulse sequence (Figure 3-6).

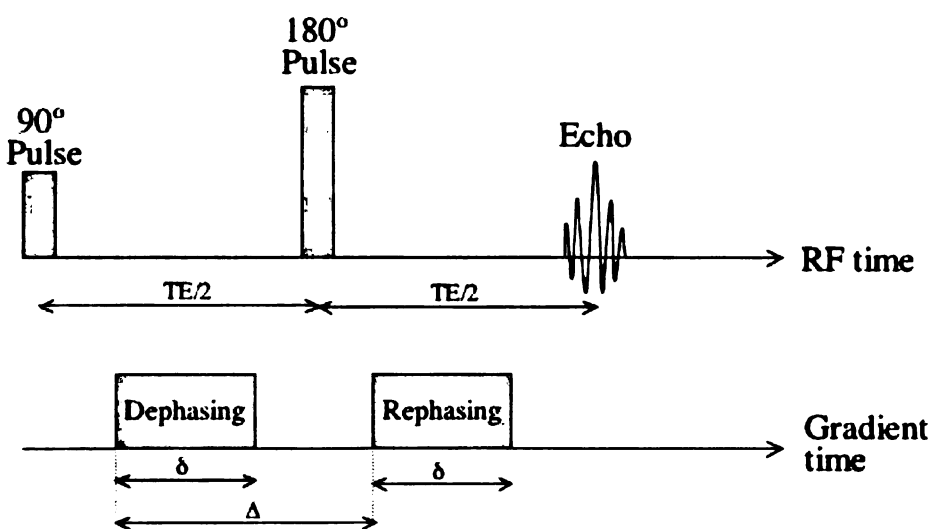


Figure 3-6: Pulsed-gradient spin echo diffusion sequence.

$$\phi_1 = \gamma \int_0^{\delta} \mathbf{G}(t) \mathbf{r}_1 dt$$

$$\phi_2 = \gamma \int_{\Delta}^{\Delta+\delta} \mathbf{G}(t) \mathbf{r}_2 dt$$

$$\phi_{dephase} = \phi_2 - \phi_1$$

Equation 3-18

In a spin-echo diffusion sequence, the protons are first excited with a 90° pulse. The protons' spins are in-phase immediately after the 90° pulse. The first diffusion gradient of amplitude $\mathbf{G}(t)$ and duration δ dephases the spin population at position \mathbf{r}_1 by ϕ_1 (Equation 3-18). The spin population is allowed to diffuse for a time period Δ between diffusion gradients. After the 180° pulse, a second diffusion gradient of amplitude $\mathbf{G}(t)$ and duration δ rephases the spins at position \mathbf{r}_2 by ϕ_2 . The second diffusion gradient pulse is identical to the first gradient pulse. If the protons in the spin population have not moved between diffusion gradients, then $\mathbf{r}_1 = \mathbf{r}_2$ for each proton and the spin population will completely rephase. If the protons have diffused, there will be a distribution of \mathbf{r}_2 values and the spin population will not completely rephase. The probability of a water molecule diffusing from position \mathbf{r}_1 to \mathbf{r}_2 in time t is described by Equation 3-19 (2, 25).

UCSF LIBRARY

$$P(\mathbf{r}_2 | \mathbf{r}_1, t) = \frac{1}{\sqrt{|\mathbf{D}_{eff}|} (4\pi t)^{3/2}} e^{-\frac{(\mathbf{r}_2 - \mathbf{r}_1)^T \mathbf{D}_{eff}^{-1} (\mathbf{r}_2 - \mathbf{r}_1)}{4t}} \quad \text{Equation 3-19}$$

Combining Equation 3-18 and Equation 3-19 leads to a signal equation relating \mathbf{D}_{eff} to the attenuation of signal S_0 . Equation 3-20 assumes rectangular diffusion gradients of amplitude G .

$$S = \int_{-\infty}^{\infty} \int_{-\infty}^{\infty} S_0 e^{iG\Delta(\mathbf{r}_2 - \mathbf{r}_1)} P(\mathbf{r}_2 | \mathbf{r}_1, t) d\mathbf{r}_1 d\mathbf{r}_2 \quad \text{Equation 3-20}$$

The effects of diffusion can also be included as a term in the Bloch-Torrey Equation (26).

$$\frac{\partial M_{xy}(t)}{\partial t} = -i\gamma(\mathbf{G} \cdot \mathbf{r})M_{xy}(t) - \frac{1}{T_2} M_{xy}(t) + \nabla^T \mathbf{D} \nabla M_{xy} \quad \text{Equation 3-21}$$

Solving the Bloch-Torrey Equation leads to an expression for the transverse magnetization.

$$M_{xy}(t) = M_{xy}(0) \left[e^{-i\mathbf{k}(t)\mathbf{r}} \right] \left[e^{\frac{-t}{T_2}} \right] \left[e^{-\int_{\tau=0}^t (\mathbf{k}^T(\tau) \mathbf{D} \mathbf{k}(\tau)) d\tau} \right] \quad \text{Equation 3-22}$$

$$\text{where: } \mathbf{k}(t) = \gamma \int_{\tau=0}^t \mathbf{G}(\tau) d\tau \quad \text{Equation 3-23}$$

UCSF LIBRARY

In a typical diffusion MR experiment with trapezoid shaped, balanced diffusion gradients, the relationship between the MR signal with and without diffusion weighting is described by Equation 3-24.

$$\frac{S}{S_0} = e^{-\left(\sum_{i=x,y,z} \sum_{j=x,y,z} b_{i,j} \mathbf{D}_{i,j}\right)} \quad \text{Equation 3-24}$$

$$\text{where: } b_{i,j} = \gamma^2 G_i G_j \left[\delta^2 \left(\Delta - \frac{\delta}{3} \right) \right] \quad \text{Equation 3-25}$$

The $\mathbf{b}_{i,j}$ matrix is related to the gradient strengths and timings and describes the sensitivity of the MR signal to diffusion. To solve for the diffusion tensor, a minimum of six diffusion weighted images with non-collinear gradients are required, in addition to the M_0 image. Using multiple linear regression, \mathbf{D}_{eff} can be determined.

3.3.1 Diffusion Tensor Parameters

The three principal components of the diffusion tensor, termed the eigenvectors, can be calculated from the diffusion tensor for each MRI voxel (2, 5).

$$\mathbf{D} \mathbf{v}_i = \lambda_i \mathbf{v}_i \quad \text{Equation 3-26}$$

Multiplying an eigenvector, \mathbf{v}_i , by \mathbf{D} is equivalent to scaling the eigenvector by λ_i . Since \mathbf{D} is positive definite and symmetric, the three eigenvectors are always orthogonal. The three eigenvectors and eigenvalues, $(\lambda_1, \lambda_2, \lambda_3)$, describe the directions and lengths of the diffusion ellipsoid axes. The eigenvalues and eigenvectors are rotationally invariant and do not depend on the laboratory

UCSF LIBRARY

coordinate system. The eigenvalues and eigenvectors can be computed by diagonalizing the diffusion tensor.

$$\Lambda = \begin{bmatrix} \lambda_1 & 0 & 0 \\ 0 & \lambda_2 & 0 \\ 0 & 0 & \lambda_3 \end{bmatrix} = \mathbf{R} \cdot \mathbf{D} \cdot \mathbf{R}^T \quad \text{Equation 3-27}$$

The diffusion tensor is rotated by matrix \mathbf{R} to produce the diagonal matrix, Λ . The columns of \mathbf{R} are comprised of the system's eigenvectors.

The primary eigenvector and associated primary eigenvalue indicate, respectively, the direction and magnitude of greatest water diffusion. In highly collimated neuronal bundles with minimal fiber crossing such as the internal capsule or corpus callosum, water diffusion will be anisotropic with the primary eigenvector oriented parallel to the axons (17, 20). The second and third eigenvectors are orthogonal to the primary eigenvector and describe diffusion transverse to axons.

A number of diffusion parameters describing the microstructure in a particular voxel can be defined with the three eigenvalues. The directionally averaged diffusion coefficient, (D_{av}), is the mean of the three eigenvalues and describes the spatially-averaged diffusivity of water in a voxel.

$$D_{avg} = \frac{\lambda_1 + \lambda_2 + \lambda_3}{3} = \text{trace}(\mathbf{D}) \quad \text{Equation 3-28}$$

LIBRARY
UNIVERSITY OF
SOUTH ALABAMA

The fractional anisotropy (FA) and relative anisotropy (RA) indexes measure the degree of directionality of diffusivity within a voxel.

$$FA = \frac{\sqrt{(\lambda_1 - \lambda_2)^2 + (\lambda_2 - \lambda_3)^2 + (\lambda_3 - \lambda_1)^2}}{\sqrt{2}\sqrt{\lambda_1^2 + \lambda_2^2 + \lambda_3^2}} \quad \text{Equation 3-29}$$

$$RA = \frac{\sqrt{(\lambda_1 - \lambda_2)^2 + (\lambda_2 - \lambda_3)^2 + (\lambda_3 - \lambda_1)^2}}{\lambda_1 + \lambda_2 + \lambda_3} \quad \text{Equation 3-30}$$

When the primary eigenvalue is much larger than the second and third eigenvalues, the anisotropy measure will be high.

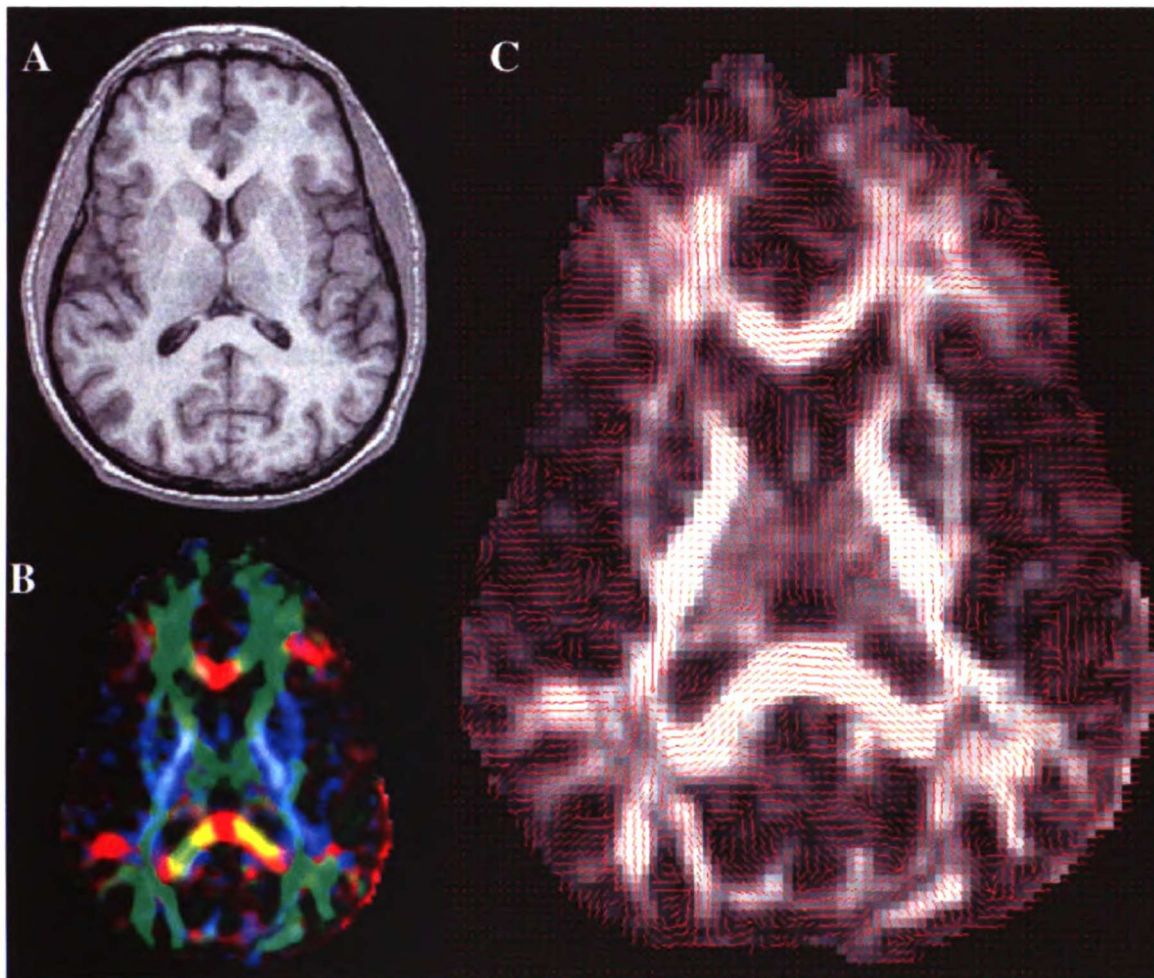


Figure 3-7: Diffusion tensor parameters. A) Conventional T1-weighted image B) Color overlay of primary eigenvector's direction. Red is Left-Right, Blue is

Superior-Inferior, Green is Anterior-Posterior. C) Vector plot of primary eigenvectors overlaid on an FA map.

3.4 Axonal Fiber Tracking with Diffusion Tensor MRI

The objective of DTI fiber tracking is to determine inter-voxel connectivity based on the anisotropic diffusion of water (3, 10, 14, 19, 21). In each brain voxel, the dominant direction of axonal tracts can be assumed to be parallel to the primary eigenvector. Fiber tracking uses each voxel's diffusion tensor to follow an axonal tract in 3D from voxel to voxel through the human brain. Since DTI only provides structural information, DTI fiber tracking is often combined with either functional or anatomical information to delineate specific pathways. Specific white matter structures such as the pyramidal, sensory, and colossal tracts can be delineated in three dimensions. The clinical and scientific utility of DTI fiber tracking is found in both the localization and quantitative assessment of specific neuronal pathways. DTI fiber tracking allows individual neuronal pathways to be quantified across regions of the brain where manual segmentation would not be possible.

Various groups have developed a number of fiber tracking algorithms (3, 10, 14, 19, 21). These algorithms can be divided into deterministic methods and probabilistic methods. However, there is some overlap between deterministic and probabilistic methods. Many of the deterministic methods can be implemented to provide a probability of connectivity metric. A brief description of some the algorithm used for this thesis project is presented in the following section. Recent comparisons between the algorithms in electronic phantoms

have not shown any of the algorithms to perform significantly better than the other methods (16).

3.4.1 Deterministic Fiber Tracking

Deterministic fiber tracking methods propagate individual trajectories from voxel to voxel through the human brain. These methods assume the diffusion tensor is an accurate representation of the underlying fiber structure and do not consider estimates of uncertainty in the tensor.

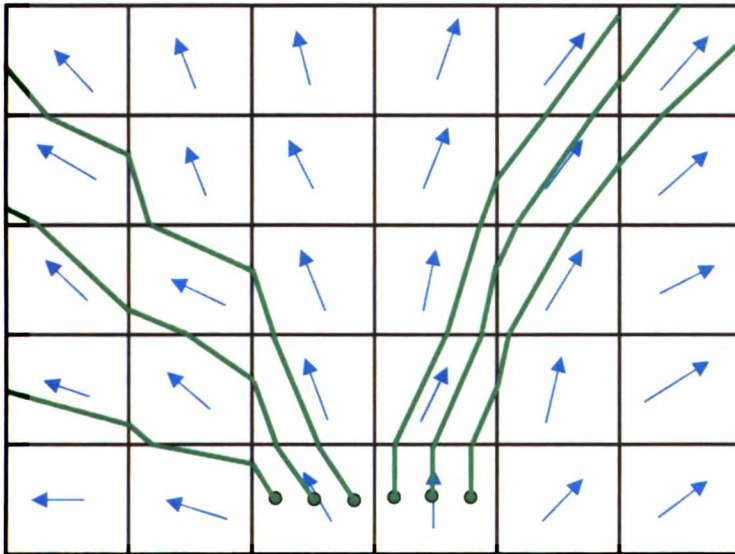


Figure 3-8: FACT algorithm in action. Blue arrows represent primary eigenvectors. Green lines are FACT trajectories.

The fiber tracking by continuous tracking (FACT) algorithm initiates fiber trajectories from user-defined voxels (Figure 3-8) (19). Fiber trajectories follow the primary eigenvector. When the fiber trajectory reaches the edge of the voxel, the trajectory's direction is changed to match the next voxel's primary

eigenvector. The trajectories are allowed to travel in continuous space across the voxel and thus the step size is variable. As seen in Figure 3-8, the starting voxels can be densely seeded with starting points. By densely seeding the starting points, the FACT algorithm can more completely delineate diverging pathways. Figure 3-9 shows a schematic example of how FACT can be used to delineate the corpus callosum. Fiber tracks are generated bidirectionally from each starting point.

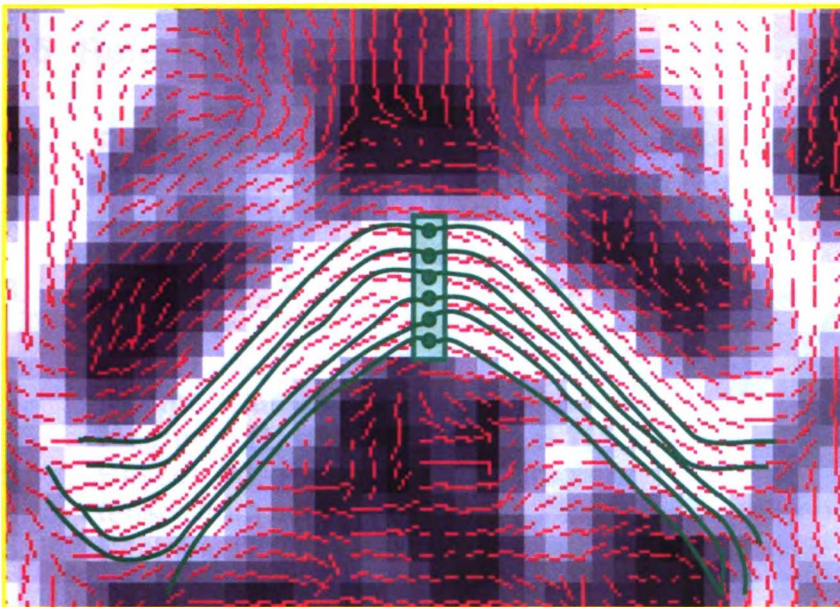


Figure 3-9: Illustrative example of deterministic FACT algorithm. The background greyscale image is the anisotropy map of the corpus callosum. The projection of the primary eigenvector on the axial plane is shown in red. A starting region for fiber tracking is represented by the green rectangle. Starting points are seeded within the starting region and fiber tracks (green lines) are propagated bidirectionally from voxel to voxel by following the eigenvector. For the purpose of clarity, all fiber tracks remain on the same axial plane in this figure.

Deterministic fiber tracking assumes there is no uncertainty in the primary eigenvector's orientation. The deterministic fiber tracking performed in this project is based on the Fiber Assignment by Continuous Tracking (FACT) algorithm developed by Mori et. al. (19). For this project, the fiber tracking software was written in Interactive Data Language (Research Systems, Boulder, CO). Interactive Data Language (IDL) is a high level programming language which allows rapid development and implementation of DTI fiber tracking tools.

3.5 References

1. Basser PJ, Mattiello J, LeBihan D: Estimation of the effective self-diffusion tensor from the NMR spin echo. **J Magn Reson B** 103:247-254, 1994.
2. Basser PJ, Mattiello J, LeBihan D: MR diffusion tensor spectroscopy and imaging. **Biophys J** 66:259-267, 1994.
3. Basser PJ, Pajevic S, Pierpaoli C, Duda J, Aldroubi A: In vivo fiber tractography using DT-MRI data. **Magn Reson Med** 44:625-632, 2000.
4. Basser PJ, Pierpaoli C: Microstructural and physiological features of tissues elucidated by quantitative-diffusion-tensor MRI. **Journal of Magnetic Resonance Series B** 111:209-219, 1996.
5. Basser PJ, Pierpaoli C: A simplified method to measure the diffusion tensor from seven MR images. **Magn Reson Med** 39:928-934, 1998.
6. Beaulieu C: The basis of anisotropic water diffusion in the nervous system - a technical review. **NMR Biomed** 15:435-455, 2002.
7. Beaulieu C, Allen PS: Determinants of anisotropic water diffusion in nerves. **Magn Reson Med** 31:394-400, 1994.
8. Bloch F, Hanson WW, Packard M: Nuclear induction. **Physical Review** 69:127, 1946.
9. Brown R: A Brief Account of Microscopical Investigations on the Particles Contained in the Pollen of Plants. **Phil. Mag.** 4:161-173, 1828.
10. Conturo TE, Lori NF, Cull TS, Akbudak E, Snyder AZ, Shimony JS, McKinstry RC, Burton H, Raichle ME: Tracking neuronal fiber pathways in the living human brain. **Proc Natl Acad Sci U S A** 96:10422-10427, 1999.
11. Damadian R: Tumor detection by nuclear magnetic resonance. **Science** 171:1151-1153, 1971.
12. Einstein A: Über die von der molekularkinetischen Theorie der Wärme geforderte Bewegung von in ruhenden Flüssigkeiten suspendierten Teilchen. **Annalen der Physik** 17:549, 1905 and again in 2005.

13. Fick A: **Ann. Phys. Chem.** 4:59-86, 1855.
14. Gossel C, Fahrmeir L, Putz B, Auer LM, Auer DP: Fiber tracking from DTI using linear state space models: detectability of the pyramidal tract. **Neuroimage** 16:378-388, 2002.
15. Haacke EM, Brown RW, Thompson MR, Ramesh V: *Magnetic Resonance Imaging Physical Principles and Sequence Design*. New York, Wiley-Liss, 1999.
16. ISMRM: Workshop on Methods for Quantitative Diffusion MRI of Human Brain. Lake Louise, Alberta, Canada, 2005.
17. Lin CP, Tseng WY, Cheng HC, Chen JH: Validation of diffusion tensor magnetic resonance axonal fiber imaging with registered manganese-enhanced optic tracts. **Neuroimage** 14:1035-1047, 2001.
18. Mansfield P: Multiplanar image formation using NMR spin echoes. **J. Phys. C: Solid State Phys.** 10:L55-L58, 1977.
19. Mori S, Crain BJ, Chacko VP, van Zijl PC: Three-dimensional tracking of axonal projections in the brain by magnetic resonance imaging. **Ann Neurol** 45:265-269, 1999.
20. Moseley ME, Cohen Y, Kucharczyk J, Mintorovitch J, Asgari HS, Wendland MF, Tsuruda J, Norman D: Diffusion-weighted MR imaging of anisotropic water diffusion in cat central nervous system. **Radiology** 176:439-445, 1990.
21. Parker GJ, Haroon HA, Wheeler-Kingshott CA: A framework for a streamline-based probabilistic index of connectivity (PICO) using a structural interpretation of MRI diffusion measurements. **J Magn Reson Imaging** 18:242-254, 2003.
22. Purcell EM, Torrey HC, Pound RV: Resonance absorption by nuclear magnetic moments in a solid. **Physical Review** 69:37-38, 1946.
23. Schmitt F, Stehling MK, Turner R: *Echo-Planar Imaging: Theory, Technique, and Application*. Berlin, Springer-Verlag, 1998.
24. Song SK, Sun SW, Ju WK, Lin SJ, Cross AH, Neufeld AH: Diffusion tensor imaging detects and differentiates axon and myelin degeneration in mouse optic nerve after retinal ischemia. **Neuroimage** 20:1714-1722, 2003.
25. Tanner JE, Stejskal EO: Restricted Self-Diffusion of Protons in Colloidal Systems by the Pulsed-Gradient, Spin-Echo Method. **The Journal of Chemical Physics** 49:1768-1777, 1968.
26. Torrey HC: Bloch Equations with Diffusion Terms. **Physical Review** 104, 1956.

Chapter 4: Parameterization of Bootstrap Analysis for Prediction of the Primary Eigenvector's Distribution

4.1 Motivation

Signal noise causes uncertainty in diffusion tensor measurements. Errors in the primary eigenvector's direction can compound and result in inaccurate DTI fiber tracks. Knowledge of the probability distribution describing the primary eigenvector's direction is important for evaluating the accuracy of fiber tracking results. Bootstrap analysis has previously been used as a model independent method of characterizing the distributions of DTI measures (4). However, the bootstrap analysis requires multiple acquisitions and intensive post-processing resources.

In this study, the bootstrap analysis was performed on the primary eigenvector's orientation and the resulting distributions are parameterized with standard DTI measures. By parameterizing the eigenvector uncertainty with standard DTI measures, a model can be developed for predicting the uncertainty without performing the entire bootstrap analysis. This chapter describes how I acquired the bootstrap DTI data, implemented bootstrap analysis software, and designed a model for predicting the primary eigenvector's distribution without performing the entire bootstrap analysis.

4.2 Introduction

Patient movement, CSF pulsation, low diffusion anisotropy, and non-linear operations affect the diffusion tensor's accuracy. Prior studies have shown the net result of these noise sources to be non-Gaussian (1, 4). The bootstrap analysis makes no assumptions about the shape of a parameter's distribution.

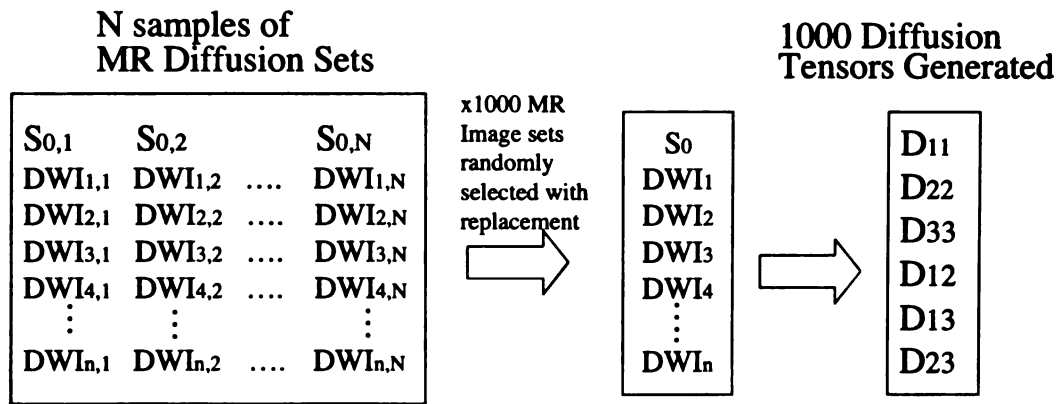


Figure 4-1: Schematic showing how $N > 1$ acquired diffusion sets can be mixed and matched to generate 1000 different diffusion tensors.

The bootstrap method randomly resamples the data from two or more independent diffusion acquisitions to generate hundreds or thousands of data sets from which diffusion parameters such as FA or the eigenvectors can be calculated (Figure 4-1). To calculate a single diffusion tensor, one set of diffusion images is required. A diffusion set includes one image volume without diffusion weighting and $n \geq 6$ diffusion weighted image volumes. Figure 4-1 shows how $N > 1$ independent acquisitions of diffusion sets can be used to generate 1000 resampled diffusion sets. The 1000 generated diffusion sets can be used to construct 1000 diffusion tensors and 1000 diffusion parameters for each voxel.

The 1000 diffusion parameters generated can be used to determine the probability density function (pdf) describing the parameter's measurement uncertainty. Prior studies have shown that 1000 bootstrap samples provides an adequate representation of a parameter's distribution (4).

4.3 Methods

4.3.1 Bootstrap Acquisition

DTI was performed at 3T, with $b=1000\text{s/mm}^2$, $TR/TE=12000/63\text{ms}$, 17 gradient directions, 1.7 isotropic voxels, and repeated 3 times. The diffusion tensor, eigenvectors ($\mathbf{v}_1, \mathbf{v}_2, \mathbf{v}_3$), and eigenvalues ($\lambda_1, \lambda_2, \lambda_3$) were calculated 1000 times with bootstrap samples selected from random combinations of the 3 acquisitions. A set of mean eigenvectors ($\mathbf{v}_{\text{avg}1}, \mathbf{v}_{\text{avg}2}, \mathbf{v}_{\text{avg}3}$) and eigenvalues ($\lambda_{\text{avg}1}, \lambda_{\text{avg}2}, \lambda_{\text{avg}3}$) was calculated after averaging the 3 DTI acquisitions together. Software for performing the bootstrap and histogram analysis was written in the C and IDL programming languages for this thesis project.

4.3.2 Histogram Analysis

The 1000 primary eigenvectors generated for each voxel are each converted to spherical coordinates (θ, ϕ, r). A 2D angular histogram of the primary eigenvectors' orientation, (θ, ϕ), with 50×50 equal angle bins was constructed for each voxel (Figure 4-2). The bootstrap software outputs 2500 DICOM volume

sets corresponding to each of the histogram bins. The number of files is massive, however, the files are easily compressed since a large percentage of the data is composed of zeroes.

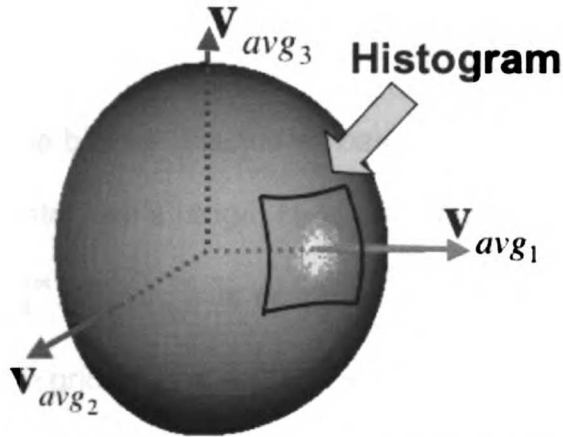


Figure 4-2: Histogram of primary eigenvectors' orientations.

An equal angle rectangular grid was chosen for histogram construction in order to simplify calculation. However, the equal angle grid contains bins with varying surface areas. For example, bins near the pole of the sphere have smaller areas than bins near the equator. To minimize the effect of the varying bin areas on distribution measurements, the histogram is always centered on spherical coordinate $(0^\circ, 90^\circ)$. A rotation matrix, \mathbf{R}_1 , is constructed for each voxel to rotate \mathbf{v}_{avg1} to the center of the histogram. A second rotation matrix, \mathbf{R}_2 , then rotates \mathbf{v}_{avg2} to point in the $(-90^\circ, 90^\circ)$ direction.

$$\mathbf{R}_1 := \text{rotation about } \frac{\mathbf{v}_{avg1} \times [1,0,0]}{|\mathbf{v}_{avg1} \times [1,0,0]|}, \text{ by } \arccos\left(\frac{\mathbf{v}_{avg1} \cdot [1,0,0]}{|\mathbf{v}_{avg1}|}\right) \text{ radians} \quad \text{Equation 4-1}$$

$$\mathbf{R}_2 := \text{rotation about } \frac{(\mathbf{R}_1 \mathbf{v}_{avg2}) \times [0,1,0]}{|(\mathbf{R}_1 \mathbf{v}_{avg2}) \times [0,1,0]|}, \text{ by } \arccos\left(\frac{(\mathbf{R}_1 \mathbf{v}_{avg2}) \cdot [0,1,0]}{|\mathbf{R}_1 \mathbf{v}_{avg2}|}\right) \text{ radians} \quad \text{Equation 4-2}$$

$$\mathbf{R}_3 = \mathbf{R}_2 \mathbf{R}_1 \quad \text{Equation 4-3}$$

The combined rotation matrix, \mathbf{R}_3 , is calculated for each voxel. \mathbf{R}_3 is used to rotate each of the 1000 bootstrapped primary eigenvectors, \mathbf{v}_1 , into the histogram's coordinate system.

$$\mathbf{v}_1^{\text{rot}} = \mathbf{R}_3 \mathbf{v}_1 \quad \text{Equation 4-4}$$

The bin size is adjusted based on each voxel's fractional anisotropy to ensure the histogram's range, H_{FOV} , encompasses the entire distribution. The orientation of $\mathbf{v}_1^{\text{rot}}$, $(\theta_{v_1}, \phi_{v_1})$, is assigned a bin according to Equation 4-5, assuming a 50x50 bin grid.

$$\theta_{bin} = \text{truncate} \left[\frac{(\theta_{v_1} + 90^\circ)}{\left(\frac{H_{FOV}}{50}\right)} \right]$$

$$\phi_{bin} = \text{truncate} \left[\frac{\left(\phi_{v_1} - \left(\frac{180^\circ - H_{FOV}}{2} \right) \right)}{\left(\frac{H_{FOV}}{50}\right)} \right] \quad \text{Equation 4-5}$$

Note that information about the primary eigenvectors' magnitudes is not preserved. Only the orientations of the eigenvectors' are studied because of their relevance to fiber tracking accuracy.

Each voxel's distribution is fitted to a 2D elliptical Gaussian equation using a non-linear least squares method to determine A_0 , A_1 , θ_{ax} , and ϕ_{ax} (Equation 4-6).

MAY 15 2011 10:50 AM

$$F(\theta, \phi) = A_0 + A_1 e^{\frac{-U}{2}}$$

$$\text{where, } U = \left(\frac{\theta}{\theta_{ax}}\right)^2 + \left(\frac{\phi}{\phi_{ax}}\right)^2 \quad \text{Equation 4-6}$$

The 2D elliptical Gaussian function was chosen because it captures the asymmetry of the angular distribution in the θ and ϕ directions with the θ_{ax} and ϕ_{ax} axis lengths. The three eigenvalues and residual error from the tensor fit, calculated from the 3 NEX averaged DTI set, were used as the independent variables in a multiple linear regression to each of the parameters, A_0 , A_1 , $\ln(\theta_{ax})$ and $\ln(\phi_{ax})$. The percent overlap between the bootstrap distribution and $F(\theta, \phi)$ was calculated to quantify the goodness of fit between the angular histogram and the Gaussian model.

The three eigenvalues (λ_{avg1} , λ_{avg2} , λ_{avg3}), $\frac{\lambda_{avg1}}{\lambda_{avg1} - \lambda_{avg2}}$, and $\frac{\lambda_{avg1}}{\lambda_{avg1} - \lambda_{avg3}}$ as calculated with the 3 NEX averaged DTI set, were used as the independent variables in a multiple linear regression to each of the parameters, A_0 , A_1 , $\ln(\theta_{ax})$ and $\ln(\phi_{ax})$.

4.4 Results

4.4.1 Bootstrap Histograms

Figure 4-3 shows example angular distribution histograms from three representative voxels in the brain. The four degrees of freedom in the 2D elliptical Gaussian are capable of modeling the asymmetric angular distributions.

In the voxel chosen from the genu of the corpus callosum, the primary eigenvector's histogram is tightly distributed and symmetric. In association pathways and frontal white matter, the primary eigenvector was observed to have a wider and asymmetric distribution. The angular distribution of the primary eigenvector is elongated in the θ direction in white matter with more complex fiber architecture and $\lambda_1 = \lambda_2 > \lambda_3$.

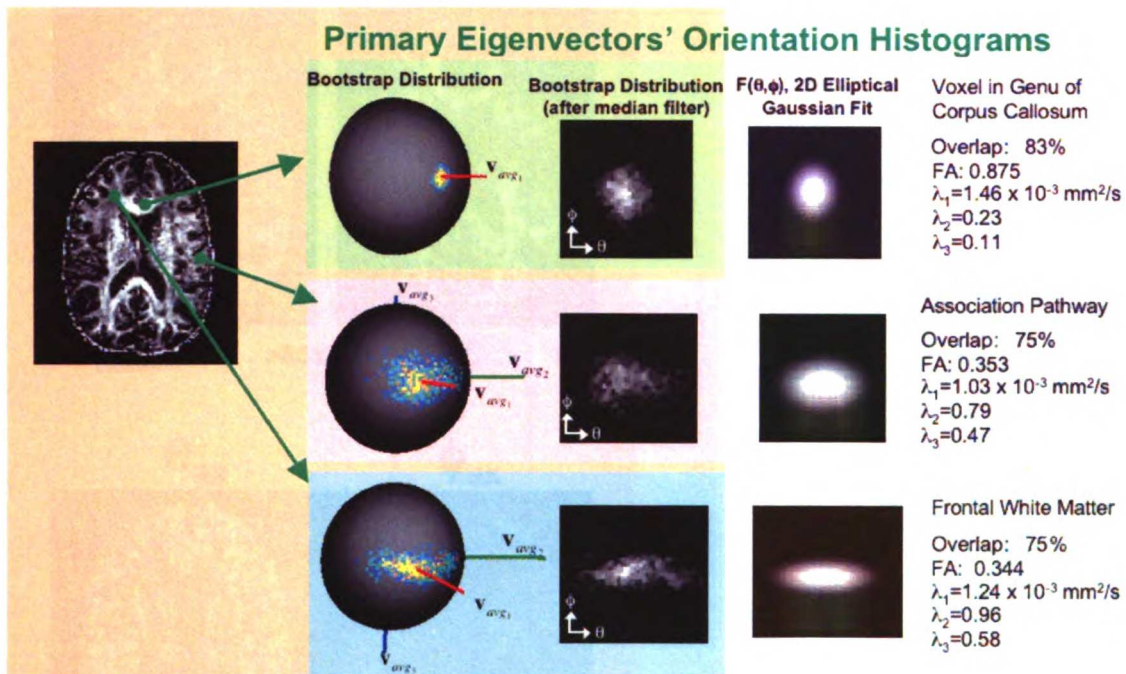


Figure 4-3: Example distributions of the primary eigenvector in three voxels. In a highly anisotropic corpus callosum voxel, the distribution is tight and symmetric. In the more complex white matter in the frontal lobe, the distribution is elongated and more dispersed. The 2D Gaussian fits for each voxel are also shown.

4.4.2 Elliptical Fit of Histograms

Figure 4-4 shows maps characterizing the 2D elliptical Gaussian fit to the bootstrap distributions. The percent overlap between the bootstrap and Gaussian distributions is highest in the white matter regions of the brain. The θ_{ax}

and ϕ_{ax} variables are lowest in the corpus callosum and internal capsule. In other less anisotropic white matter regions, both θ_{ax} and ϕ_{ax} are observed to increase. However, θ_{ax} is consistently larger than ϕ_{ax} , indicating the asymmetry of the angular distribution.

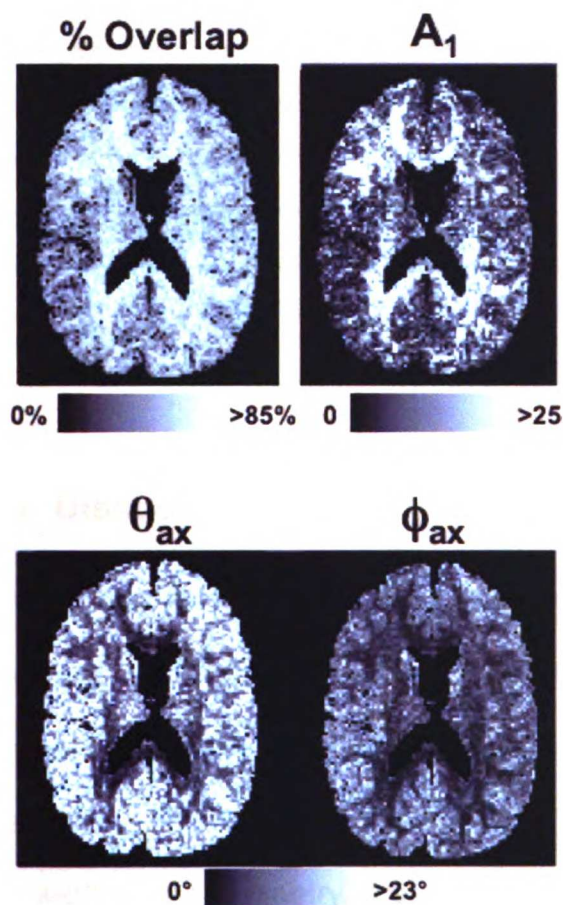


Figure 4-4: Maps describing the fit the 2D elliptical Gaussian to the bootstrap distributions.

Table 4-1 shows the correlation of the Gaussian model variables to the standard DTI parameters. The mean value of A_0 , the offset constant, was zero and was uncorrelated. The residual error of the fit to determine the tensor elements was

UCSF LIBRARY

also uncorrelated. The width of the Gaussian in the θ direction was most correlated with λ_{avg1} and λ_{avg2} . The width of the Gaussian in the ϕ direction was most correlated with λ_{avg1} and λ_{avg3} .

Parameter	Multiple Correlation Coefficient	λ_{avg1} Correlation Coefficient	λ_{avg2} Correlation Coefficient	λ_{avg3} Correlation Coefficient	$\frac{\lambda_{avg1}}{\lambda_{avg1} - \lambda_{avg2}}$ Corr. Coef.	$\frac{\lambda_{avg1}}{\lambda_{avg1} - \lambda_{avg3}}$ Corr. Coef.
$\ln(\theta_{ax})$	0.695	-0.417	0.255	0.202	0.290	0.502
$\ln(\phi_{ax})$	0.651	-0.363	0.119	0.315	0.157	0.583
A_1	0.644	0.567	0.0407	0.0707	-0.261	-0.476
A_0	0.294	-0.152	0.0977	0.129	0.139	0.266

Table 4-1: Regression of DTI parameters to 2D elliptical Gaussian fit parameters.

4.5 Discussion

Prior studies have shown the advantages of bootstrap based fiber tracking (2, 3). However, the bootstrap analysis is impractical for routine, clinical applications because of the necessity for multiple acquisitions and intensive post-processing resources. The model of the bootstrap distribution used in this study can capture the width and asymmetry in the primary eigenvector's angular uncertainty. The 2D elliptical Gaussian model uses 4 degrees of freedom to describe the shape of the primary eigenvector's angular distribution. Using the standard DTI eigenvalues, the 2D elliptical shape can be estimated and used in Monte-Carlo based probabilistic fiber tracking (5) without a bootstrap acquisition.

UNIVERSITY OF
 MICHIGAN
 LIBRARY

The remaining chapters in this thesis project assess the accuracy of DTI fiber tracking and determine the feasibility of using the technique for clinical applications. The work I completed for this chapter contributed to our understanding of the types of errors that can be encountered with DTI fiber tracking. DTI fiber tracks can be generated anywhere in the brain, however, the bootstrap methods predict where fiber tracking is likely to be accurate and where fiber tracking will fail. In Chapter 5, quantitative DTI fiber tracking is tested within the internal capsule and cerebral peduncle of hemiplegic patients. These regions of the brain have tight primary eigenvector distributions, leading to a low amount of uncertainty in DTI fiber tracks.

4.6 References

1. Heim S, Hahn K, Samann PG, Fahrmeir L, Auer DP: Assessing DTI data quality using bootstrap analysis. **Magn Reson Med** 52:582-589, 2004.
2. Jones DK, Pierpaoli C: Confidence mapping in diffusion tensor magnetic resonance imaging tractography using a bootstrap approach. **Magn Reson Med** 53:1143-1149, 2005.
3. Lazar M, Alexander AL: Bootstrap white matter tractography (BOOT-TRAC). **NeuroImage** 24:524-532, 2005.
4. Pajevic S, Basser PJ: Parametric and non-parametric statistical analysis of DT-MRI data. **J Magn Reson** 161:1-14, 2003.
5. Parker GJ, Haroon HA, Wheeler-Kingshott CA: A framework for a streamline-based probabilistic index of connectivity (PICO) using a structural interpretation of MRI diffusion measurements. **J Magn Reson Imaging** 18:242-254, 2003.

WEST LIBRARY

Chapter 5: Quantitative DTI Fiber Tracking of the Corticospinal Tract in Patients with Congenital Hemiplegia

5.1 Motivation

The goal of this study is to develop a method of using DTI fiber tracking to locate and quantify the motor tract in patients with congenital hemiplegia. While visual inspection of 3D fiber tracts can provide important qualitative information on the characteristics and pathology of the corticospinal tract, a more quantitative method is desirable (3). Hemiplegic patients comprise an appropriate population for testing DTI fiber tracking methods because the unaffected side of the brain serves as an internal control.

For this study, I wrote software to perform DTI fiber tracking based on an algorithm described in the literature. In addition, I developed software which performs tract-specific measurements based on the location of DTI fiber tracts. To display DTI fiber tracks in 3D, visualization tools were developed. Using these quantitative tools, diffusion parameters such as anisotropy, ADC, and the individual eigenvalues were measured within the motor tract. This study determined that the quantitative fiber tracking tools developed for this thesis project are sensitive enough to detect damage to white matter pathways in this patient population.

5.2 Methods

5.2.1 DTI acquisition

Patients were examined on a 1.5T General Electric scanner. Images were acquired using an echo planar sequences with TR=8 s, TE = 97.8 ms, FOV =360x180 mm, voxel size of 1.4 x 1.4 mm, and a slice thickness of 3 mm. No gaps were present between slices. MR volumes contained 28 image slices that spanned from the superior pons through the superior aspects of the corona radiata. Six diffusion weighted images with b=1000 s/mm² and one baseline image with b=0 s/mm² were acquired. Stejskal-Tanner diffusion gradients were applied in six different directions in a tetrahedral pattern. All studies were averaged over six acquisitions (NEX=6) to improve the signal to noise ratio. Total acquisition time was approximately 18 minutes. The diffusion tensor and DTI parameters were calculated as described in other works.

5.2.2 Patient and Control Population

Five cases of congenital hemiplegia were studied and were aged 10 months, 1, 2, 3, and 8 years (Table 5-1). Among the cases, motor weaknesses were evenly distributed between left and right side deficiencies. Two of the cases (ages 2 and 3 years) had unilateral polymicrogyria. Table 5-1 indicates the degree of motor weakness observed during testing by a neurologist. Five age-matched controls were used to establish a normal benchmark for left-right corticospinal tract measurement asymmetry. Controls were scanned for evaluation of

retinoblastoma, macrocephaly, or family history of vascular anomalies. All controls had normal neurological exams and no motor deficiencies.

Patient #	Age	Motor Weakness
1	10 months	Mild Normal motor exam 2 months after MR
2	14 months	Moderate
3	2 years	Moderate Unilateral polymicrogyria
4	3 years 6 months	Moderate Unilateral polymicrogyria
5	8 years	Mild

Table 5-1: Hemiplegic patient population.

5.3 Fiber Tracking

The fiber tracking algorithm used was based on the fiber assignment by continuous tracking (FACT) method (5). The primary eigenvectors of the diffusion tensors were followed bidirectionally until the relative anisotropy (RA) fell below a threshold of 0.04 or the tract turned at an angle above a set threshold of 41°. Each voxel in the starting region was densely seeded with 25 coplanar starting points for tracking. The starting points were equally spaced in a plane intersecting the center of the voxel and perpendicular to the superior-inferior direction. By densely seeding the starting region, the full extent of diverging tracts can be more accurately determined.

AMBENT
 WEST LIBRARY
 1000

The fiber tracking software developed for this thesis project was implemented using Interactive Data Language (IDL, Research Systems, Boulder, CO). A user-friendly graphical interface allows the DTI data set and regions of interest to be read. The user can control fiber tracking thresholds. The output is typically DTI fiber tracks overlaid on the b=0 echo planar image. The software can also use the delineated fiber tracks to take tract-specific measurements of RA, eigenvalues, or any other map. Measurements are outputted directly onto spreadsheets for analysis.

5.3.1 Selection of fiber tracking ROIs

The corticospinal tract (CST) was tracked by using a starting region in the caudal cerebral peduncle. The length of the cerebral peduncle was measured and the middle third used as the starting region. Tracks originating in the starting region and passing through a target region in the posterior limb of the internal capsule (PLIC) at the level of the globus pallidus were retained and used for analysis. All starting and target regions were drawn based on T2 weighted images and anisotropy maps before tracking was performed. All regions were measured and drawn by a neuroradiologist.

5.3.2 Quantitation of DTI Parameters

Diffusion parameters were measured from voxels through which the tracts passed between and including the starting and target region. Between the

UNIVERSITY OF TORONTO LIBRARY

cerebral peduncle and PLIC at the level of the globus pallidus, the CST is primarily a distinct fiber bundle and partial voluming effects are expected to be minimal. To attenuate the effects of stray tracts, measurements were weighted by the number of tracks passing through each voxel. Relative anisotropy (RA), mean diffusivity (D_{av}), the primary eigenvalue, and the mean of the two minor eigenvalues, were measured in the corticospinal tract based on the position of the fiber tracks. The minor eigenvalues indicates the diffusivity transverse to axonal bundles.

Left to right asymmetries of brain anatomy and measured diffusion parameters are expected in the normal brain. Benchmarks of normal percent asymmetry were established based on the control population. The mean magnitude of the percent asymmetry of diffusion parameters was calculated. These normal asymmetry magnitudes were then compared to the magnitude of asymmetry found in each of the hemiplegic cases.

5.4 Results

5.4.1 Qualitative Analysis

Figure 5-1 shows the left and right DTI fiber tracks for hemiparetic patient #5. The fiber tracks pass from the cerebral peduncle to the posterior limb of the internal capsule, following the expected course of the motor pathway. Figure 5-2 shows a three-dimensional plot of the left and right corticospinal tract of a one

year old hemiplegic patient. The tract affected by hemiplegia was marked with an arrow. The starting and target regions were outlined in green. The affected tract appeared thinner and less extensive than the unaffected CST. In addition, an overall decrease in anisotropy was visible along the affected tract.

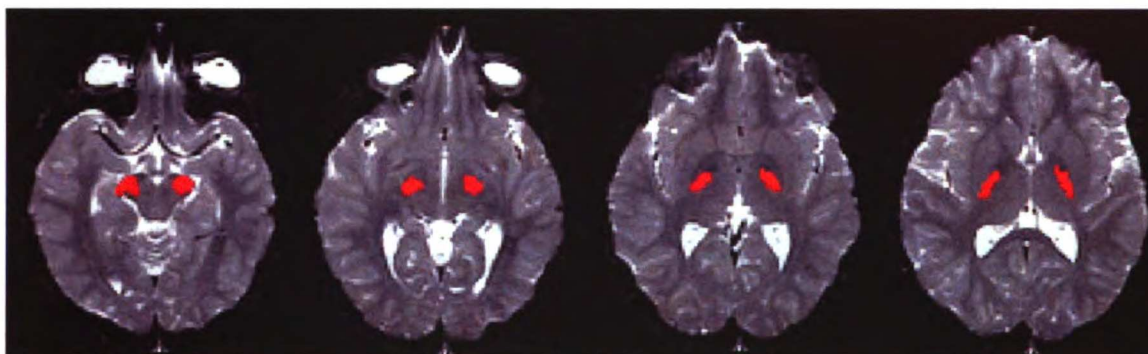


Figure 5-1: Fiber tracks (red) of a hemiparetic patient (age 8 years) are shown overlaid on b=0 EPI images. DTI fiber tracks are seen coursing from the cerebral peduncle through the internal capsule.

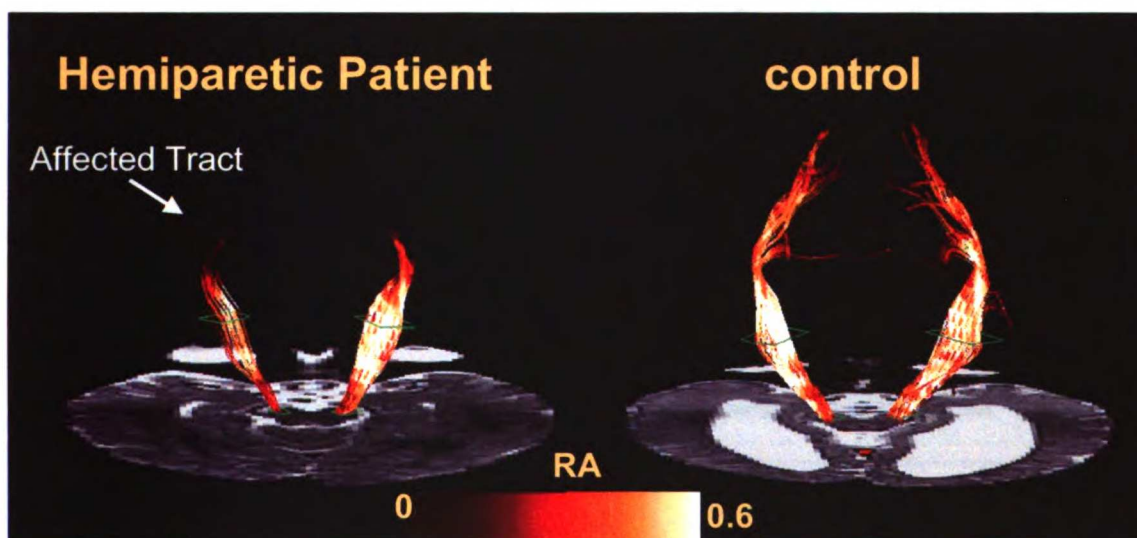


Figure 5-2: 3D fiber tracks of a hemiparetic patient (#2) with moderate motor deficit and an age-matched control are shown with an EPI slice through the cerebral peduncle. Starting and target regions are shown in green. Fiber tracks are color coded by the underlying RA.

5.4.2 Asymmetry in Patients

Figure 5-3 compares measurements from affected and unaffected tracts in hemiparetic patients along with measurements from the age matched controls. Moderate motor weakness was associated with decreased primary eigenvalues and increased transverse diffusivity. Asymmetry of RA in patients with congenital hemiplegia was greater than asymmetry in age-matched controls ($p < 0.03$, paired t-test).

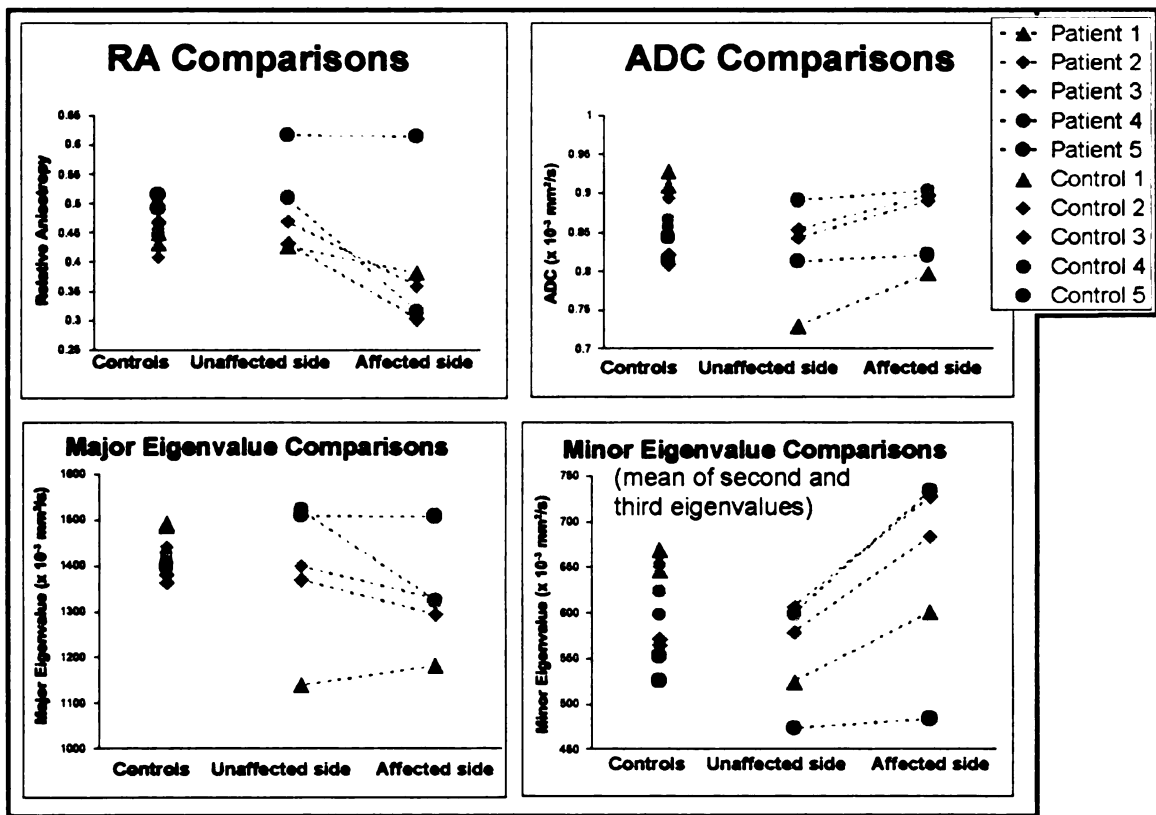


Figure 5-3: Diffusion parameter comparisons. Measurements from controls are shown along with measurements from both unaffected and affected motor tracts in hemiplegic patients. Patients and their age matched controls share symbols.

Figure 5-4 compares Z-scores between patients with mild and moderate hemiparesis. The Z-scores indicate the amount of asymmetry based on the control population's left-right tract measurement asymmetry. Patients with moderate hemiparesis have greater left to right tract asymmetry of measured RA, primary eigenvalues and minor eigenvalues.

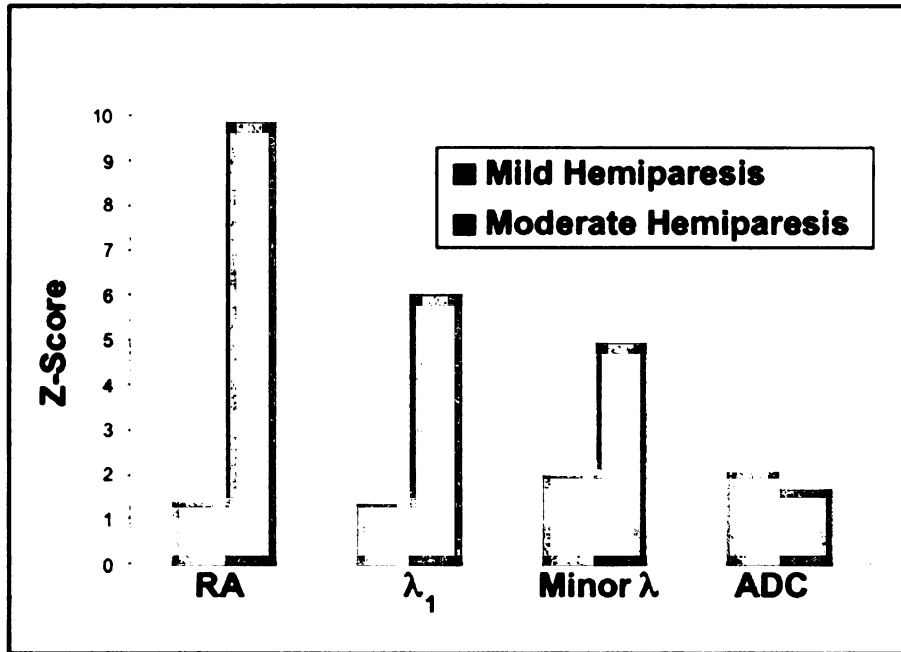


Figure 5-4: Asymmetry of DTI parameters related to severity of hemiparesis.

5.4.3 Anisotropy Changes with Age

Figure 5-5 shows RA increased with age among the control population at a rate of 9.8×10^{-3} RA/year. All hemiparetic tract measurements were more than 2 standard deviations from normal tracts.

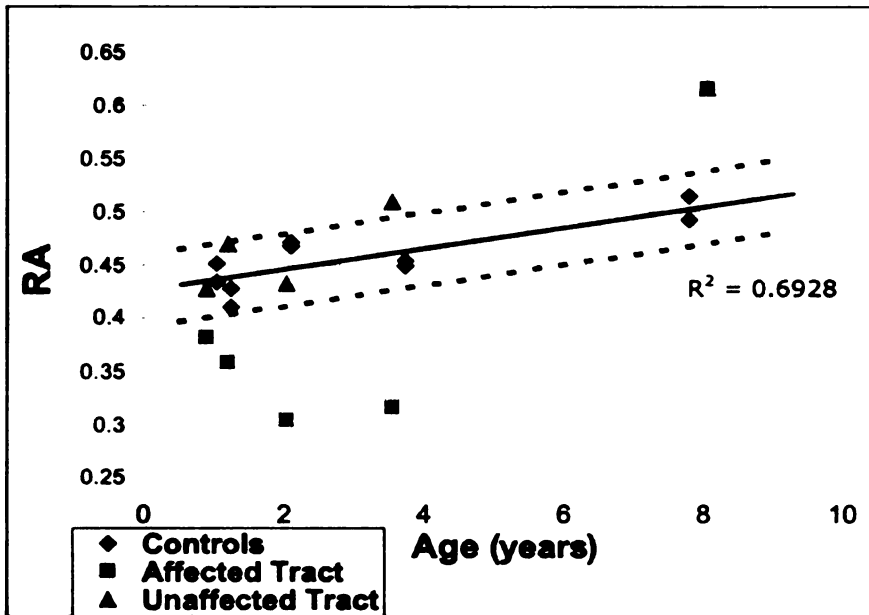


Figure 5-5: Relative anisotropy as a function of age. The regression line was fitted to control measurements. The dotted lines indicate two standard deviations about the regression line.

5.5 Discussion

In this study, I have developed a method of quantitatively studying the pediatric corticospinal tract with DTI fiber tracking. The method uses densely seeded starting points in the cerebral peduncle and the tracks are filtered with a target region drawn in the PLIC. Fiber tracking allows measurement of the CST across slices where the location of the tract is not visibly obvious. Large asymmetries of diffusion parameters were noted, indicating structural asymmetry. Possible causes of lower anisotropy and higher transverse diffusivity are changes in the structure, density, and organization of axons (1, 2, 7). These types of changes are consistent with the neurological damage expected in patients with motor weakness. In the control subjects, anisotropy of the motor tract increased with

age. This trend is a result of white matter maturation and is consistent with prior studies using manually drawn regions of interest (4, 6).

This study focused on a small section of the motor tract between the cerebral peduncle and internal capsule. High anisotropy and few crossing pathways characterize this portion of the motor tract. Thus, fiber tracking is expected to be relatively accurate between the cerebral peduncle and internal capsule. However, analysis of additional regions of the motor tract could lead to more sensitive measurements indicating the severity and location of white matter tract damage. In Chapter 6 and Chapter 7, DTI fiber tracking of the motor pathway through the entire cerebrum is validated with intraoperative stimulations. The results of Chapter 6 and Chapter 7 provide the groundwork for Chapter 9's quantitative study of white matter development in premature infants.

5.6 References

1. Beaulieu C: The basis of anisotropic water diffusion in the nervous system - a technical review. **NMR Biomed** 15:435-455, 2002.
2. Beaulieu C, Allen PS: Determinants of anisotropic water diffusion in nerves. **Magn Reson Med** 31:394-400, 1994.
3. Hoon AH, Lawrie WT, Melhem ER, Reinhardt EM, van Zijl PCM, Solaiyappan M, Jiang H, Johnston MV, Mori S: Diffusion tensor imaging of periventricular leukomalacia shows affected sensory cortex white matter pathways. **Neurology** 59:752-756, 2002.
4. Huppi PS, Maier SE, Peled S, Zientara GP, Barnes PD, Jolesz FA, Volpe JJ: Microstructural development of human newborn cerebral white matter assessed in vivo by diffusion tensor magnetic resonance imaging. **Pediatr Res** 44:584-590, 1998.
5. Mori S, Crain BJ, Chacko VP, van Zijl PC: Three-dimensional tracking of axonal projections in the brain by magnetic resonance imaging. **Ann Neurol** 45:265-269, 1999.

6. Neil JJ, Shiran SI, McKinstry RC, Schefft GL, Snyder AZ, Almli CR, Akbudak E, Aronovitz JA, Miller JP, Lee BC, Conturo TE: Normal brain in human newborns: apparent diffusion coefficient and diffusion anisotropy measured by using diffusion tensor MR imaging. **Radiology** 209:57-66, 1998.
7. Song SK, Sun SW, Ju WK, Lin SJ, Cross AH, Neufeld AH: Diffusion tensor imaging detects and differentiates axon and myelin degeneration in mouse optic nerve after retinal ischemia. **Neuroimage** 20:1714-1722, 2003.

Chapter 6: DTI Fiber Tracking from Motor Points Defined by Intraoperative Cortical Stimulation

6.1 Abstract

The goal of this study is to use magnetic resonance diffusion tensor imaging (DTI) fiber tracking combined with cortical stimulation mapping to delineate the descending motor pathway (4). The measurements I performed in Chapter 5 were restricted to the internal capsule and cerebral peduncle. This chapter serves to validate the ability of DTI fiber tracking to delineate the motor tract through the entire cerebrum through correlations with a functional mapping technique. In addition, this work presents the clinical relevance of DTI fiber tracking in brain tumor patients. Subcortical localization of the motor pathway in relation to a glioma may provide critical information to help guide tumor resection and prevent surgical morbidity.

This chapter describes a patient study I conducted using the DTI fiber tracking tools developed for Chapter 5. Eleven adult patients with gliomas underwent MR imaging one day prior to image-guided intraoperative cortical motor mapping and resection. DTI fiber tracks of the descending motor pathway were launched from 27 cortical motor sites identified stereotactically during intraoperative cortical mapping. The position and organization of DTI fiber tracts were visualized with both freely available software and software I developed for this project. Fiber tracking from 16 motor stimulation sites followed descending

pathways from the precentral gyrus, through the corona radiata, internal capsule, and into the cerebral peduncle. DTI fiber tracks were also observed to diverge along crossing white matter bundles (4 cases) and to terminate or deviate in regions of peritumoral vasogenic edema (5 cases). The subcortical fiber tracks generated are consistent with the known anatomical course and somatotopic organization of the motor tract in relation to its cortical origins.

6.2 Introduction

Removing glial neoplasms within or adjacent to functional pathways subserving motor function carries with it a risk of injuring subcortical fibers emanating from the primary motor cortex. Prior to removing a lesion in this critical area, functional mapping with magnetic source imaging, functional MRI, or intraoperative electrical stimulation of the exposed cortex can be utilized to identify the Rolandic cortex (16-18). These mapping strategies provide a safety margin to the surgeon during a radical tumor resection; however, localization is largely limited to the grey matter. Intraoperative stimulation mapping can be used to identify subcortical motor pathways subserving the motor cortex, however the procedure is invasive, complex and time consuming (Figure 6-1) (2, 3, 7). The ability to localize the subcortical pathways preoperatively with an imaging modality would be highly advantageous, especially if this data is incorporated into a navigational workstation to be used during the tumor removal.

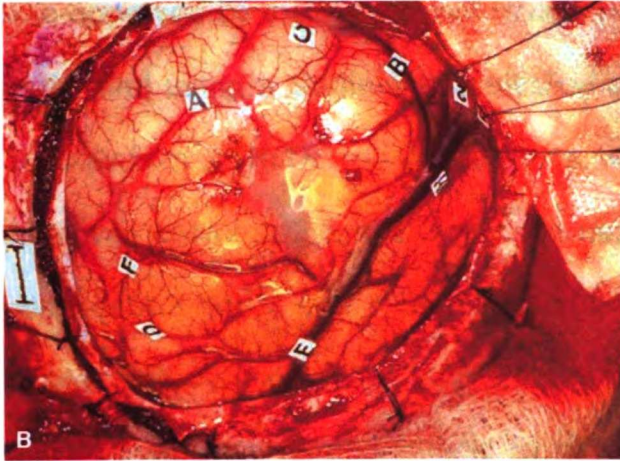


Figure 6-1: Human brain cortex exposed after craniotomy and removal of the dura, but before resection.

To delineate a specific neural pathway with DTI fiber tracking in the complex architecture of the brain requires some prior knowledge of the tract's origin. The purpose of this study is to use motor sites identified by intraoperative cortical stimulation to launch DTI fiber tracking of the subcortical motor pathways.

6.3 Methods

6.3.1 MR Imaging

This study included eleven consecutive adult patients with gliomas who underwent MR imaging one day prior to intraoperative cortical motor mapping and image-guided resection. The patients consisted of six men and five women with a mean age of 40.5 years. A mix of tumor grades and locations were included as summarized in Table 1. MR scans were performed on a 1.5T General Electric Signa scanner (General Electric, Milwaukee WI). The protocol

was approved by the institutional review board at our medical center. DTI was performed using a single-shot multislice spin echo echoplanar sequence with $b=1000\text{s/mm}^2$, TR/TE = 10000/100ms, 4 to 6 averaged acquisitions, slice thickness between 2 and 2.3 mm, no gap between slices, and voxel volume between 4.5 and 9 mm^3 . Six diffusion gradient directions and one image set without diffusion weighting ($b=0\text{ s/mm}^2$) were acquired. Acquisition coverage was from the cerebral peduncle to the brain vertex. The diffusion tensor, eigenvectors, eigenvalues, and relative anisotropy were calculated as described elsewhere using in-house software written in the C programming language (1). T2-weighted fast spin echo (FSE) and post-contrast T1-weighted spoiled gradient echo (SPGR) images were also acquired for use with the image guided surgical navigation system.

6.3.2 Cortical Stimulation and Stereotactic Registration

Direct cortical stimulation of the patients' exposed cortex was performed to identify the cortical sites of origin for motor function. Stimulation was performed with a 5 mm wide bipolar electrode that produces a small electric current to depolarize cortical neurons. This elicits motor responses in muscle groups in the extremities, which are monitored with electromyographic recordings (20). Motor points on the cortex were stereotactically identified on FSE or SPGR MR images during the operation but prior to resection using the StealthStation surgical navigation system (Medtronic, Broomfield CO). The stereotactic probe is positioned on the stimulation site and viewed on the navigation system's screen

(Figure 6-2a). Screen saves from the navigation system showing axial, coronal, and oblique trajectory views of the stimulation point were saved for later use with DTI fiber tracking.

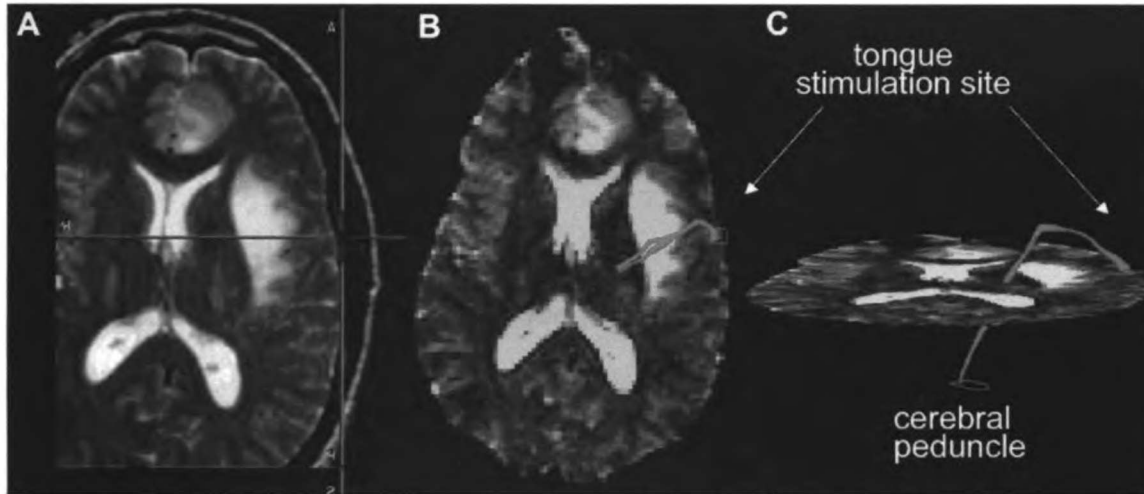


Figure 6-2: Fiber tracking from stereotactically identified motor site. A) Surgical navigation screen save of a tongue motor site in patient 11. The center of the cross-hairs indicates the position of the tip of the stereotactic probe on T2-weighted FSE MR images. B) The corresponding axial echo planar image from the DTI set with the square starting region (arrow) and 3D fiber tracks (red). C) Coronal projection of fiber tracks connecting the cortex with the cerebral peduncle. The outline of the region drawn in the cerebral peduncle for filtering the fiber tracks is shown.

6.3.3 Fiber Tracking

After completion of the surgery, screen saves showing the location of stimulation sites on FSE or SPGR images are downloaded from the navigation system. The navigation images and DTI are acquired during the same MR exam so a common coordinate system exists. The stimulation points were transferred to the echo planar DTI volume using the common coordinate system. The transferred stimulation sites were visually checked to ensure an accurate match between

echo planar DTI and navigational image volumes. A 6x6 mm square drawn at the stimulation site on the echo planar image without diffusion weighting was used as the starting region for DTI fiber tracking (Figure 6-2b). Fiber tracking trajectories were launched from multiple points within every voxel in the starting region. Each voxel inside the starting region contained 64 evenly spaced starting points distributed in a 4 x 4 x 4 cubic grid. Fiber tracks were generated from each individual starting point within the stimulation site.

DTI fiber tracking software was written in Interactive Data Language (Research Systems Inc., Boulder CO) and run on a SunBlade 150 workstation (Sun Microsystems, Santa Clara CA). The fiber tracking method was based on fiber assignment by continuous tracking (FACT)(13). The 3D fiber track is allowed to continue from voxel to voxel until it enters a region of relative anisotropy less than 0.014, turns an angle greater than 70 degrees, or exits the brain. Generating fiber tracks from a stimulation site requires less than a minute of computer processor time.

In each case, the cerebral peduncle was identified and manually outlined on the echo planar images. If DTI fiber tracks reached the cerebral peduncle, spurious tracks not passing through the cerebral peduncle were excluded (6) (Figure 6-2c). In cases which no DTI fiber tracks reached the cerebral peduncle, all generated tracks were retained for analysis.

11/10/11 10:10 AM

6.4 Results

A total of 28 cortical motor stimulation sites were identified on the 11 patients. An average of 2.6 motor sites with a range of 2 to 3 were found in each patient. Muscle responses observed included mouth, tongue, shoulder, arm, wrist, hand, finger, trunk, and leg motions. These intact motor responses were spread over the motor homunculus and represented both the corticospinal and corticobulbar tracts. One shoulder stimulation site could not be used for fiber tracking because it was at the extreme vertex of the brain and the axial surgical navigation system image contained no brain landmarks such as sulci that could be located on the echo planar images. Figure 6-2(a-c) shows a tongue motor stimulation site transferred from the surgical navigation system to the DTI set and the resulting fiber tracks connecting the cortex with the cerebral peduncle.

Four of the patients exhibited pre-operative motor functional impairments. Patients 2 and 5 exhibited motor weakness. Patient 4 had upper extremity shaking and patient 6 exhibited upper extremity pronator drift. The remainder of the patients showed no motor deficits prior to surgery.

6.4.1 Motor Pathway Delineated with Diffusion Tensor Fiber Tracking

Results of fiber tracking from each of the stimulation points are summarized in Table 6-1. DTI fiber tracking from 16 motor sites coursed from the cortex, into the corona radiata, posterior limb of the internal capsule, and entered the cerebral peduncle. Fiber tracks originating from two sites terminated within the

corona radiata. The pathway of the descending fiber tracks matched the known anatomical locations of the corticospinal and corticobulbar tracts (12).

WJL LIDIAN

Patient Number	Gender/age	Tumor Location and Type	Motor Site	DTI Tracking Result
1	M / 41	Left frontal grade2 gemistocytic astrocytoma.	Mouth 1	Descends through CR, IC, to CP
			Mouth 2	Descends through CR, IC, to CP
			Jaw	Descends through motor gyrus to CR
2	F / 32	Left parieto-occipital grade 2 oligodendroglioma	Finger Flexion	Descends through motor gyrus and diverges posteriorly in region of edema
			Hand Wrist Thumb Finger Flexion	Descends through motor gyrus, and terminates in edema
			Wrist Finger Flexion	Descends through motor gyrus and diverges posteriorly in region of edema
3	F / 33	Left temporal grade 2 oligodendroglioma; recurrence of grade 3 oligoastrocytoma	Mouth 1	Descends through CR, IC, to CP
			Mouth 2	Descends through CR, IC, to CP
4	F / 44	Left frontal grade 2 oligoastrocytoma	Wrist Flexion	Descends through motor gyrus to SLF
			Hip Flexion	Descends through CR, IC, to CP
5	F / 40	Right parietal grade 4 glioblastoma multiforme	Jaw 1	Descends through CR, IC, to CP
			Jaw 2	Descends through CR, IC, to CP
6	M / 49	Right front parietal grade 4 glioblastoma multiforme	Hand	Descends through CR, IC to CP
			Index Finger	Descends through CR, IC, to CP
			Forearm	Descends through CR, IC, to CP
7	M / 46	Left insular grade 4 glioblastoma	Mouth 1	Descends through CR, IC, to CP
			Mouth 2	Stimulation site proximal to tumor and edema and tracks diverted posteriorly
			Jaw	Stimulation site proximal to tumor and edema and tracks diverted posteriorly
8	F / 36	Left frontal grade 3 anaplastic astrocytoma	Mouth 1	Descends through CR, IC, to CP
			Mouth 2	Descends through CR, IC, to CP
9	M / 22	Left posterior frontal lobe grade 2 astrocytoma	Wrist	Descends through CR, IC, to CP
			Forearm	Descends through motor gyrus to SLF
			Shoulder	Descends through CR, IC, to CP
10	M / 65	Right posterior frontal lobe grade 3 anaplastic astrocytoma	Hand 1	Descends through motor gyrus to SLF
			Hand 2	Descends through motor gyrus to SLF
11	M / 38	Left grade 3 fronto-temporal anaplastic astrocytoma	Tongue 1	Descends through CR, IC, to CP
			Tongue 2	Descends through motor gyrus to CR

Table 6-1: Summary of cases and tracking results. Cases with two different cortical stimulation sites controlling similar motor responses are numbered. SLF: Superior longitudinal fasciculus, CR: Corona radiata, CP: Cerebral peduncle, IC: Internal capsule.

UNCLASSIFIED

Fiber tracks descending from the precentral gyrus through the corona radiata were organized somatotopically, mirroring the cortical motor homunculus. The corticospinal tract is known to twist as it descends through the corona radiata and internal capsule (12). In patient 9, this twisting was also observed in the DTI fiber tracks (Figure 6-3). The motor cortex representation for the shoulder is superiolateral to the wrist cortical representation. As the DTI fiber tracks enter the cerebral peduncle, the wrist and shoulder DTI tracks have switched positions, placing the wrist track medial to the shoulder track.

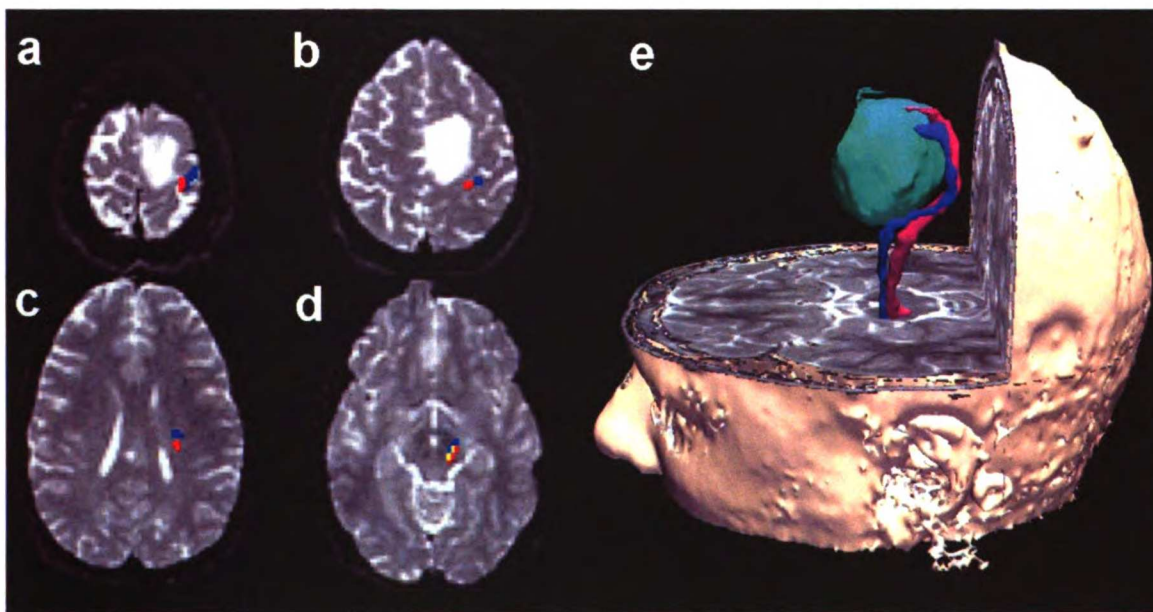


Figure 6-3: Subcortical organization of DTI fiber tracks. Fiber tracks from patient 9 are shown intersecting different axial levels. Tracks from shoulder motor (red) and wrist motor (blue) cortical stimulation sites are seen descending to the cerebral peduncle. Overlapping voxels are shown in yellow. A) Level of shoulder stimulation site. The wrist stimulation site was superior to the shoulder site. B) Motor tracks passing by border of tumor. The corticospinal tract is deviated posterolaterally by the mass of the tumor. C) Corticospinal tracts descending through the centrum semiovale. The DTI fiber tracks have spiraled, placing the shoulder track directly posterior to the wrist track. D) Shoulder track medial to wrist track in the cerebral peduncle. E) Three dimensional view of DTI fiber tracks in relation to tumor (green). The two tracks are seen twisting about each other as they descend through the internal capsule.

UNIVERSITY OF MICHIGAN LIBRARY

6.4.2 Fiber Tracking and Crossing Neuronal Fibers

In four of the DTI fiber tracks that did not connect the cortex with the internal capsule, the fiber tracks diverged along the superior longitudinal fasciculus (SLF). These fiber tracks originated at wrist, forearm, and two hand motor stimulation sites. The SLF courses anteroposteriorly through the centrum semiovale and intersects or passes very closely to portions of the pyramidal tract, particularly those axonal tracts from the upper extremity. Fiber tracks in these four cases were observed coursing from the cortex, through the precentral gyrus along the pyramidal tract, and into the centrum semiovale (Figure 6-4). However, instead of descending into the internal capsule, these four tracks entered the SLF and were diverted either anteriorly or posteriorly.

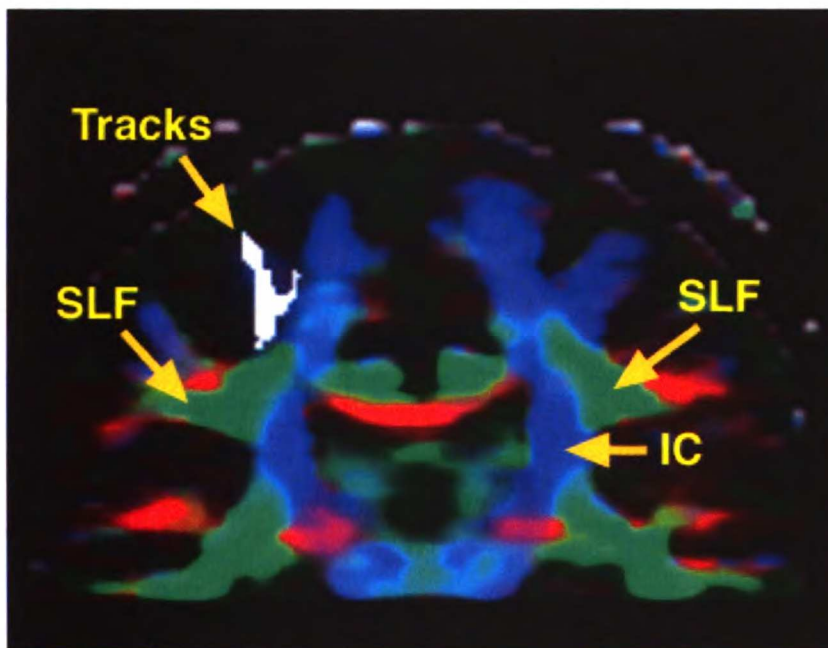


Figure 6-4: Fiber tracks encountering crossing fibers. Coronal slice through fiber tracks (white) terminating at the superior longitudinal fasciculus (SLF). Directionality of the primary eigenvector is color coded with anterior-posterior as green, left-right as red, and inferior-superior as blue. The anteroposteriorly directed fibers of the SLF are seen as green triangular regions (arrows) in both

the left and right hemispheres. The descending motor pathway tracks (hand #2, patient 10, depicted in white) intersects or passes very closely to the SLF, preventing DTI fiber tracks from entering the internal capsule (IC).

6.4.3 Fiber Tracking and Edema

Five of the fiber tracks that did not reach the internal capsule diverged and terminated in regions of peritumoral vasogenic edema exhibiting low anisotropic diffusion. Figure 6-5 shows a fiber track from a cortical site on patient 2 initiating wrist and finger flexion that enters a region of edema anterior to the tumor. Tumor and edema infiltration of the pyramidal tracts is evident from decreased anisotropy and hyperintensity of T2-weighted images. The fiber tracks initially descend through the precentral gyrus and corona radiata anterior to the tumor. As the fiber track proceeds through the regions of edema, the track fragments and courses posteriorly.

11/11/11 10:00

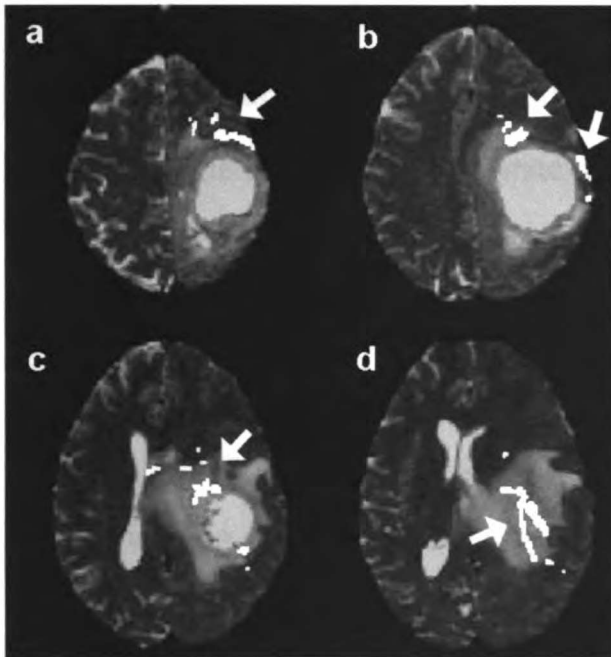


Figure 6-5: Fiber track divergence in edema. A) DTI fiber tracks from a wrist/finger motor site from patient 2 initially descend through the precentral gyrus. B) Fiber tracks are seen descending parallel to the border of the tumor and C) entering a hyperintense region of edema. D) The tracks are deviated posteriorly and are not consistent with the known location of the pyramidal tract at this level.

6.5 Discussion

DTI fiber tracks originated at the motor cortex stimulation sites and revealed the subcortical connectivity of the pyramidal tract. The rostral segment of the subcortical motor tract was delineated in all cases.

6.5.1 Delineation of a Functionally Specific White Matter Pathway

The results suggest that the DTI fiber tracks maintain some degree of functional specificity. The descending DTI fiber tracks were not observed to greatly diverge

www.lidiana.com

or encompass the entire pyramidal tract. The human motor cortex homunculus is topographically organized by function, as observed through cortical stimulation (15). The underlying subcortical white matter architecture is an extension of the organization of the cortex. The descending motor tracts form a converging sheet as they descend into the internal capsule. The organization of this sheet by function was observed with DTI fiber tracking. The motor tracts spiral as they descend from the cortex to the cerebral peduncle. In one case, fiber tracks from two stimulation points were observed to twist about each other in the corona radiata and internal capsule. The fiber tracks from the two stimulation points were consistent with the known structure and somatotopic organization of the motor functions associated with the cortical origins of the track (12).

Previous studies have used DTI anisotropy maps and directional color-coded images to determine the relationship of tumor to surrounding white matter (10, 19). Fiber tracking based on DTI can supplement these techniques by extending functional knowledge from the cortex to subcortical regions. Since a large tumor can distort the surrounding brain anatomy, it may be unclear which gyrus contains the descending motor pathway. By following white matter fasciculi from known motor points on the cortex, the position of the pyramidal tract at the level of the tumor can be elucidated. Even if it is not possible to follow the pyramidal tract completely to the midbrain, DTI fiber tracking may still be valuable in delineating the motor pathway near the borders of a tumor.

11/11/11 10:00

6.5.2 Limitations of the DTI Fiber Tracking Technique

DTI fiber tracks that entered regions of edema or tumor were prone to failure because of low anisotropy indicating uncertainty of the primary eigenvector direction. Edema increases the isotropic characteristic of diffusion and degrades the ability of DTI to detect white matter tracts. Thus, tracks entering regions of edema could be misdirected by eigenvectors not accurately representing the directionality of axonal bundles. Even though the fiber tracks sometimes terminated or diverged in regions of edema, it was demonstrated through motor stimulation that the pyramidal tract was functionally intact within these regions. Thus, in cases where DTI does not show neuronal pathways in a lesion, no immediate conclusion can be made about whether the tracts are destroyed or functionally intact.

The error in fiber tracking trajectories are known to accumulate as a function of distance, step size, algorithm, data signal-to-noise, track geometry, anisotropy and ambient white matter architecture (11, 14). Our results demonstrate a high degree of precision, which is partly due to tracking a convergent, high anisotropy pathway from the cortex to the mid-brain. Conversely, tracking from the mid-brain to the cortex would produce more errors in the final destination of the tracks. Therefore, cortical localization of functional regions enables association of function with structural connectivity and is optimum in terms of delineating fiber tracts that converge subcortically.

11/10/11 10:00

Four DTI fiber tracks from upper extremity motor sites were observed to deviate from the pyramidal tract when encountering fiber crossings. Portions of the pyramidal tract can intersect the superior longitudinal fasciculus at the level of the centrum semiovale. When white matter bundles intersect or pass very close to one another, the directionality of the primary eigenvector can be ambiguous and DTI fiber tracking can indicate false connectivity. Only fiber tracks from upper extremity motor sites were observed entering the SLF. The section of the motor cortex controlling upper extremities is superior and lateral to the SLF. The descending white matter pathways from this region of cortex curve inferiorly and medially through the corona radiata and can intersect the SLF. Motor skills of the hand and arm are important to preserve during resection, and this limitation caused by interference from the SLF must be considered when observing fiber tracks from these motor sites. To prevent tracks from being diverted from the pyramidal tract, the SLF can be segmented and DTI tracks terminated prior to encountering the SLF. Even though fiber tracking is halted, the pyramidal tract between the cortex and SLF can still be delineated and could be useful for surgical planning.

The dominant factors affecting the ability of DTI fiber tracking to follow the motor tract are crossing fibers and lesion location. Crossing fibers in the centrum semiovale are expected to complicate fiber tracking of upper extremity motor pathways in all patients. However, the location and geometry of lesions differs in each case. Factors such as preoperative functional deficit, tumor grade, and

11/10/11 10:00 AM

patient age were not observed to impact the ability to delineate motor pathways. Previous studies have shown that DTI fiber tracking is capable of delineating motor pathways in patients with congenital hemiparesis (8). It was found that motor pathways affected by hemiparesis exhibited lower anisotropy than the contralateral tracts, however fiber tracking was successful in both motor pathways.

6.5.3 Use of DTI Fiber Tracking for Surgical Planning

The technique described here in which fiber tracking begins at cortical stimulation sites may be implemented in the operating room (5, 9). Although, motor mapping by cortical stimulation is performed after the surgical procedure has begun, DTI fiber tracking could be completed in approximately 30 minutes, which is rapid enough to be of use during the subcortical resection. The necessary steps are to translate the motor points from the 3D volumetric MR images on the surgical navigation system images to the 3D DTI images, perform the DTI fiber tracking, and then overlay the tracked pathway back on the 3D volumetric images. A system performing these tasks in the operating room would enable the neurosurgeon to identify the subcortical position of specific motor functions in relation to the border of the resection cavity.

11/11/11 11:11:11

6.6 Conclusions

Identification of the position of the pyramidal tract relative to all borders of a tumor is critical for preserving motor function during surgery to remove the lesion. The combination of precise intraoperative cortical mapping information with DTI fiber tracking can reveal the course of motor pathways beneath the cortex. The subcortical fiber tracks generated are consistent with the known anatomical course and somatotopic organization of the pyramidal tract. Motor pathways displaced by the mass of the tumor were readily observed.

This study also showed some of the limitations of the DTI fiber tracking technique. The brain tumor and its surrounding vasogenic edema can alter the diffusion characteristics of functional white matter, interfering with the ability of DTI fiber tracking to fully delineate a white matter pathway. Crossing white matter fibers can also divert DTI fiber tracks from portions of the descending motor tract to another pathway such as the superior longitudinal fasciculus. Within these limitations, this new imaging technique allows functional cortical localization to be extended to the subcortical white matter pathways.

In this study, I have correlated DTI fiber tracking with functionally mapped cortical points. However, the clinical significance of DTI fiber tracking is primarily its ability to delineate specific white matter pathways within deep white matter structures. The results shown in this chapter are extended with the work I

11/11/11 10:00 AM

completed in Chapter 7. In Chapter 7, DTI fiber tracking is further validated with subcortical stimulations in the subcortical white matter.

6.7 References

1. Basser PJ, Mattiello J, LeBihan D: Estimation of the effective self-diffusion tensor from the NMR spin echo. **J Magn Reson B** 103:247-254, 1994.
2. Berger MS: Minimalism through intraoperative functional mapping. **Clin Neurosurg** 43:324-337, 1996.
3. Berger MS, Ojemann GA: *Intraoperative Monitoring Techniques in Neurosurgery*. New York, McGraw-Hill, 1994.
4. Berman JI, Berger MS, Mukherjee P, Henry RG: Diffusion-tensor imaging-guided tracking of fibers of the pyramidal tract combined with intraoperative cortical stimulation mapping in patients with gliomas. **J Neurosurg** 101:66-72, 2004.
5. Coenen VA, Krings T, Mayfrank L, Polin RS, Reinges MH, Thron A, Gilsbach JM: Three-dimensional visualization of the pyramidal tract in a neuronavigation system during brain tumor surgery: first experiences and technical note. **Neurosurgery** 49:86-92; discussion 92-83, 2001.
6. Conturo TE, Lori NF, Cull TS, Akbudak E, Snyder AZ, Shimony JS, McKinstry RC, Burton H, Raichle ME: Tracking neuronal fiber pathways in the living human brain. **Proc Natl Acad Sci U S A** 96:10422-10427, 1999.
7. Duffau H, Capelle L, Denvil D, Sichez N, Gatignol P, Taillandier L, Lopes M, Mitchell MC, Roche S, Muller JC, Bitar A, Sichez JP, van Effenterre R: Usefulness of intraoperative electrical subcortical mapping during surgery for low-grade gliomas located within eloquent brain regions: functional results in a consecutive series of 103 patients. **J Neurosurg** 98:764-778, 2003.
8. Glenn OA, Henry RG, Berman JI, Chang PC, Miller SP, Vigneron DB, Barkovich AJ: DTI-based three-dimensional tractography detects differences in the pyramidal tracts of infants and children with congenital hemiparesis. **Journal of Magnetic Resonance Imaging** 18:641-648, 2003.
9. Holodny AI, Schwartz TH, Ollenschleger M, Liu WC, Schulder M: Tumor involvement of the corticospinal tract: diffusion magnetic resonance tractography with intraoperative correlation. **J Neurosurg** 95:1082, 2001.
10. Krings T, Reinges MH, Thiex R, Gilsbach JM, Thron A: Functional and diffusion-weighted magnetic resonance images of space-occupying lesions affecting the motor system: imaging the motor cortex and pyramidal tracts. **J Neurosurg** 95:816-824, 2001.

11. Lazar M, Alexander AL: Divergence/Convergence Effects on the Accuracy of White Matter Tractography Algorithms. Presented at ISMRM, Toronto, 2003.
12. Martin JH: *Neuroanatomy : text and atlas*. Stamford, Conn., Appleton & Lange, 1996.
13. Mori S, Crain BJ, Chacko VP, van Zijl PC: Three-dimensional tracking of axonal projections in the brain by magnetic resonance imaging. **Ann Neurol** 45:265-269, 1999.
14. Mori S, van Zijl PC: Fiber tracking: principles and strategies - a technical review. **NMR Biomed** 15:468-480, 2002.
15. Penfield W, Rasmussen T: *The cerebral cortex of man : a clinical study of localization of function*. New York, Macmillan, 1950.
16. Roux FE, Ibarrola D, Tremoulet M, Lazorthes Y, Henry P, Sol JC, Berry I: Methodological and technical issues for integrating functional magnetic resonance imaging data in a neuronavigational system. **Neurosurgery** 49:1145-1156; discussion 1156-1147, 2001.
17. Schiffbauer H, Berger MS, Ferrari P, Freudenstein D, Rowley HA, Roberts TP: Preoperative magnetic source imaging for brain tumor surgery: a quantitative comparison with intraoperative sensory and motor mapping. **J Neurosurg** 97:1333-1342, 2002.
18. Schiffbauer H, Ferrari P, Rowley HA, Berger MS, Roberts TP: Functional activity within brain tumors: a magnetic source imaging study. **Neurosurgery** 49:1313-1320; discussion 1320-1311, 2001.
19. Witwer BP, Moftakhar R, Hasan KM, Deshmukh P, Haughton V, Field A, Arfanakis K, Noyes J, Moritz CH, Meyerand ME, Rowley HA, Alexander AL, Badie B: Diffusion-tensor imaging of white matter tracts in patients with cerebral neoplasm. **J Neurosurg** 97:568-575, 2002.
20. Yingling CD, Ojemann S, Dodson B, Harrington MJ, Berger MS: Identification of motor pathways during tumor surgery facilitated by multichannel electromyographic recording. **J Neurosurg** 91:922-927, 1999.

1. The first part of the document discusses the importance of maintaining accurate records of all transactions and activities. It emphasizes that this is crucial for ensuring transparency and accountability in the organization's operations.

2. The second part of the document outlines the specific procedures and protocols that must be followed to ensure the integrity and security of the data.

3. The third part of the document provides a detailed overview of the various systems and tools used to manage and analyze the data, highlighting their strengths and limitations.

Chapter 7: Accuracy of Diffusion Tensor MRI Tractography Assessed with Subcortical Intraoperative Stimulation

7.1 Abstract

The study presented in Chapter 6 showed the correlation of DTI fiber tracks with cortical stimulation sites. However, the placement of DTI motor fiber tracks within the deep white matter of the human brain has not previously been validated. In this study, I used intraoperative subcortical stimulation of the motor tract to validate DTI fiber tracking's utility as a tool for surgical planning.

DTI fiber tracks were generated preoperatively using regions drawn based on anatomical landmarks. A mask of the resultant fiber tracks were overlaid on high resolution T1 and T2-weighted anatomical images and used for stereotactic surgical navigation. During surgical resection, subcortical stimulation of the motor pathway was performed within white matter using a bipolar stimulator. A total of 16 subcortical motor stimulations were stereotactically identified on 9 patients. The mean distance between the stimulation sites and the DTI fiber tracks was 8.7 ± 3.2 mm. The observed gap between the stimulation sites and DTI fiber tracks is expected because of electrical current penetration depth during bipolar stimulation. The precision of the DTI fiber tracking technique is affected by brain shift, stereotactic registration error, and DTI fiber tracking error.

This study shows the validity of using DTI fiber tracking of the the motor tract with a surgical navigation system.

7.2 Introduction

During resection of cerebral tumors, preservation of the patient's motor function is a priority. Knowledge of the location of the pyramidal tract in relation to a tumor is important for deciding if surgery is feasible and for maintaining a margin of safety between the resection cavity and functional pathways. If the descending motor pathway is damaged during brain surgery, the patient is likely to experience post-operative motor deficits. Brain mapping techniques such as magnetic source imaging (MSI), functional MR, transcranial stimulation, and direct electrical cortical stimulations are capable of identifying motor and somatosensory cortices (2, 6, 24, 27, 28). However, these procedures are restricted to the grey matter and cannot reveal the subcortical position of the pyramidal tract. Subcortical stimulation can be performed during tumor resection to identify the motor tract in deep white matter structures, however the technique is time consuming, invasive, and does not reveal the full extent of the motor tract (3, 14). This study evaluates the accuracy and validity of a preoperative, non-invasive diffusion tensor MRI fiber tracking method to localize the motor tract in subcortical white matter.

Delineating white matter pathways for neurosurgical planning is one of the most obvious and challenging applications of DTI fiber tracking (5, 9, 11).

Conventional T1 and T2-weighted anatomical images used for stereotactic navigation show little or no contrast between white matter structures. In tumor cases with mass effect or edema, it may be difficult to find structures such as the internal capsule on traditional MR images. Color maps indicating the direction of the primary eigenvector provide some additional information about white matter structures. However, the pyramidal tract is within a band of parallel pathways in the internal capsule and corona radiata. Thus, the motor tract cannot be differentiated with primary eigenvector maps from sensory, frontopontine, and other parallel pathways. However, when information from DTI fiber tracking is integrated with conventional images, specific white matter pathways can be visualized.

In prior studies, DTI fiber tracking has been shown to connect functionally mapped motor cortex with the midbrain (5, 9). Other validity studies have been limited to animal models and phantoms (16, 17). However, the accuracy of DTI fiber tracks between the cortex and the midbrain in humans has not been shown. Subcortical stimulation is the clinical gold standard and only functional method for identifying the pyramidal tract in deep white matter structures (14). Thus, before DTI fiber tracking can be relied upon as an accurate surgical planning tool, the technique must be validated with subcortical stimulations. In this study, I generated DTI fiber tracks of the pyramidal tract preoperatively and integrated the data with a surgical navigation system. The DTI fiber tracks were then

compared with the location of subcortical motor stimulations to evaluate the validity and accuracy of fiber tracking.

7.3 Methods

7.3.1 Imaging

MR scans of 9 adult patients were performed one day prior to craniotomy for resection of cerebral gliomas. Consecutive patients undergoing intraoperative motor mapping with subcortical stimulation were analyzed. The patients consisted of 5 men and 4 women with a mean age of 41 years and a mix of tumor grades (Table 7-1). MR images were acquired on a 1.5T scanner (General Electric, Milwaukee WI). DTI was performed with $b=1000\text{s/mm}^2$, $\text{TR/TE} = 10000/100\text{ms}$, slice thickness between 2 and 3 mm, no inter-slice gap, voxel volume between 4.8 and 10.1 mm^3 , and 6 averaged acquisitions. Six diffusion gradient directions and one image set without diffusion weighting ($b=0\text{ s/mm}^2$) were acquired. Acquisition coverage was from the cerebral peduncle to the brain vertex. The diffusion tensor, eigenvectors, eigenvalues, and relative anisotropy were calculated using in-house software. T2-weighted and post-contrast T1-weighted anatomical images were also acquired for use with the stereotactic surgical navigation system. T2-weighted images were acquired with an axial fast spin echo (FSE) pulse sequence with $\text{TR/TE} = 3\text{s}/105\text{ms}$, field of view $260 \times 195\text{mm}$, 256×192 matrix, and voxel dimensions of $1.02 \times 1.02 \times 1.5\text{mm}$ with no gap between slices. T1-weighted images were acquired with a spoiled gradient

echo (SPGR) sequence with TR/TE = 34ms/3ms, field of view 260 x 195mm, 256 x 192 matrix, and voxel dimensions of 1.02 x 1.02 x 1.5mm with no gap between slices. FSE and SPGR acquisition coverage included the entire head and 10 fiducials attached to the head. Magnetic source imaging (MSI) was performed on 7 of the patients to identify somatosensory and motor cortical sites. Functional cortex was localized from the early peak response after mechanical stimulation of digits, lips, and toes and a hand movement task.

Subject	Age/ Gender	Tumor/Grade	Presurgical Motor Deficit	Postsurgical Motor Deficit
1	35/F	Oligodendoglioma, Grade II	None	None
2	33/F	Oligodendoglioma, Grade II	None	None
3	58/M	Glioblastoma, Grade IV	Very mild hand motor deficit	No change
4	31/M	Oligoastrocytoma, Grade III	None	Facial weakness after face motor cortex removed
5	49/M	Glioblastoma, Grade IV	Decreased hand dexterity	No change
6	48/F	Oligodendroglioma, Grade II	Upper extremity and Facial weakness	Facial droop after face motor cortex removed; Decreased fine motor hand skills
7	45/M	Astrocytoma, Grade II	None	None
8	50/F	Astrocytoma, Grade III	None	None
9	22/M	Astrocytoma, Grade II	None	Minor decreased movement on right side

Table 7-1: Summary of patients included in study.

7.3.2 DTI Fiber Tracking

DTI fiber tracking of the pyramidal tract was performed with an algorithm based on the fiber assignment by continuous tracking (FACT) method (19). DTI fiber tracking software was written in Interactive Data Language (Research Systems

Inc., Boulder CO) and run on a SunBlade 2500 workstation (Sun Microsystems, Santa Clara CA). Fiber tracks were launched from a region drawn in the cerebral peduncle ipsilateral to the brain tumor (Figure 7-1a). Fiber trajectories follow the primary eigenvector in 3D through the brain. Target regions were drawn in the posterior limb of the internal capsule and the precentral gyrus (Figure 7-1a).

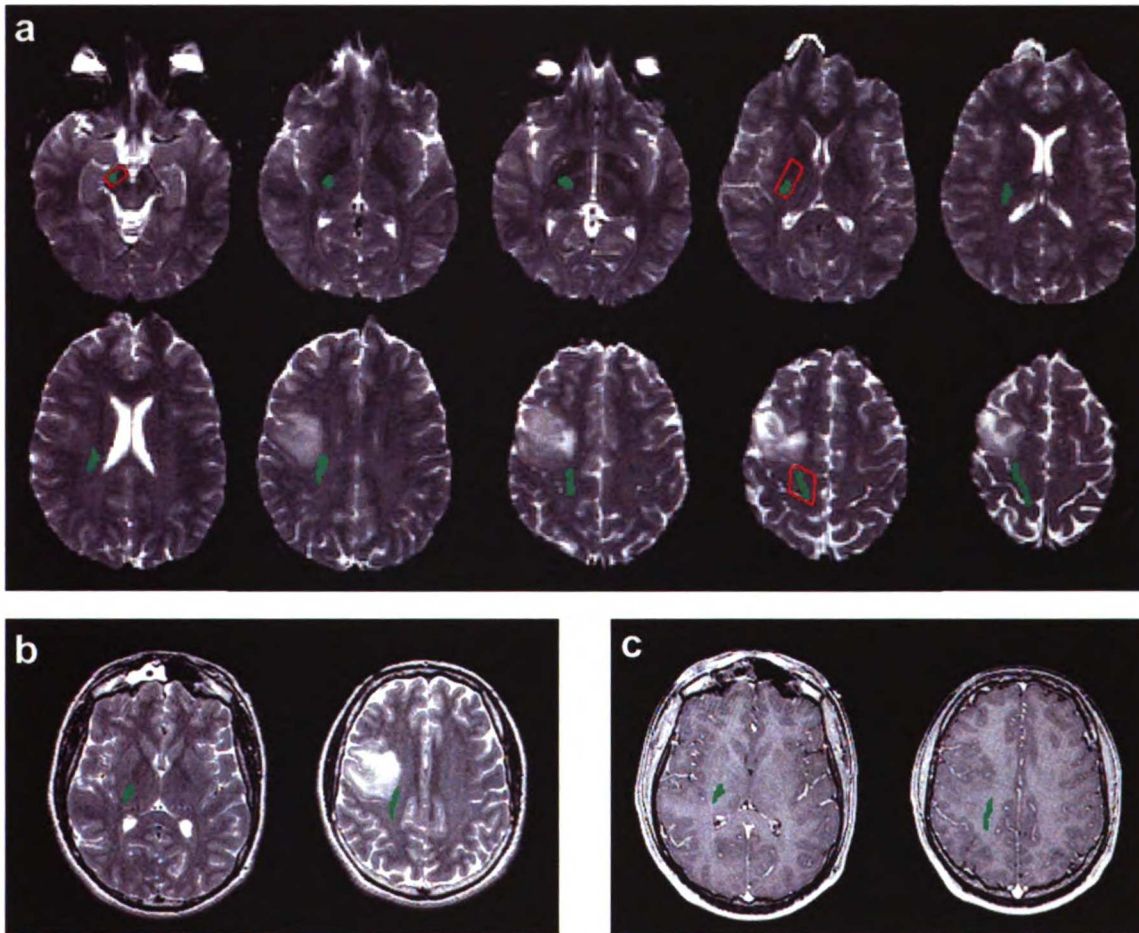


Figure 7-1: a) DTI fiber tracks of the pyramidal tract are shown at different levels of the $b=0$ echo planar images. Voxels through which the fiber tracks pass are colored green. The starting region for tracking (red outline) is seen at the level of the cerebral peduncle. Additional regions drawn in the posterior limb of the internal capsule and the precentral gyrus (red outline) are also shown. Generated fiber tracks are seen to course through the internal capsule and near the posterior-medial border of the lesion. b) DTI fiber tracks shown registered

and overlaid on FSE images at the level of the internal capsule and at the lesion.
c) DTI fiber tracks registered and overlaid on SPGR images.

DTI Fiber tracks passing through each of the three drawn regions were retained as pyramidal fiber tracks. The DTI $b=0$ echo planar volume was registered to the FSE and SPGR image volumes with a 3D affine 12-parameter model fit with a maximum of 50 iterations (31). The resulting transformation was then used to overlay a mask of the fiber tracks onto the anatomical FSE and SPGR images. Pixels containing fiber tracks were assigned intensities higher than any anatomical feature in the image. This bright white intensity ensures fiber tracks could be distinguished from T2-lesions, contrast enhancement, and CSF. The anatomical images with overlaid fiber tracks were loaded onto the stereotactic surgical navigation system for use during resection (StealthStation, Medtronic, Broomfield, CO). The surgical navigation system's software was used to register the T1 and T2-weighted anatomical images to each other and to the patient's head in the operating room. The total time required between the completion of the MR exam and uploading the images to the surgical navigation system was approximately 2 hours. In one patient, DTI fiber tracking was performed after the surgery but with the presurgical DTI data by a user blinded to the results of the subcortical stimulation.

7.3.3 Subcortical Stimulation

Direct electrical stimulation of subcortical white matter within the resection cavity was performed during the surgical procedure with a 5mm wide bipolar electrode

(4). Points that elicited a motor response were stereotactically identified on the anatomical images and screen saves from the navigation system were saved. Typically, a specific muscle group's movement was observed such as finger motion or mouth motion. Once a subcortical motor site was found, resection at that location is stopped. After the surgery, I download the screensaves from the navigation system for analysis. The distance between the stimulation site and the closest in-plane border of the DTI fiber tracks was measured.

7.4 Results

7.4.1 DTI Fiber Tracking

The pyramidal tract was successfully delineated with DTI fiber tracking in each of the 9 patients in this study. Figure 7-1 shows an example result with the DTI fiber tracks coursing from the cerebral peduncle, through the internal capsule, to the precentral gyrus. During the surgery, the neurosurgeon could clearly visualize the motor tract in 3D or on any plane through the cerebrum. In no case did the white voxels representing the DTI fiber tracks interfere with interpretation of the T1 or T2-weighted anatomical images.

A total of 16 subcortical motor stimulation points were identified of which 8 were face or mouth motor, 4 were upper extremity motor, and 4 were lower extremity motor sites. All stimulation sites were either on the lesion border or within the lesion. In all cases, the DTI fiber tracks were outside the resection cavity. The

average distance between stimulation sites and DTI fiber tracks was 8.7 ± 3.2 mm. Figure 7-2 shows an example subcortical stimulation of arm motor and the measured distance to the DTI fiber tracks. In Figure 7-3, the measured distances are grouped into lower extremity, upper extremity, and head motor responses. There was no significant difference between measured distances among the three motor stimulation groups ($P=0.95$, ANOVA).

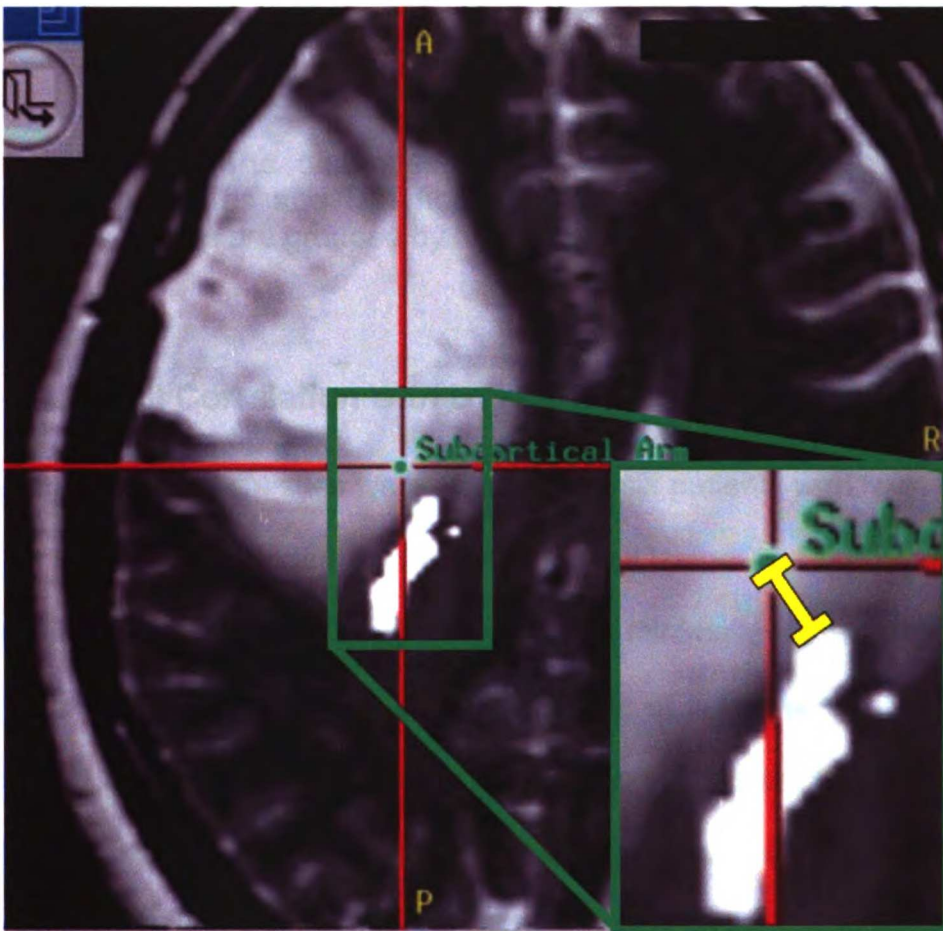


Figure 7-2: The crosshairs indicate the locations of an arm motor subcortical stimulation site on this screen save from the surgical navigation system. In the close-up view, the yellow bar shows the distance between the stereotactically identified stimulation site and the DTI fiber tracks.

www.nwll.com

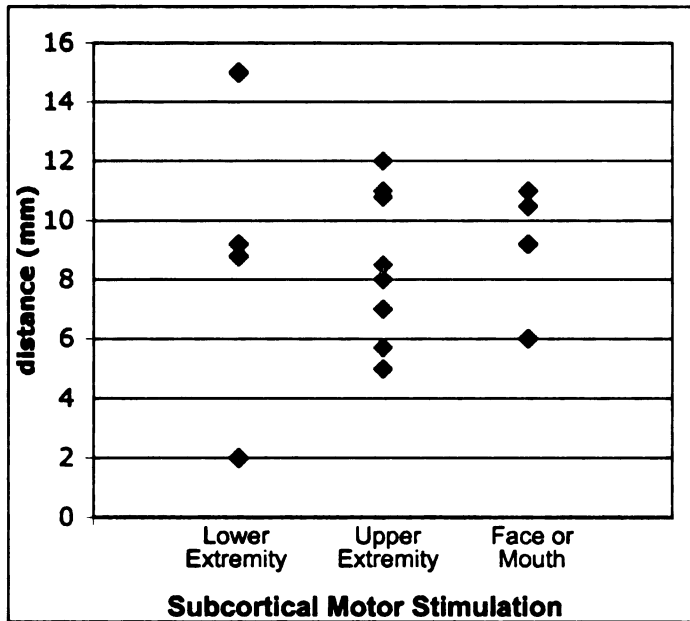


Figure 7-3: The distances between stereotactically localized subcortical stimulation sites and DTI fiber tracks of the motor tract are shown. The measurements are grouped by region of the body.

7.4.2 MSI Correlation with DTI Fiber Tracks

Functional cortical sites were identified on six patients with MSI. In one patient, no MSI sites were identified ipsilateral to the lesion. In four of these patients, the position of the precentral gyrus was not or minimally altered by mass effect from lesion. Figure 7-4 shows the juxtaposition of subcortical motor sites, DTI fiber tracks, and MSI somatosensory sites in one such case. The DTI fiber tracks and motor stimulations are within the precentral gyrus and the MSI somatosensory sites are within the postcentral gyrus. In two patients with MSI and subcortical stimulation data, the lesion compressed the precentral and postcentral gyri. Figure 7-5 shows one such case where the DTI fiber tracks, subcortical

stimulation, MSI motor site, and MSI sensory site are all aligned along the posterior margin of the tumor.

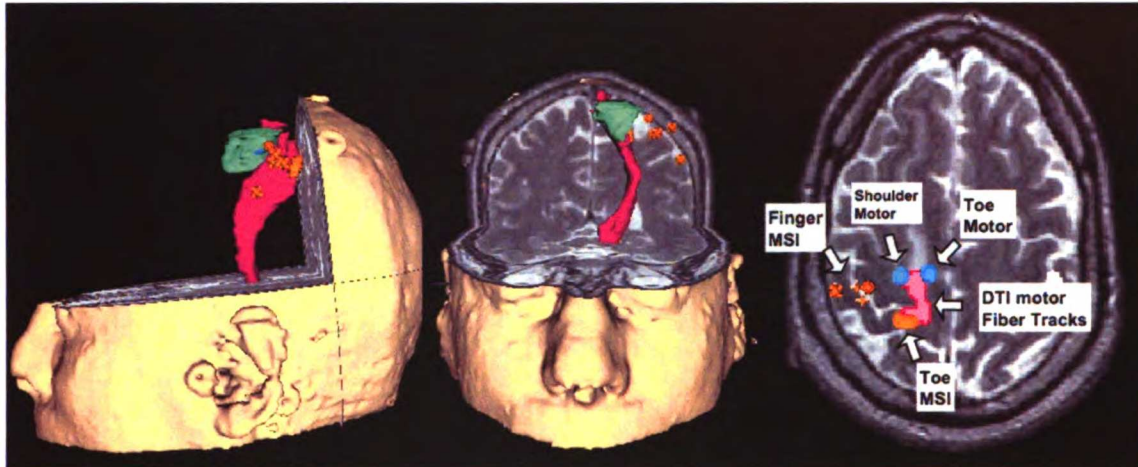


Figure 7-4: Illustrative case showing the juxtaposition of subcortical motor sites (blue), DTI fiber tracks (red), and MSI somatosensory sites (gold). The axial section (right) includes MSI sites and subcortical stimulations within 1 cm of the axial level projected onto the image. The DTI fiber tracks and motor stimulations are within the precentral gyrus and the MSI somatosensory sites are within the postcentral gyrus. The DTI fiber tracks adjacent to the toe motor stimulation site show connectivity to the superior-medial portion of the motor cortex, which is known to control lower extremity motor.

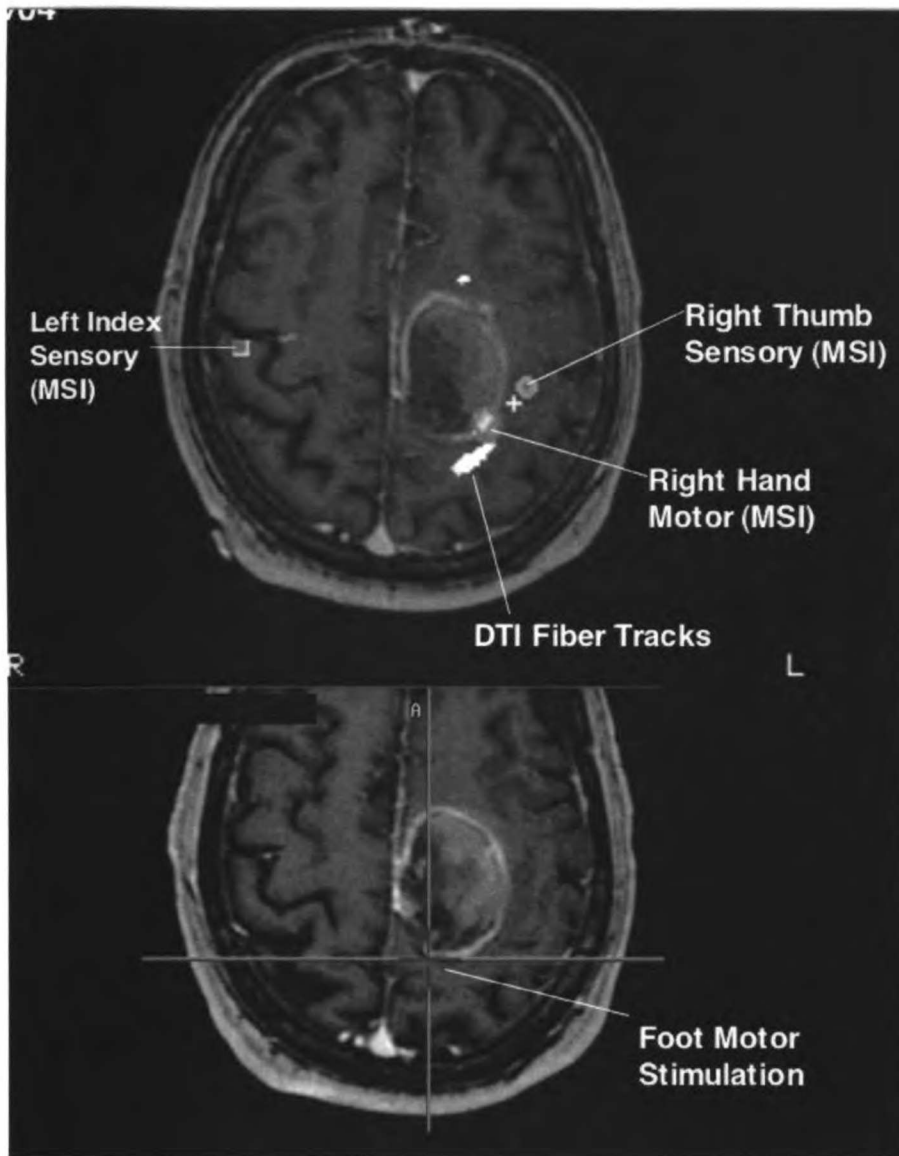


Figure 7-5: Illustrative case showing the compression of the motor and sensory tracts along the posterior border of the lesion. MSI thumb sensory (orange), MSI hand motor (purple), DTI fiber tracks (bright white), and a foot motor stimulation site (bottom, crosshairs) are shown.

7.5 Discussion

DTI fiber tracking provides information on white matter connectivity and can be used to segment the motor tract in 3D. In this study, DTI fiber tracks were

1945
1946
1947
1948
1949
1950
1951
1952
1953
1954
1955
1956
1957
1958
1959
1960
1961
1962
1963
1964
1965
1966
1967
1968
1969
1970
1971
1972
1973
1974
1975
1976
1977
1978
1979
1980
1981
1982
1983
1984
1985
1986
1987
1988
1989
1990
1991
1992
1993
1994
1995
1996
1997
1998
1999
2000
2001
2002
2003
2004
2005
2006
2007
2008
2009
2010
2011
2012
2013
2014
2015
2016
2017
2018
2019
2020
2021
2022
2023
2024
2025

1945
1946
1947
1948
1949
1950
1951
1952
1953
1954
1955
1956
1957
1958
1959
1960
1961
1962
1963
1964
1965
1966
1967
1968
1969
1970
1971
1972
1973
1974
1975
1976
1977
1978
1979
1980
1981
1982
1983
1984
1985
1986
1987
1988
1989
1990
1991
1992
1993
1994
1995
1996
1997
1998
1999
2000
2001
2002
2003
2004
2005
2006
2007
2008
2009
2010
2011
2012
2013
2014
2015
2016
2017
2018
2019
2020
2021
2022
2023
2024
2025

integrated with anatomical images for visualization during stereotactic tumor resection. The fiber tracking technique was validated in deep white matter structures with subcortical stimulation. The correlation with subcortical stimulations suggests that DTI fiber tracking can be a valuable tool for surgical planning.

In this study, anatomical images fused with bright white overlays of the DTI fiber tracks were loaded onto the surgical navigation system. This black and white fused image approach is easy to implement and requires no additional time to load or set up on the surgical navigation system. In no case did the overlaid DTI fiber tracks interfere with interpretation of the underlying anatomical images. If pathways besides the motor tract such as sensory or language are requested for surgical use, the black and white fused image approach may not be able to clearly distinguish the multiple pathways. Transparent color overlays of each pathway may be a better approach in this situation.

Electrical current from the bipolar stimulator penetrates tissue surrounding the electrodes, stimulating a volume of tissue. However, the surgical navigation system only identifies a single point associated the position of the electrodes. The range of bipolar stimulation has been observed to be up to 8 mm (8, 23). Models have also predicted that current density falls with the square of distance within brain tissue (21). Since resection is halted when a motor subcortical stimulation is found, a gap between the stimulation point and the motor tract is

expected. In this study, an offset between DTI fiber tracks and stimulation sites was observed which is consistent with the current penetration expected.

Stereotactic localization error and brain shift each contribute to errors in the stereotactic navigation system. A number of studies have examined the inherent technical errors in optical stereotactic localization (7, 13, 15). The localization error of a frameless optical system with high resolution MRI, as used in this study, is typically less than 1.5 mm. Studies have shown brain shift to be highly variable (7, 20, 22, 25, 26). Brain shift can be inward or outward and is related to many factors including lesion size, gravity, and surgical technique. A recent study used DTI fiber tracking to determine a mean outward 2.7 mm shift of white matter pathways (22). A systematic outward brain shift due to decompression will artifactually increase the measured distance between stimulation sites and DTI fiber tracks. Brain shift and other inherent localization errors contribute to variability in the perceived distance between subcortical stimulation and DTI fiber tracks.

Noise, echo planar distortions, and limitations of the tensor model in regions of crossing fibers contribute to errors in the orientation of the primary eigenvector (1, 12, 16, 18, 29). If the primary eigenvector does not accurately reflect the orientation of axonal bundles, DTI fiber tracking may provide erroneous results. Extraneous fiber tracks outside the motor tract may be produced or the full extent of the motor tract may not be delineated. The three ROI approach used in this

study is expected to constrain the number of extraneous fiber tracks. Regions of crossing fibers in the centrum cerniovale prevent DTI fiber tracking from reproducibly delineating the entire motor pathway. Prior studies have shown that crossing white matter pathways hinder detection of connectivity to the section of the motor cortex controlling upper extremity motor (5). Future fiber tracking work using high angular resolution diffusion imaging may improve the performance of fiber tracking (29, 30).

It is difficult to separate DTI fiber tracking error from other stereotactic navigation errors and stimulation effects. Figure 7-6 shows an example where DTI fiber tracking error can be eliminated as a factor contributing to the gap between subcortical stimulation and fiber tracks. The motor tract is known to not pass through the temporal lobe, however a motor stimulation site was localized within a temporal lesion. Thus, the 8.5 mm gap between the cerebral peduncle and the stimulation site in this case can be attributed to current penetration, stereotactic errors, and brain shift.

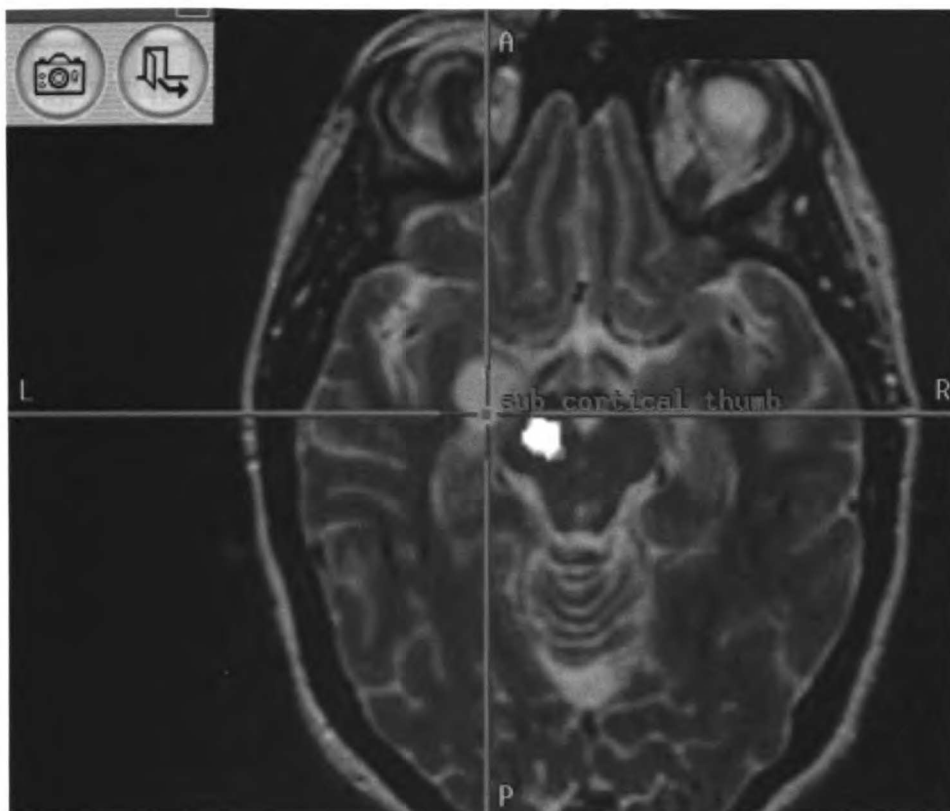


Figure 7-6: A subcortical thumb motor stimulation site (cross hairs) is shown localized to the temporal lobe. The DTI fiber tracks of the motor pathways are shown (bright white) within the cerebral peduncle. The apparent distance between the stimulation site and the cerebral peduncle is expected because of the penetration of stimulation current. In addition, brain shift and stereotactic registration errors can also contribute to variability in stimulation site localization.

This study provides a clinically relevant analysis of the validity of DTI fiber tracking when used in conjunction with a surgical navigation system. The measured distance between subcortical stimulation and DTI fiber tracks is a combination of all factors encountered when combining DTI fiber tracking with a stereotactic navigation system. The mean distance of 8.7 mm provides a clinically useful guide to the motor tract's location. The 3.2 mm standard deviation of the measured distance is consistent with the known precision of stereotactic localization during resections.

1
2
3
4
5
6
7
8
9
10
11
12
13
14
15
16
17
18
19
20
21
22
23
24
25
26
27
28
29
30
31
32
33
34
35
36
37
38
39
40
41
42
43
44
45
46
47
48
49
50
51
52
53
54
55
56
57
58
59
60
61
62
63
64
65
66
67
68
69
70
71
72
73
74
75
76
77
78
79
80
81
82
83
84
85
86
87
88
89
90
91
92
93
94
95
96
97
98
99
100

1
2
3
4
5
6
7
8
9
10
11
12
13
14
15
16
17
18
19
20
21
22
23
24
25
26
27
28
29
30
31
32
33
34
35
36
37
38
39
40
41
42
43
44
45
46
47
48
49
50
51
52
53
54
55
56
57
58
59
60
61
62
63
64
65
66
67
68
69
70
71
72
73
74
75
76
77
78
79
80
81
82
83
84
85
86
87
88
89
90
91
92
93
94
95
96
97
98
99
100



Prior DTI fiber tracking validation studies have not addressed the location of fiber tracks between the cortex and midbrain in humans (5, 10). Functional mapping techniques can validate the cortical endpoint of DTI fiber tracks, but provide no information on the location of the connecting white matter. In this study, the MSI cortical sites indicated that the DTI fiber tracks were correctly located in the precentral gyrus. However, the MSI could not validate the placement of the motor tract within the internal capsule or centrum semiovale.

Intraoperative cortical and subcortical stimulation will remain the gold standard for functional localization. However, DTI fiber tracking can be a valuable complement to invasive subcortical stimulation. DTI is non-invasive and increases MRI scan time by only a moderate amount. In this study, the DTI data was acquired in approximately 15 minutes. DTI fiber tracking requires significant post-processing resources, however the process can easily be accomplished in the time between MRI and surgery. Unlike subcortical stimulation, DTI fiber tracking can provide information on the 3D extent of the motor tract prior to surgery. Subcortical stimulation can locate points along the motor tract only when the resection has encroached within a small distance of the functional pathway. Prior studies have shown that the incidence of postoperative motor deficit is higher when subcortical stimulation sites are found (14). When no subcortical stimulation sites are found, the resection cavity is presumably a greater distance from functional motor tracts. DTI fiber tracks can indicate which

borders of the lesion should not be aggressively resected to avoid being within stimulation range of the motor tract. Alternatively, surgical planning based on DTI fiber tracking in combination with subcortical stimulation may have the potential to prevent surgical morbidity. DTI fiber tracks can indicate which regions of brain should be more carefully mapped with subcortical stimulation to avoid surgical morbidity after aggressive resection.

7.6 Conclusion

In both this chapter and Chapter 6, I have shown the clinical validity of DTI fiber tracking for surgical planning. To successfully complete this chapter's study, I developed a robust method of processing DTI fiber tracks and providing the results for intraoperative use. In Chapter 8, I provide a detailed description of the presurgical DTI fiber tracking protocol that I have introduced into routine clinical practice at our medical center.

7.7 References

1. Anderson AW: Theoretical analysis of the effects of noise on diffusion tensor imaging. **Magn Reson Med** 46:1174-1188, 2001.
2. Berger MS: Minimalism through intraoperative functional mapping. **Clin Neurosurg** 43:324-337, 1996.
3. Berger MS, Ojemann GA: Intraoperative brain mapping techniques in neuro-oncology. **Stereotact Funct Neurosurg** 58:153-161, 1992.
4. Berger MS, Ojemann GA: *Intraoperative Monitoring Techniques in Neurosurgery*. New York, McGraw-Hill, 1994.
5. Berman JI, Berger MS, Mukherjee P, Henry RG: Diffusion-tensor imaging-guided tracking of fibers of the pyramidal tract combined with intraoperative cortical stimulation mapping in patients with gliomas. **J Neurosurg** 101:66-72, 2004.

6. Ganslandt O, Buchfelder M, Hastreiter P, Grummich R, Fahlbusch R, Nimsky C: Magnetic source imaging supports clinical decision making in glioma patients. **Clinical Neurology and Neurosurgery** 107:20-26, 2004.
7. Grunert P, Darabi K, Espinosa J, Filippi R: Computer-aided navigation in neurosurgery. **Neurosurg Rev** 26:73-99; discussion 100-101, 2003.
8. Haglund MM, Ojemann GA, Blasdel GG: Optical imaging of bipolar cortical stimulation. **J Neurosurg** 78:785-793, 1993.
9. Hendler T, Pianka P, Sigal M, Kafri M, Ben-Bashat D, Constantini S, Graif M, Fried I, Assaf Y: Delineating gray and white matter involvement in brain lesions: three-dimensional alignment of functional magnetic resonance and diffusion-tensor imaging. **J Neurosurg** 99:1018-1027, 2003.
10. Henry RG, Berman JI, Nagarajan SS, Mukherjee P, Berger MS: Subcortical pathways serving cortical language sites: initial experience with diffusion tensor imaging fiber tracking combined with intraoperative language mapping. **Neuroimage** 21:616-622, 2004.
11. Holodny AI, Schwartz TH, Ollenschleger M, Liu WC, Schulder M: Tumor involvement of the corticospinal tract: diffusion magnetic resonance tractography with intraoperative correlation. **J Neurosurg** 95:1082, 2001.
12. Jones DK: Determining and visualizing uncertainty in estimates of fiber orientation from diffusion tensor MRI. **Magn Reson Med** 49:7-12, 2003.
13. Kaus M, Steinmeier R, Sporer T, Ganslandt O, Fahlbusch R: Technical accuracy of a neuronavigation system measured with a high-precision mechanical micromanipulator. **Neurosurgery** 41:1431-1436; discussion 1436-1437, 1997.
14. Keles GE, Lundin DA, Lamborn KR, Chang EF, Ojemann G, Berger MS: Intraoperative subcortical stimulation mapping for hemispherical peritumoral gliomas located within or adjacent to the descending motor pathways: evaluation of morbidity and assessment of functional outcome in 294 patients. **J Neurosurg** 100:369-375, 2004.
15. Krempien R, Hassfeld S, Kozak J, Tuemmler HP, Dauber S, Treiber M, Debus J, Harms W: Frameless image guidance improves accuracy in three-dimensional interstitial brachytherapy needle placement. **Int J Radiat Oncol Biol Phys** 60:1645-1651, 2004.
16. Lazar M, Alexander AL: An error analysis of white matter tractography methods: synthetic diffusion tensor field simulations. **Neuroimage** 20:1140-1153, 2003.
17. Lin CP, Tseng WY, Cheng HC, Chen JH: Validation of diffusion tensor magnetic resonance axonal fiber imaging with registered manganese-enhanced optic tracts. **Neuroimage** 14:1035-1047, 2001.
18. Lori NF, Akbudak E, Shimony JS, Cull TS, Snyder AZ, Guillory RK, Conturo TE: Diffusion tensor fiber tracking of human brain connectivity: acquisition methods, reliability analysis and biological results. **NMR Biomed** 15:494-515, 2002.
19. Mori S, Crain BJ, Chacko VP, van Zijl PC: Three-dimensional tracking of axonal projections in the brain by magnetic resonance imaging. **Ann Neurol** 45:265-269, 1999.

20. Nabavi A, Black PM, Gering DT, Westin CF, Mehta V, Pergolizzi RS, Jr., Ferrant M, Warfield SK, Hata N, Schwartz RB, Wells WM, 3rd, Kikinis R, Jolesz FA: Serial intraoperative magnetic resonance imaging of brain shift. **Neurosurgery** 48:787-797; discussion 797-788, 2001.
21. Nathan SS, Sinha SR, Gordon B, Lesser RP, Thakor NV: Determination of current density distributions generated by electrical stimulation of the human cerebral cortex. **Electroencephalogr Clin Neurophysiol** 86:183-192, 1993.
22. Nimsky C, Ganslandt O, Hastreiter P, Wang RP, Benner T, Sorensen AG, Fahlbusch R: Preoperative and intraoperative diffusion tensor imaging-based fiber tracking in glioma surgery. **Neurosurgery** 56:130-137, 2005.
23. Ojemann G: Brain organization for language from the perspective of electrical stimulation mapping. **The Behavioral and Brain Sciences** 6:189-230, 1983.
24. Penfield W, Rasmussen T: *The cerebral cortex of man : a clinical study of localization of function*. New York, Macmillan, 1950.
25. Reinges MHT, Nguyen HH, Krings T, Hutter BO, Rohde V, Gilsbach JM: Course of brain shift during microsurgical resection of supratentorial cerebral lesions: limits of conventional neuronavigation. **Acta Neurochirurgica** 146:369-377, 2004.
26. Roberts DW, Hartov A, Kennedy FE, Miga MI, Paulsen KD: Intraoperative brain shift and deformation: a quantitative analysis of cortical displacement in 28 cases. **Neurosurgery** 43:749-758; discussion 758-760, 1998.
27. Roux FE, Ibarrola D, Tremoulet M, Lazorthes Y, Henry P, Sol JC, Berry I: Methodological and technical issues for integrating functional magnetic resonance imaging data in a neuronavigational system. **Neurosurgery** 49:1145-1156; discussion 1156-1147, 2001.
28. Schiffbauer H, Berger MS, Ferrari P, Freudenstein D, Rowley HA, Roberts TP: Preoperative magnetic source imaging for brain tumor surgery: a quantitative comparison with intraoperative sensory and motor mapping. **J Neurosurg** 97:1333-1342, 2002.
29. Tuch DS: Q-ball imaging. **Magn Reson Med** 52:1358-1372, 2004.
30. Tuch DS, Reese TG, Wiegell MR, Wedeen VJ: Diffusion MRI of complex neural architecture. **Neuron** 40:885-895, 2003.
31. Woods RP, Grafton ST, Holmes CJ, Cherry SR, Mazziotta JC: Automated image registration: I. General methods and intrasubject, intramodality validation. **Journal of Computer Assisted Tomography** 22:139-152, 1998.

Chapter 8: Presurgical DTI Fiber Tracking Protocol

8.1 Motivation

The previous chapters have shown the validity of DTI fiber tracking for identifying the motor tract in brain tumor patients. Delineating white matter pathways for neurosurgical planning is one of the most obvious and challenging applications of DTI fiber tracking (3, 4). Translating DTI fiber tracking into a useful clinical tool requires robust integration of the technique into presurgical protocols. Besides technical considerations, there are many safety issues involved with modifying images to be used during brain surgery. This chapter describes the presurgical DTI fiber tracking protocol I have developed and routinely perform at UCSF. The protocol involves image acquisition, post processing, quality assurance, and communication with the neurosurgical staff. To date, the protocol outlined in this chapter has been used with approximately 100 brain tumor cases. DTI is ordered as a supplementary tool for any cases involving awake or asleep intraoperative cortical stimulation mapping.

8.2 Introduction

T2-weighted FSE and T1-weighted SPGR anatomical images are the primary volumes used for surgical planning and intraoperative stereotactic navigation. These images have high resolution and the post-contrast SPGR volumes can show contrast enhancement within tumors. However, these traditional

anatomical images show little or no contrast between different white matter structures. Thus, DTI fiber tracking with echo planar diffusion images is performed to delineate specific white matter pathways. The echo planar images have coarse resolution and suffer from spatial distortions, making the echo planar images unsuitable for surgical navigation. Standard high-resolution anatomical images and DTI fiber tracks must be fused together so that the information from both data sets may be viewed simultaneously. The solution is to overlay fiber tracks on the anatomical images for stereotactic navigation. This chapter presents the constraints on the DTI fiber tracking protocol and the solutions I have developed.

8.3 Constraints

The following sections describe the mandatory features of the presurgical DTI fiber tracking protocol. These requirements are necessary to ensure the technique is robust and safe.

8.3.1 Timing

Time is of the essence when DTI fiber tracks are generated for use in the operating room. Patients are generally scanned the day before their surgery. Depending on when the scan is scheduled, the MR exam can be completed as late as 8 or 9 PM. Brain surgeries at UCSF typically begin at 7:30 AM, but the surgical navigation system needs to be set up and configured at about 6 AM.

This sequence of events leaves less than 10 hours for processing the DTI maps, constructing the DTI fiber tracks, relaying the images to the operating room, and troubleshooting any unexpected problems. Thus a streamlined, robust, and consistent system is necessary for placing DTI fiber tracks on the surgical navigation system and transmitting the results to the picture archival communication system (PACS).

8.3.2 Interference of Overlaid Fiber Tracks with Underlying Anatomy

DTI fiber tracks are most useful for surgical planning when the corticospinal tract courses adjacent to the lesion slated for resection. DTI fiber tracks placed directly on the border of the lesion can prevent visual demarcation of the lesion border. In addition, DTI fiber tracks adjacent to a hyperintense lesion can falsely make the lesion appear larger. The neurosurgeon must be able to clearly see the borders of the lesion in order to determine the extent of resection. Limiting the volume occupied by the DTI fiber tracks to the tract of interest and ensuring contrast between the lesion and overlaid fiber tracks may meet these constraints.

8.3.3 Registration of MR Volumes

Accurate registration of echo planar DTI volumes to the high-resolution surgical navigation images is required. The echo planar DTI volume is characterized by warping of the brain because of susceptibility differences at the air-tissue interfaces. A non-linear algorithm capable of aligning the echo planar images to

the anatomical images is necessary for accurately overlaying the DTI fiber tracks to anatomical images.

8.3.4 Image Accuracy and Quality Assurance

The image files generated by the presurgical DTI protocol will be relied upon by the neurosurgeon during a patient's brain surgery. Thus, the software used for the presurgical DTI protocol must accurately preserve the image information and identifiers not related to the DTI fiber tracks. Within the image, the anatomical contrast must not be changed. The images must never be flipped in any direction. The Digital Imaging and Communication in Medicine (DICOM) header information must also be preserved to ensure accurate interpretation of the image files by PACS and the surgical navigation system. For example, the coordinate system must not be altered, the number of slices must remain the same, and the patient name must be correct. Any inadvertent changes to the MR images caused by the DTI fiber tracking protocol can have serious clinical ramifications. The presurgical DTI protocol was thus designed to have multiple quality assurance steps.

8.4 Technique Methods

I developed the presurgical protocol described in the following section to address the various safety and technical considerations encountered and anticipated.

8.4.1 Medical Center Image Network

The systems level procedure for bringing DTI fiber tracking into the operating room is shown in Figure 8-1. The medical center network allows images to be received and transmitted quickly and efficiently. The nodes include scanners, Unix workstations, and PACS workstations. All computers are connected via a medical center wide network which enables DICOM images to be shared. The universal DICOM format allows any scanner at UCSF to be utilized. The picture archival and communication system (PACS) is a central database which collects images from the scanners and can send or receive patient scans to other systems within the medical center. Other laboratories, such as the Biomagnetic Imaging Laboratory, have access to PACS and can overlay functional information in addition to the DTI fiber tracks overlaid by our laboratory.

In a situation where the medical center network is not operating, images can be manually transferred to and from nodes on the network with compact disks.

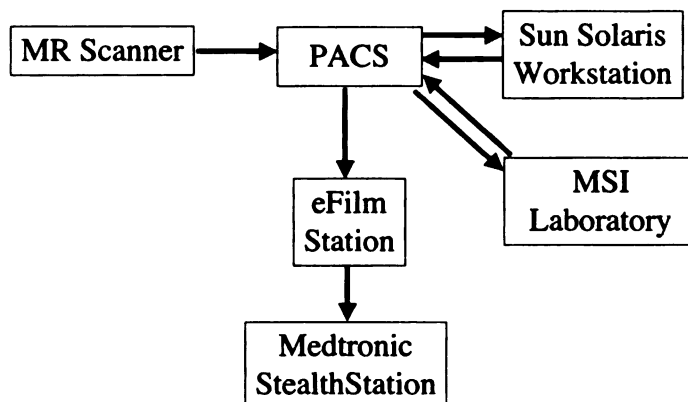


Figure 8-1: DTI and anatomical images are acquired on the MR scanner and archived on PACS. Images on PACS are retrieved for processing and the images for use in the operating room are transmitted back to PACS. Staff in the

operating room are able to retrieve the surgical navigation images from PACS and place them first on the eFilm station and then the StealthStation surgical navigation system.

8.4.2 DTI Processing and Fiber Tracking

DTI processing is performed on the Sun Solaris workstations in our laboratory. The specific tasks and timings for generating DTI fiber tracks are listed in Figure 8-2. The minimum time required for processing, after completion of the MR exam, is approximately 1.5 hours.

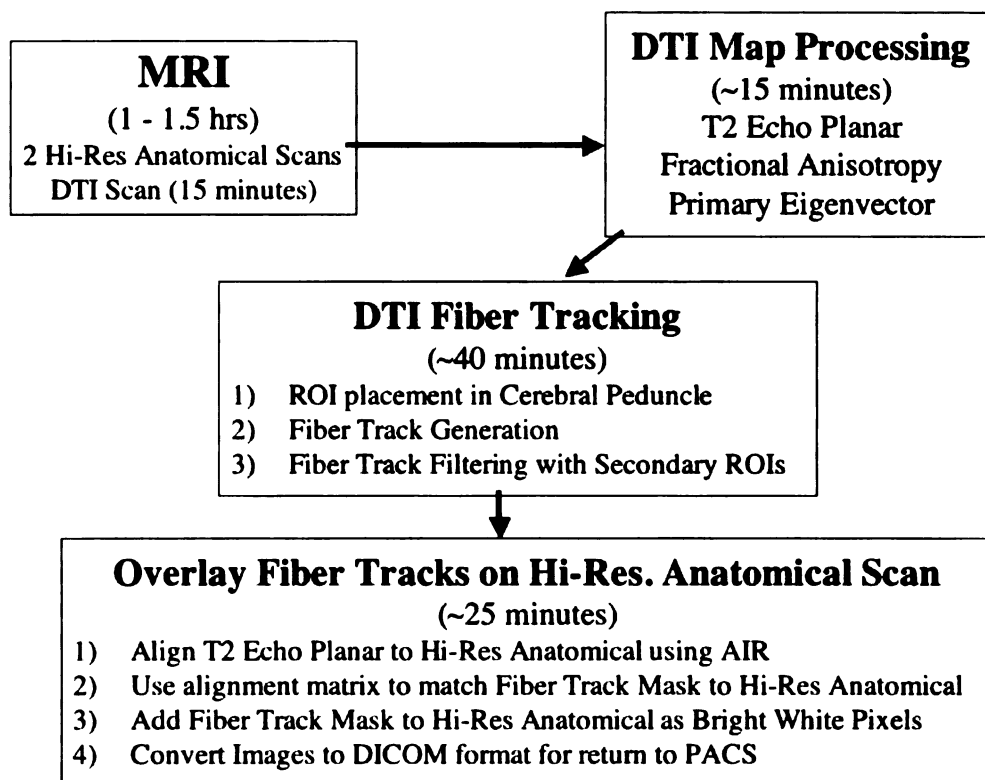


Figure 8-2: Timing of tasks required for constructing DTI fiber tracks and overlaying the tracks on anatomical images used for surgical navigation.

The raw diffusion weighted images are processed to create the eigenvector and anisotropy maps using previously developed in-house software based on published algorithms (1, 2). The DTI maps are output in our laboratory's in-house image format developed by others. This in-house image format is very similar to the analyze format. All fiber tracking and image fusion is performed with the in-house format. DTI processing for a 6 gradient direction data set typically takes less than 15 minutes on a Sun Blade workstation.

Fiber tracking is performed with a multiple ROI process using the tools I have developed and previously described (Figure 8-3). Fiber tracks are first generated from a region drawn in the cerebral peduncle with the aid of the $b=0$ echo planar image and the anisotropy map (Figure 8-3A & B). The resultant fiber tracks are then targeted to a region drawn in the posterior limb of the internal capsule (Figure 8-3C). Then a third targeting region is drawn around fiber track bundles anterior to the central sulcus within the precentral gyrus (Figure 8-3D). Fiber tracks passing through all three regions are retained as the delineated pyramidal tract. Resulting fiber tracks of the motor tract are shown in Figure 8-4.

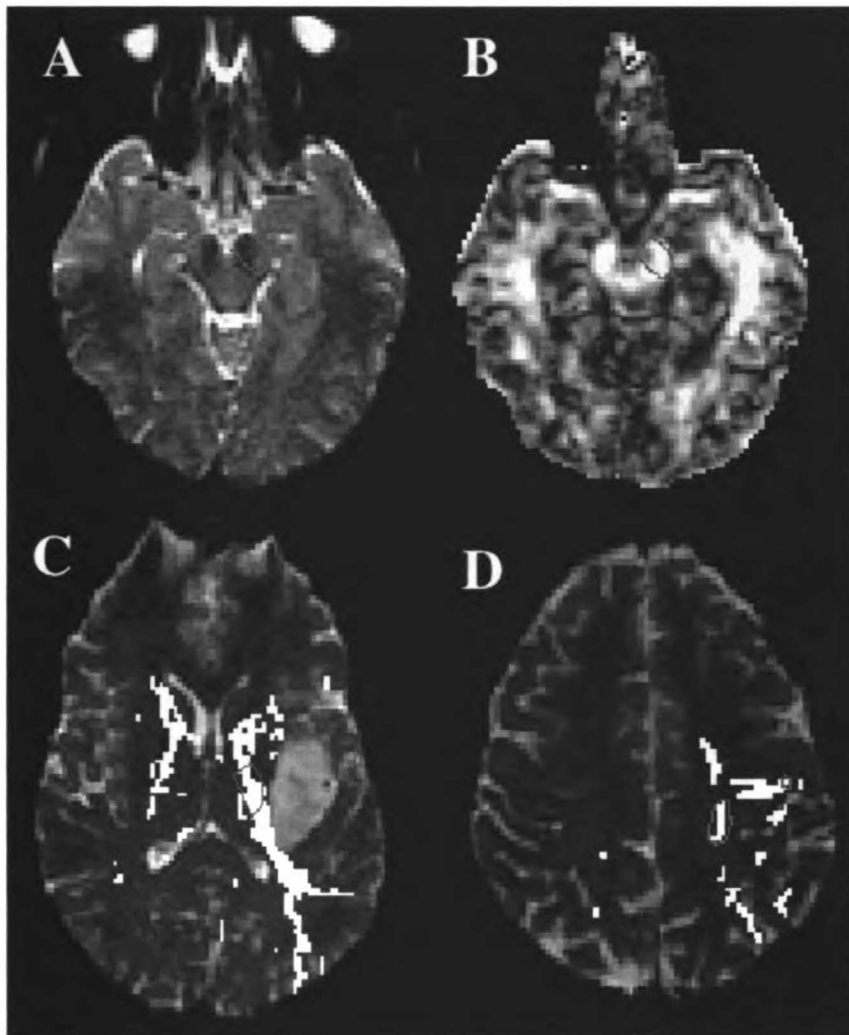


Figure 8-3: A) The DTI fiber tracking starting ROI is shown in green. The starting region is drawn in the cerebral peduncle. B) Anisotropy map with starting ROI shown in green. C) Fiber tracks originating from the cerebral peduncle are shown in bright white. The fiber tracks are targeted to a region drawn in the posterior limb of the internal capsule. D) An additional target region is drawn anterior to the central sulcus.

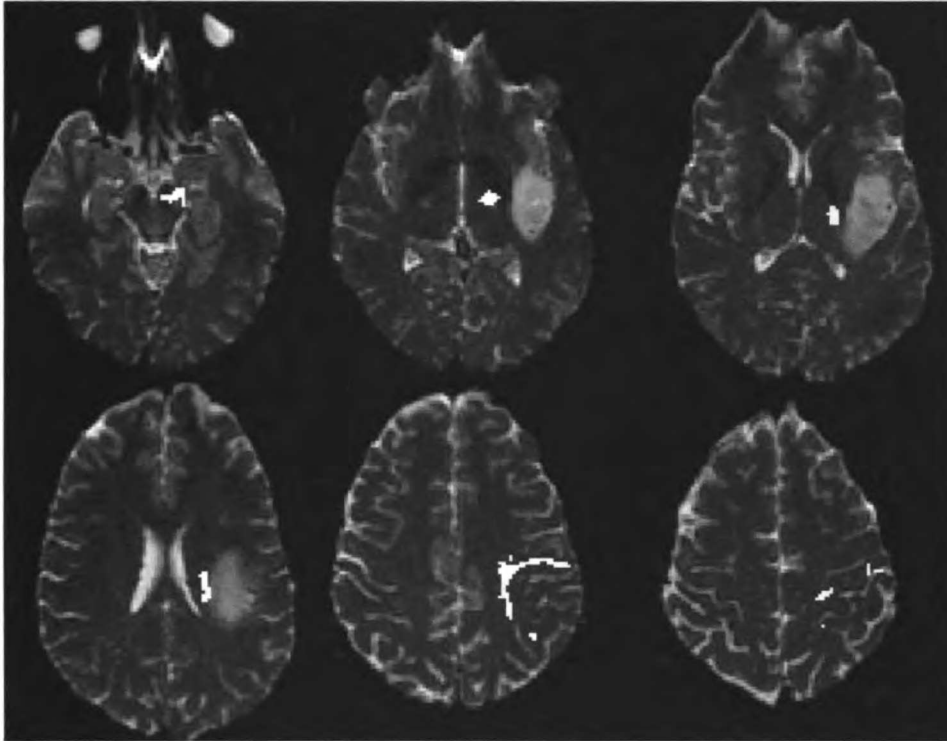


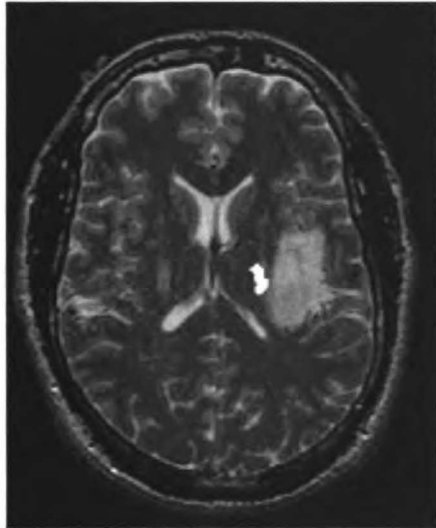
Figure 8-4: Presurgical DTI fiber tracks of the corticospinal tract are shown. Fiber tracks are overlaid on b=0 echo planar images.

The tracks are initially overlaid on the b=0 echo planar images for inspection. As seen in Figure 8-4, the delineated pathway begins in the cerebral peduncle and maintains a singular, compact structure through the internal capsule. The fiber tracks begin to diverge in the corona radiata and a segment turns laterally into the motor cortex. A segment also continues superiorly to the vertex of the brain but maintains its position anterior to the central sulcus.

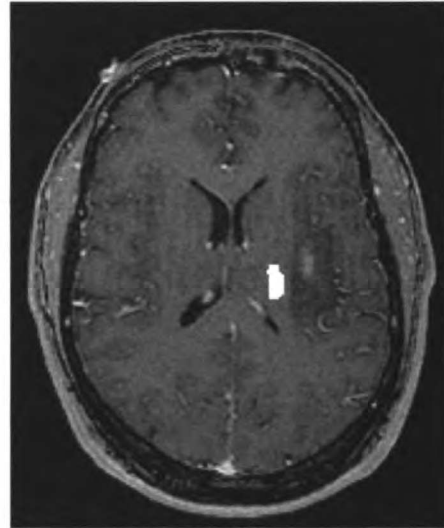
8.4.3 Fusion of Anatomical Images and DTI Fiber Tracks

Since the echo planar images are unsuitable for surgical navigation, the DTI fiber tracks must be fused with the high-resolution anatomical images. The b=0 echo

planar images are first aligned to the anatomical images using AIR (5, 6). A 3D affine 12 parameter model with a maximum of 50 iterations were used for registration. The registration's performance is checked by comparing the position of sulci, ventricles, and the brain's border. The transformation matrix is applied to the DTI fiber track mask and the registered mask fused to the anatomical images. Pixels containing fiber tracks are given intensities between 1.5 and 3 times higher than the brightest anatomical feature in the image (Figure 8-5). This "hot white" intensity ensures fiber tracks can easily be distinguished from T2-lesions and cerebral spinal fluid (CSF). The DTI fiber tracks also have a distinctive 3D geometric shape that can be visually recognized as separate from the underlying conventional MR image.



FSE



SPGR

Figure 8-5: DTI fiber tracks of the motor tract overlaid on images used for stereotactic navigation during craniotomy for tumor resection. The fiber tracks in bright white are easily spotted.

8.4.4 Transmission of Images to PACS

Once the fused images are created, the images must be converted into the DICOM format before being transmitted back to the PACS system. A copy of the original anatomical DICOM images is used as a template for the newly created image series. The changes to these original DICOM images are few. Of course, the entire image volume is swapped with the fused image volume. Within the header, the series descriptor is changed. Instead of "FSE" or "SPGR" the series descriptor is changed to "FSE Tractography Stealth" or "SPGR Tractography Stealth." The series number is also changed in the DICOM header to avoid confusion with the original series. Usually, the original series number is incremented by 10. Thus, the "FSE" series may be number 6 while the "FSE Tractography Stealth" series is assigned number 16. The unique identifier (UID) is a pseudo-random series of numbers which serves as a type of serial number for every image stored in the PACS system. The UID codes are changed to a new, unique number to avoid overwriting the original images in the PACS system.

Before the newly created DICOM images are transmitted to PACS, they are compared against the original anatomical images to ensure that the slices are in the correct order and the coordinate systems are identical. Once the images are transmitted to PACS, the images are once again checked on a PACS workstation. The original anatomical images are placed next to the fused images

and compared to ensure the patient name, coordinates, and slice order are identical.

After all checks are complete, the operating room staff and the neurosurgeons are notified that the DTI processing is complete. The operating room staff then retrieves the images from PACS and loads them on the surgical navigation system (Figure 8-6 and Figure 8-7).



Figure 8-6: Stereotactic navigation system components include camera (left), computer (right), screen, and probe (not shown).

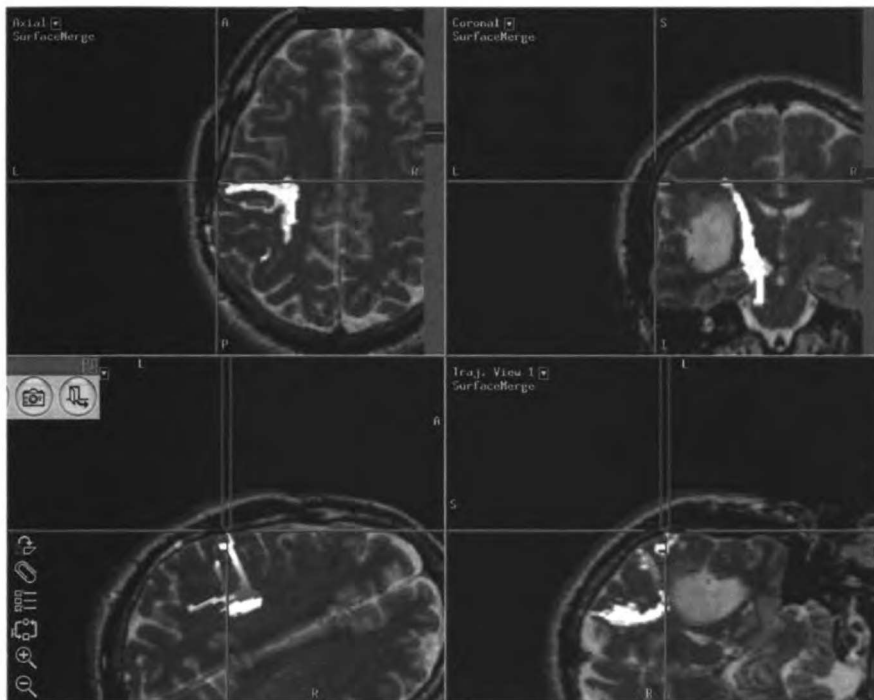


Figure 8-7: Screen capture from the surgical navigation system. The crosshairs indicate the location of a jaw motor site. Bright white pixels on the MR images indicate the DTI fiber tracks generated prior to surgery. Images are oriented in the neurological convention.

If the images do not pass all the quality checks, and the problem cannot be fixed, the images can not be used for surgical navigation. In cases where the fiber tracking was successful but image fusion was unsuccessful, we still have the option of allowing the neurosurgeon to view the DTI fiber tracks overlaid on the $b=0$ echo planar images. These images may be helpful, however they cannot be used in conjunction with the surgical navigation system due to their low resolution and spatial distortions.

8.5 Use of DTI in the OR

Since routine MR provides no contrast between different white matter pathways, DTI provides an important landmark for surgical planning (Figure 8-7). DTI fiber tracks can clearly show the location of the motor tract in 3D within the cerebrum. DTI fiber tracks of the motor pathway can also indirectly provide localization of the somatosensory pathway and cortex since the somatosensory radiation is situated directly posterior to the pyramidal tract.

Intraoperative cortical and subcortical stimulation remains the gold standard for functional localization. However, stimulation mapping can be time consuming and is not always possible because of bleeding or dura stuck to the cortex. DTI fiber tracking can add an additional margin of safety by guiding the stimulation mapping to the motor tract.

8.6 References

1. Basser PJ, Mattiello J, LeBihan D: Estimation of the effective self-diffusion tensor from the NMR spin echo. **J Magn Reson B** 103:247-254, 1994.
2. Basser PJ, Pierpaoli C: A simplified method to measure the diffusion tensor from seven MR images. **Magn Reson Med** 39:928-934, 1998.
3. Holodny AI, Schwartz TH, Ollenschleger M, Liu WC, Schulder M: Tumor involvement of the corticospinal tract: diffusion magnetic resonance tractography with intraoperative correlation. **J Neurosurg** 95:1082, 2001.
4. Krings T, Coenen VA, Axer H, Reinges MH, Holler M, von Keyserlingk DG, Gilsbach JM, Thron A: In vivo 3D visualization of normal pyramidal tracts in human subjects using diffusion weighted magnetic resonance imaging and a neuronavigation system. **Neurosci Lett** 307:192-196, 2001.
5. Woods RP, Grafton ST, Holmes CJ, Cherry SR, Mazziotta JC: Automated image registration: I. General methods and intrasubject, intramodality

- validation. **Journal of Computer Assisted Tomography** 22:139-152, 1998.
6. Woods RP, Grafton ST, Watson JDG, Sicotte NL, Mazziotta JC: Automated image registration: II. Intersubject validation of linear and nonlinear models. **Journal of Computer Assisted Tomography** 22:153-165, 1998.

Chapter 9: Quantitative DTI Fiber Tracking of the Preterm Infant's Sensorimotor Tracts

9.1 Abstract

In this chapter, the DTI techniques developed and validated in prior chapters are applied to a quantitative investigation of sensorimotor pathways in premature infants (8). Previous studies have only been able to delineate parts of these pathways that could be manually outlined in 2D based on anatomical landmarks. Furthermore, these previous studies could not separate motor and sensory regions.

For this patient study, I performed DTI fiber tracking to delineate the motor and sensory tracts and derive tract-specific measurements. A high-sensitivity neonatal head coil was employed in conjunction with an MR-compatible incubator to perform high-resolution imaging of the premature infant brain. The motor and somatosensory tracts were successfully delineated with 3D DTI fiber tracking in 37 exams of preterm newborns between 28 and 43 weeks gestational age. I implemented both streamline deterministic and probabilistic methods to perform quantitative fiber tractography. Tract-specific measurements of diffusion parameters including fractional anisotropy, directionally averaged diffusivity, and eigenvalues were obtained from the motor and sensory pathways. Using both deterministic and probabilistic fiber tracking, all tract-specific diffusion parameters were found to be significantly correlated with age and the motor tract was found

to have higher anisotropy and lower diffusivity than the sensory pathway. By segmenting the 3D fiber tracks by slice, measurements from different axial levels of the brain were found to vary with region and age.

9.2 Introduction

The premature infant brain undergoes rapid structural and functional development. Diffusion tensor MR imaging (DTI) is the first and only non-invasive technique capable of delineating white matter pathways in-vivo and quantifying microstructural changes not visible on conventional MR (34). DTI uses the diffusion of water as a probe to examine the brain's microstructural environment (3). The Brownian diffusion of water is hindered by axonal membranes, myelin, neurofilaments, and any other structures that interact with water molecules (6). Changes in the arrangement, quantity, and permeability of these diffusion barriers occur during brain maturation and injury. In pediatrics, DTI has found applications in detecting white matter changes in congenitally hemiplegic patients (12), white matter injury of prematurity (16, 18, 23), and white matter development (17, 26, 27).

Diffusion parameters describing the brain's microstructure include the three eigenvalues ($\lambda_1, \lambda_2, \lambda_3$), directionally averaged diffusion coefficient (D_{av}), and fractional anisotropy (FA). The primary eigenvalue is the magnitude of diffusivity in the direction of the primary eigenvector. In regions dominated by highly ordered axonal bundles, the primary eigenvector describes diffusivity parallel to

axonal bundles while the second and third eigenvectors describe diffusivity orthogonal to the axonal bundles. D_{av} is the mean of the three eigenvalues and describes the spatially-averaged diffusivity of water in a voxel. FA measures the degree of directionality of diffusion within a voxel. Even in the unmyelinated axonal bundles found in premature infants, diffusion is anisotropic due to higher restriction transverse to axons.

White matter fiber tracking with DTI is a non-invasive method of delineating functionally specific neuronal pathways in three dimensions (4, 9, 13, 25). Fiber tracking uses each voxel's primary eigenvector of the diffusion tensor to follow an axonal tract in 3D from voxel to voxel through the human brain. The clinical and scientific utility of DTI fiber tracking is found in both the localization and quantitative assessment of specific neuronal pathways. Localization of particular fiber tracts with DTI has proven useful in cases of periventricular leukomalacia (16). Besides qualitative localization, DTI fiber tracking also allows individual neuronal pathways to be quantified across regions of the brain where manual segmentation would not be possible. Quantitative assessment with fiber tracking has been shown to reveal microstructural changes in the corticospinal tracts of children with congenital hemiplegia that correlated with their motor impairment (12).

This study investigates the feasibility of both localizing and quantitatively assessing motor and sensory pathways during development in prematurely born

infants. The pyramidal tract and the somatosensory radiation are unmyelinated or partially myelinated in premature infants and are among the first white matter tracts to mature. During preterm maturation, these two important white matter tracts are susceptible to injury leading to neurological deficits, often resulting in the classic clinical presentation of spastic diplegia. Early detection and classification of neonatal brain injury may enable intervention and improve our ability to determine the neurodevelopmental prognosis of affected infants. Thus, there is great interest in improved non-invasive imaging techniques to monitor the structural development of these pathways. Unlike conventional T1- and T2-weighted MR imaging, DTI fiber tracking allows quantitative measurements along the entire 3D volume of a functionally specific axonal pathway, even prior to the onset of myelination.

9.3 Methods

9.3.1 Patient Population

Twenty-seven prematurely born infants were imaged between 28 and 43 weeks gestational age (GA), in accordance with a research protocol approved by the institutional review board at our medical center. Ten of the infants were serially scanned at two time points for a total of 37 MR scans. All of the infants included in this study had minimal or no white matter injuries on conventional spin echo T1 and T2-weighted images, using the grading system described by Miller et al. (24). Assessment for white matter injury was performed by consensus of two

neuroradiologists experienced in neonatal imaging. Cases with minimal white matter injury had 3 or fewer lesions measuring less than 2mm. Exclusion criteria included severe intraventricular hemorrhage, ventriculomegaly, and motion-degraded DTI.

9.3.2 Imaging

MR scans were performed at 1.5 Tesla on a General Electric Signa Echospeed LX scanner (General Electric, Milwaukee WI) using an MR-compatible incubator with a custom designed high sensitivity neonatal head coil (11). The incubator was built onto a scanner table and includes MR-compatible oxygen and air tanks along with monitors for blood pressure, oxygen saturation, respiration, and electrocardiography. T1-weighted volumes used for identifying lesions were coronal 3D spoiled gradient-echo images with 0.7 x 0.7 mm in-plane pixel size, 1.8 mm slice thickness, and TR/TE= 35/9 ms. DTI was acquired with a 4.8 minute single-shot, multirepetition echoplanar sequence with TR/TE = 7s/100ms, 256 x 128 matrix, 360x180 mm FOV, 167 kHz readout bandwidth, and 3 image averages. Voxel dimensions were 1.4 x 1.4 mm in-plane with 3 mm slice thickness and no slice gap. Diffusion gradients were applied in 6 non-collinear directions with $b=600 \text{ s/mm}^2$ in addition to a $b=0 \text{ s/mm}^2$ image. Acquisition coverage of the DTI volume was from the midbrain to the brain vertex.

Signal to noise ratios (SNR) of the echo planar images with and without diffusion weighting are summarized in Table 9-1. In two representative neonates, SNR

measurements were calculated for each of the six $b=600$ diffusion-weighted images independently and then averaged. The noise's standard deviation was estimated with a region drawn in the background outside the head. The SNR was multiplied by a factor of 0.655 to account for the background noise following a Rayleigh distribution (14).

		Frontal WM	Basal Ganglia	Internal Capsule
28 weeks GA	b=0	94.3	90.9	89.4
	b=600	37.6	40.5	43.8
40 weeks GA	b=0	76.0	66.1	65.2
	b=600	34.5	34.2	35.7

Table 9-1: Signal to noise ratios (SNR) for echo planar $b=0$ and $b=600$ s/mm^2 images in two neonates representative of the younger and older premature newborns.

Diffusion weighted images were motion corrected using the $b=0$ s/mm^2 echo planar image as a reference with a 2D 10th order nonlinear registration model (35, 36). The diffusion tensor and diffusion parameter maps were calculated for each voxel using in-house software written in C++ based on published algorithms (5). A smoothed and unsmoothed set of diffusion parameters including eigenvalues ($\lambda_1, \lambda_2, \lambda_3$), eigenvectors, fractional anisotropy, and D_{av} were then calculated for each patient. Smoothing was performed by averaging a 3×3 in-plane neighborhood of voxels on the echo planar images prior to tensor calculation. The smoothed diffusion parameter images were used for region of interest (ROI) placement and fiber tracking. To reduce partial-volume averaging of voxels included in tract quantification, the unsmoothed sets were used for

measurements of D_{av} , FA, and eigenvalues. Transverse diffusion represents diffusivity perpendicular to axonal bundles and is the mean of λ_2 and λ_3 . T1-weighted anatomical images were used for 3D rendering of the entire head in combination with the DTI fiber tracks.

9.3.3 DTI Fiber Tracking

DTI fiber tracking software was written in Interactive Data Language (Research Systems Inc., Boulder CO) and run on a SunBlade 2500 workstation (Sun Microsystems, Santa Clara CA). The streamline fiber tracking method was based on fiber assignment by continuous tracking (FACT) (25). The algorithm computes a 3D trajectory in continuous space beginning from a user-defined starting region. Each voxel in the starting region is densely seeded with 27 equally spaced starting points arranged in a 3 x 3 x 3 grid and track trajectories follow the principal eigenvectors. When the 3D fiber track trajectory enters a neighboring voxel, the fiber track's direction is altered to match the direction of the new voxel's primary eigenvector. The 3D fiber track is allowed to continue from voxel to voxel until it enters a region of fractional anisotropy less than 0.024, turns an angle greater than 50 degrees between two consecutive voxels, or exits the brain.

In addition to the streamline deterministic FACT algorithm, fiber tracking based on FACT but using a probabilistic index of connectivity (PICO) was performed (29). The probabilistic method generates fiber trajectories in the same way as

the FACT method, except a Monte Carlo method is used while the direction of the primary eigenvectors is randomly toggled. When using the probabilistic fiber tracking method, 512 trajectories were launched from the center of each voxel in the starting region. Each trajectory can have a unique path because the primary eigenvectors of each voxel in the brain are perturbed by angles randomly selected from probability distributions based on the voxels' fractional anisotropies. The number of resultant fiber tracks passing through a voxel provides a confidence metric of the voxel's inclusion in a delineated pathway.

Tracks were launched from a starting region encompassing the posterior limb and the retrolenticular segment of the internal capsules (Figure 9-1). This region is known to encompass both the pyramidal tract and somatosensory radiation. Resultant fiber tracks were segmented into motor and somatosensory components using two target regions placed near the brain's vertex drawn in the precentral and postcentral gyri, respectively. Fiber tracks originating in the starting region and passing through the precentral or postcentral gyrus were defined as motor or sensory tracks, respectively. Fiber tracks not reaching either of the target regions were excluded.

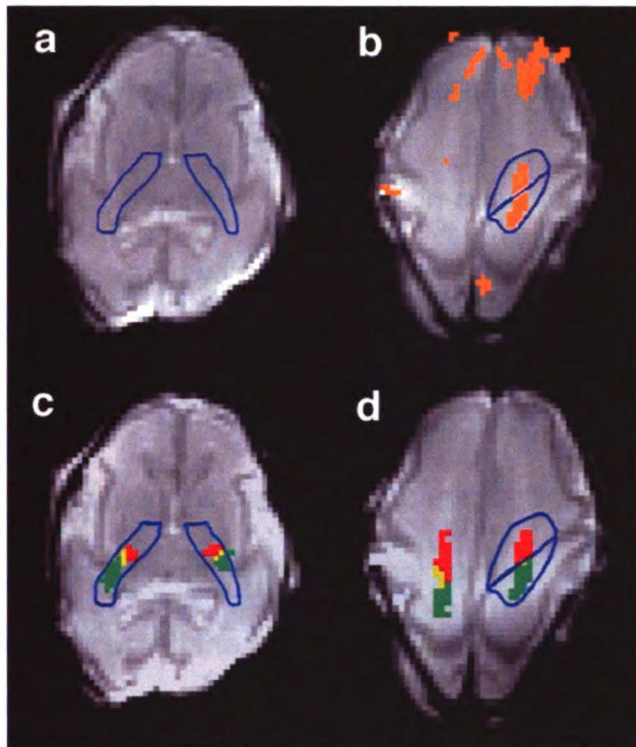


Figure 9-1: a) Starting regions for DTI fiber tracking shown for a 29 week GA premature infant in the posterior limb and retrolenticular segments of the internal capsule. b) Fiber tracks from the left starting region (orange) are segmented into motor and sensory tracks using regions drawn in the pre and post-central gyri, respectively. The central sulcus is used to guide placement of segmentation regions. c) Axial cross section of segmented motor (red) and sensory (green) fiber tracks at the level of the internal capsule. Voxels containing both motor and sensory fiber tracks are yellow. d) Motor and sensory fiber tracks near the vertex of the brain.

Fractional anisotropy, D_{av} , and the three eigenvalues (λ_1 , λ_2 , λ_3) were measured on a slice-by-slice basis, based on voxels through which the fiber tracks passed (12). Measurements from the left and right sides of the brain were averaged for both the sensory and motor tracks. Overlapping voxels containing both motor and sensory DTI tracks were included in each tract's measurements. The measurements reported were a weighted average with the number of tracks passing through a voxel comprising the weight for each voxel. Thus, voxels with

few fiber tracks were considered least likely to be within the tract of interest and contributed least to the measurements.

A slice-by-slice plot of region-specific measures along the delineated pathway was created with the diffusion parameter measurements obtained at each level. The 3D tract-specific measures of FA, D_{av} , λ_1 , and transverse diffusion were obtained by averaging the slice-specific data along the internal capsule and centrum semiovale. An experienced pediatric neuroradiologist determined axial levels containing the internal capsule and white matter of the centrum semiovale subjacent to the sensorimotor cortex that were consistent across all subjects.

A mixed random-effects analysis of the tract-specific measurements was used to identify gestational age related trends, differences between the motor and sensory tracts, and the effect of the fiber tracking algorithm on measurements (20). The mixed random-effect analysis included measurements from all 37 scans and controlled for the 10 subjects scanned twice. A p-value of less than 0.05 was considered significant.

9.4 Results

DTI fiber tracks were generated in each of 37 MR examinations included in the study. Figure 9-2 shows axial overlays of motor and somatosensory DTI fiber tracks generated with the deterministic FACT algorithm in a 29 week GA neonate. The delineated motor pathways course from the internal capsule, through the centrum semiovale to the precentral gyrus. The tracked sensory

pathways are posterior to the motor tracks and course through the internal capsule, centrum semiovale, and post-central gyrus. Figure 9-3 shows axial overlays of the motor pathway generated with probabilistic DTI fiber tracking using the PICO algorithm. The delineated neuronal pathway is color-coded based on the number of fiber tracks passing through each voxel. The connectivity confidence peaks in the center of the region containing fiber tracks.

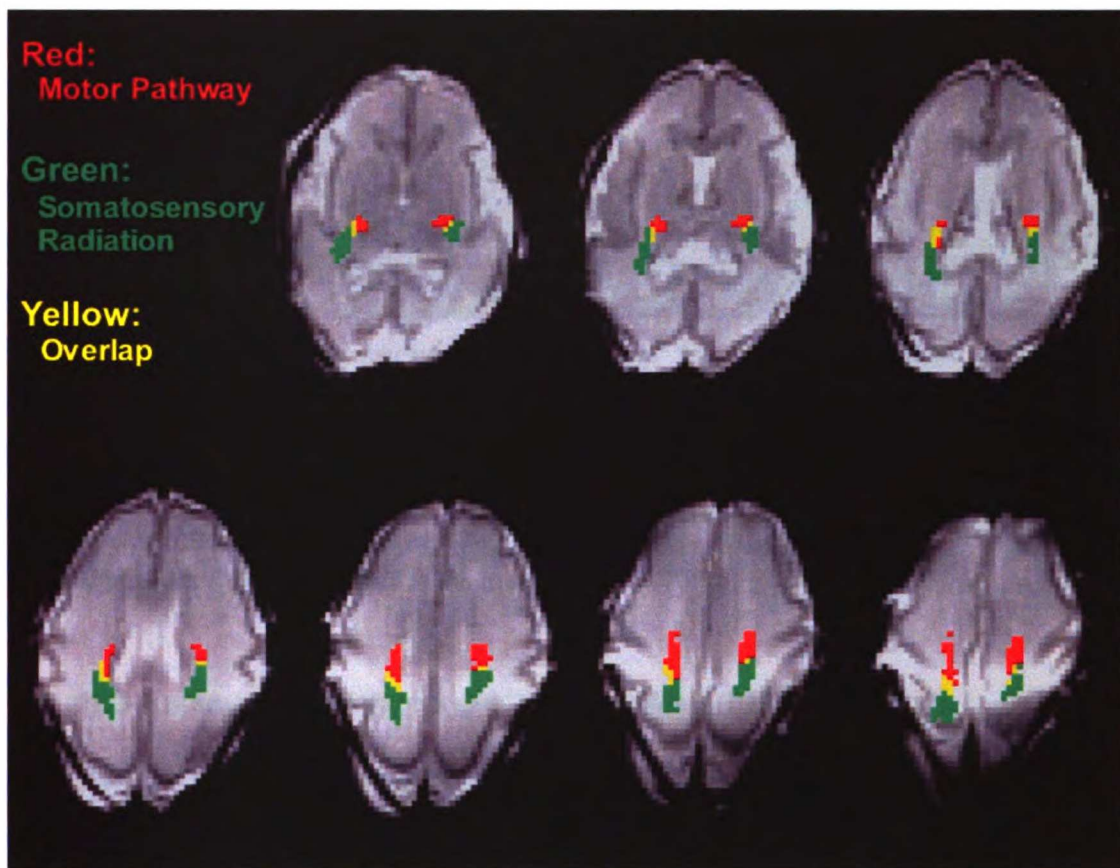


Figure 9-2: Axial cross sections of DTI fiber tracks in a preterm infant born at 27 weeks GA and studied at an age of 29 weeks GA. Fiber tracks were generated with the deterministic streamline algorithm. The motor pathway (red) and somatosensory radiation (green) are shown from the level of the internal capsule to the vertex of the brain. Voxels containing both motor and sensory fiber tracks are colored yellow.

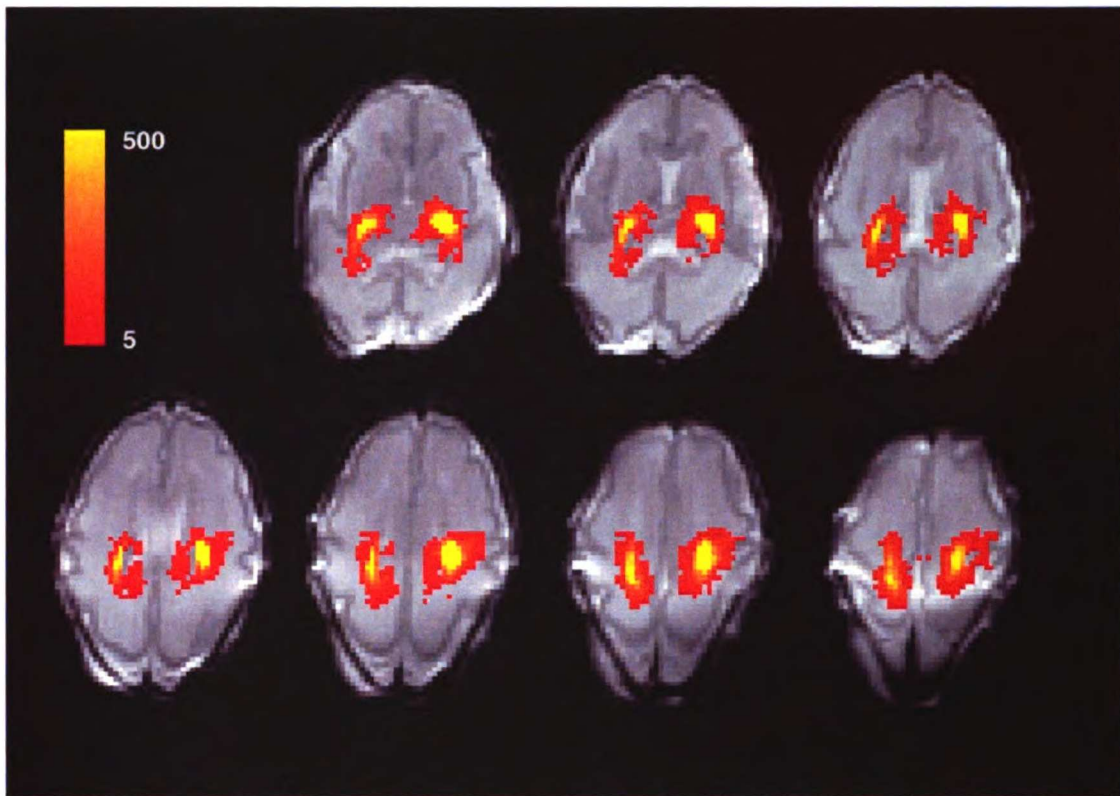


Figure 9-3: Axial cross sections of DTI fiber tracks of the motor pathway in a preterm infant born at 27 weeks GA and studied at 29 weeks GA. Fiber tracks were generated with the probabilistic streamline algorithm. The motor pathway is shown from the level of the internal capsule to the vertex of the brain. Voxels are color coded according to the number of fiber tracks passing through each voxel. Yellow indicates the greatest density of fiber tracks and thus the regions of greatest localization confidence.

Figure 9-4 shows a 3D rendering of motor and sensory fiber tracks in a 37 week GA infant. The head is cut away at the level of the internal capsule. Fiber tracks are seen to occupy a smaller cross-sectional area in the internal capsule than in the corona radiata. The motor and somatosensory pathways are known to occupy a larger volume as they spread in the corona radiata.

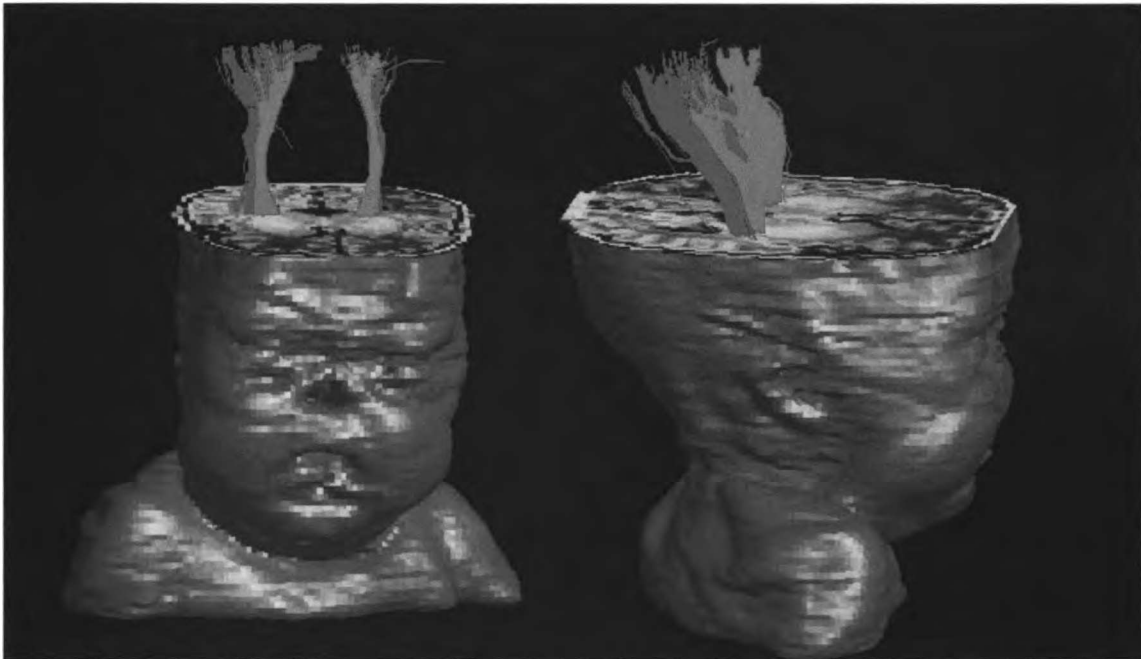


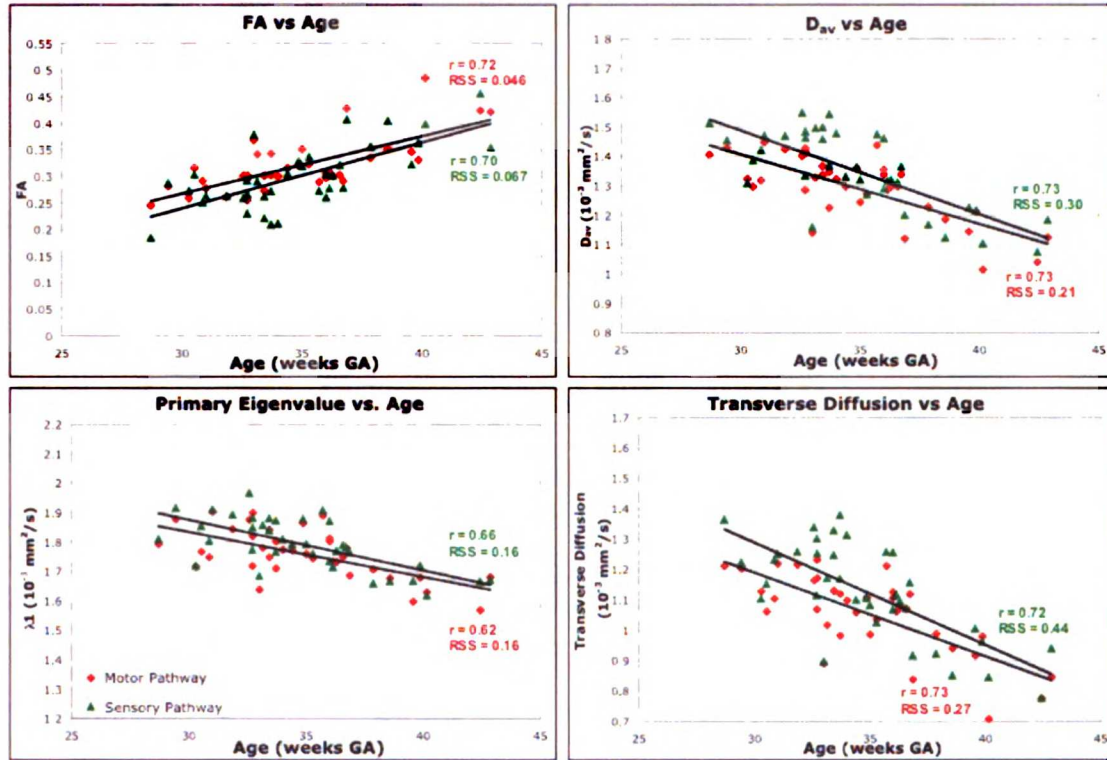
Figure 9-4: 3D rendering of DTI fiber tracks and infant head for a 37 week GA premature infant. Motor tracks (red) are anterior to the sensory (green) fiber tracks. The head and brain are sliced at the level of the internal capsule. The elongation of the brain and skull common in premature newborns is evident in the 3D rendering.

9.4.1 Tract-Specific Measurements

Tract-specific measurements from 3D regions defined by fiber tracks generated with the deterministic FACT (Figure 9-5) and probabilistic PICO (Figure 9-6) algorithms are shown as a function of age. FA, D_{av} , λ_1 , and transverse diffusion in both the motor and sensory pathways were significantly correlated with age (see figures for p-values). FA in the motor and somatosensory tract significantly increased with age in measurements derived from both deterministic and probabilistic fiber tracking. The primary eigenvalue λ_1 , D_{av} , and transverse diffusion each significantly decreased with increasing age in the motor and somatosensory pathways as measured with both fiber tracking methods.

Transverse diffusion decreased with age at a significantly higher rate than λ_1 ($p < 0.0001$).

Deterministic Fiber Tracking Measurements



Differences between motor and sensory tract measurements

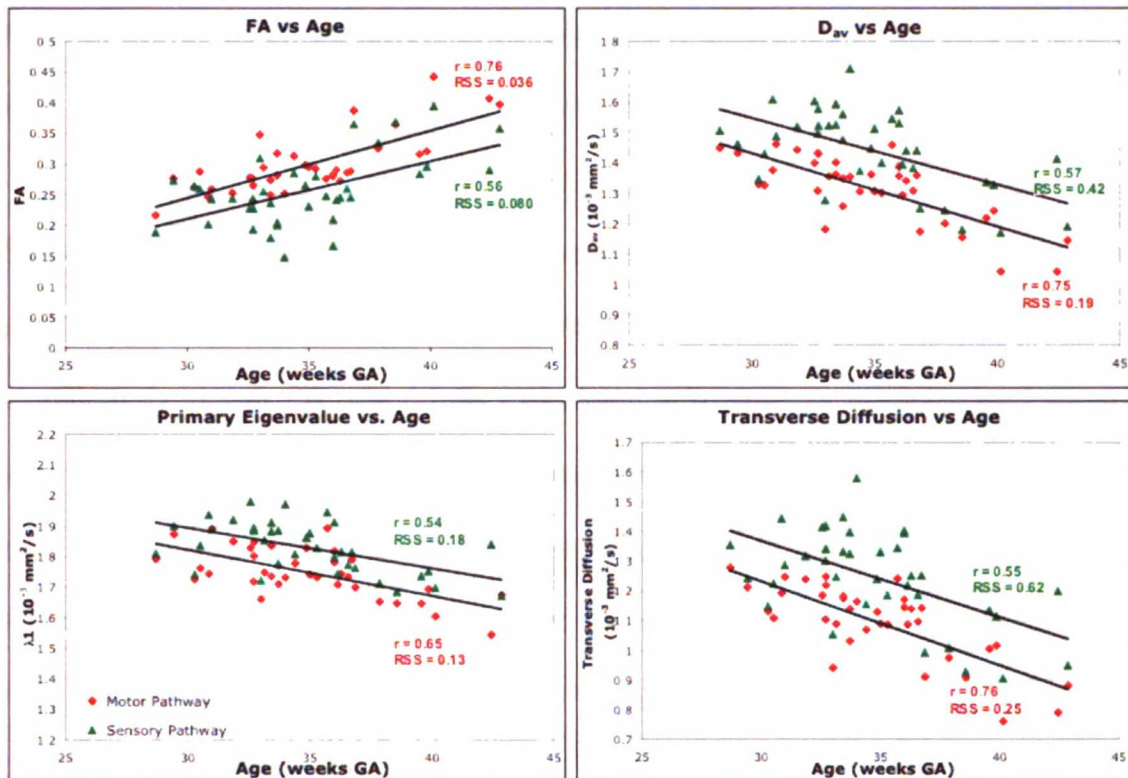
FA	$p < 0.0001$	D_{av}	$p < 0.014$
λ_1	$p < 0.021$	Trans. Diffusion	$p < 0.018$

Test for parameter correlation with age

FA motor	$p < 0.0001$	D_{av} motor	$p < 0.0001$
sensory	$p < 0.0001$	sensory	$p < 0.0001$
λ_1 motor	$p < 0.0001$	Trans. Diffusion motor	$p < 0.0001$
sensory	$p < 0.0001$	sensory	$p < 0.0001$

Figure 9-5: 3D tract-specific measurements of FA, D_{av} , primary eigenvalue, and transverse diffusion are plotted vs age. Measurements were based on a 3D region delineated by fiber tracking between the internal capsule and centrum semiovale. Measurements and statistics from deterministic fiber tracking using the FACT algorithm are shown. The correlation coefficient (r) and residual sum of squares (RSS) are shown for each plot.

Probabilistic Fiber Tracking Measurements



Differences between motor and sensory tract measurements

FA	p < 0.0001	D _{av}	p < 0.0001
λ ₁	p < 0.0001	Trans. Diffusion	p < 0.0001

Test for parameter correlation with age

FA	motor p < 0.0001	D _{av}	motor p < 0.0001
	sensory p < 0.0001		sensory p < 0.0001
λ ₁	motor p < 0.0001	Trans. Diffusion	motor p < 0.0001
	sensory p < 0.0001		sensory p < 0.0001

Figure 9-6: 3D tract-specific measurements of FA, D_{av}, primary eigenvalue, and transverse diffusion are plotted vs age. Measurements were based on a 3D region delineated by fiber tracking between the internal capsule and centrum semiovale. Measurements and statistics from probabilistic fiber tracking using the PICO method are shown. The correlation coefficient (r) and residual sum of squares (RSS) are shown for each plot.

Differences between motor and sensory tracts were detected with quantitative DTI fiber tracking. D_{av}, λ₁, and transverse diffusion measured with each fiber tracking method were significantly higher in the sensory pathway than those in the motor pathway. The FA measured with each fiber tracking method in the motor pathway was found to be significantly higher in the pyramidal tract than in

the somatosensory radiation (see Figure 9-5 and Figure 9-6 for p-values). For each of the diffusion parameters, no significant difference in the rate of change with age was detected between sensory and motor tracts.

Systematic differences were detected between measurements from deterministic and probabilistic fiber tracking algorithms. The deterministic algorithm produced significantly higher FA and primary eigenvalue measures in motor and sensory tracts as compared to the probabilistic method ($p < 0.0001$). Transverse diffusion and D_{av} measurements with deterministic fiber tracking were systematically lower as compared to the probabilistic method ($p < 0.0001$). No significant difference in the rate of change of diffusion parameters with age was detected between the two tracking techniques.

9.4.2 Region-Specific Measures

Figure 9-7 shows slice-by-slice measurements from 42 week and 29 week GA infants. Diffusion parameters are graphed for each slice along delineated tracks from the internal capsule to the brain vertex. FA is higher along the white matter pathways in the 42 week GA infant as compared to the 29 week GA infant. D_{av} , λ_1 , and transverse diffusion are higher along tracked white matter pathways in the younger infant. Fractional anisotropy of the motor and sensory tracts is greater in the internal capsule than in more superior portions of the tracts within the corona radiata and centrum semiovale. This pattern of maximum FA in the internal capsule was observed in all cases in this study.

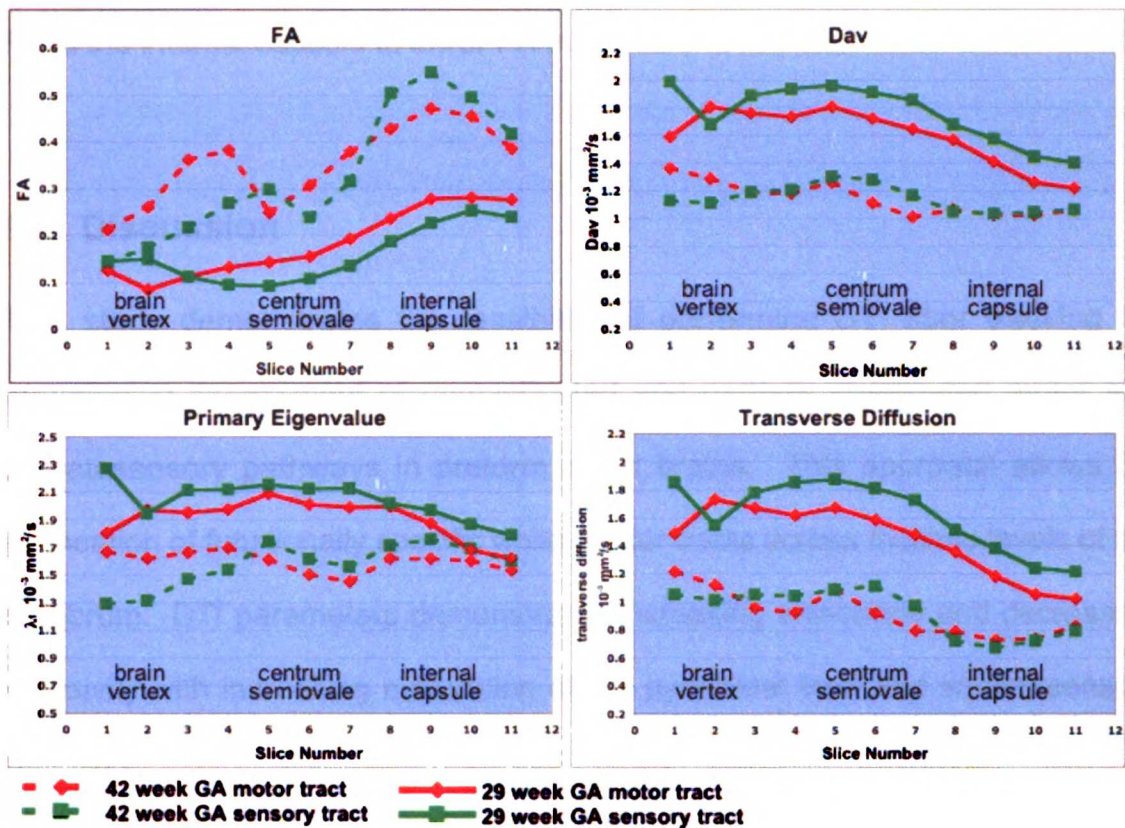


Figure 9-7: Diffusion parameters measured along the motor and sensory tracts in a 42 week GA infant born at 34 weeks GA and a 29 week GA infant born at 27 weeks GA. Plots were aligned at the centrum semiovale. FA, D_{av} , primary eigenvalue, and transverse diffusion measurements are graphed at each slice along delineated tracks from the internal capsule to the brain vertex. The 42 week GA infant exhibits higher FA than the younger 29 week GA infant in the white matter tracts of interest. All cases showed highest FA in the internal capsule and lower FA in superior portions of the tracts. A dip in FA exists in the slices spanning the centrum semiovale of the 42 week GA infant.

Slice-by-slice measurements also revealed an age related pattern of FA along the motor and sensory tracts. The older infants show a dip in FA within the centrum semiovale that is absent in the younger infants. This decrease in FA is seen in Figure 9-7 across slices 5 to 7 corresponding to the centrum semiovale.

In contradistinction, the 29 week GA infant shows a smooth transition from high FA in the internal capsule to lower FA in the corona radiata.

9.5 Discussion

This study demonstrates the feasibility of performing DTI fiber tracking for quantitative assessment of unmyelinated and partially myelinated motor and somatosensory pathways in preterm infant brains. This approach allows 3D delineation of functionally specific white matter tracts across multiple levels of the cerebrum. DTI parameters demonstrated increasing anisotropy and decreasing diffusivity with increasing maturation of the pyramidal tract and somatosensory radiation.

9.5.1 ROIs Based on DTI Fiber Tracking

DTI fiber tracking can delineate portions of an axonal pathway at levels where the tract cannot be manually outlined for region of interest analysis. The descending motor pathway is known to be located in the middle third of the cerebral peduncle and the posterior limb of the internal capsule. Similarly, the somatosensory radiation is known to pass through the internal capsule posterior to the motor tract. However, the motor tract and somatosensory radiation cannot easily be defined or differentiated from other white matter tracts on conventional MR at the level of the corona radiata or centrum semiovale. Even with the aid of DTI anisotropy maps or color overlays of the primary eigenvector, the motor and

somatosensory tracts are within a band of inferior-superior oriented pathways containing functionally unrelated tracts coursing to and from the frontal, occipital, and parietal lobes (28). DTI fiber tracking uses the orientation of axonal bundles to extend tract localization from known anatomical landmarks to regions where localization can be ambiguous.

The 3D region defined by DTI fiber tracking allows quantitative analysis of a specific functional pathway across multiple levels. Previous newborn infant studies have been limited to DTI measurements from single-slice ROIs drawn in white matter structures encompassing multiple pathways serving different functions (17, 27, 30). The 3D region does not have to conform to any particular geometric shape. The shape and position of the fiber tracks are determined by the inter-voxel connectivity inferred from the diffusion tensor. For example, the fiber tracks generated in this study were observed to spread in the corona radiata, matching the known anatomical features of the pathway.

Measurements from 3D regions defined by fiber tracking are less susceptible to variation from different scan plane orientations than 2D region of interest analysis. Depending on the patient's head position, a region drawn on a single slice can include different portions of a white matter tract. Drawing 2D regions encompassing a consistent portion of brain in multiple neonates can be especially difficult because of their small head size. DTI fiber tracking delineates a large segment of a tract without regard to the tract's orientation or geometry. In

this study, the 3D region used for measurements spanned from the internal capsule to the centrum semiovale. Head orientation does introduce variability in the anatomy included in the two endpoint slices. However, the regions delineated on the majority of slices between the internal capsule and centrum semiovale are not as dependent on head orientation.

This study restricted tract-specific measurements between the internal capsule and the centrum semiovale. The somatosensory tract emerges from the thalamus into the internal capsule, so cannot be reliably followed inferior to this level. The motor tracts could be delineated to the cerebral peduncle. However, motor tracts in the midbrain are difficult to measure with DTI fiber tracking because of the low anatomical resolution and the echo planar distortions near the skull base.

9.5.2 Measurements of Developing Sensorimotor Tracts

The tract-specific developmental changes detected in this study are consistent with prior studies using manually drawn ROIs in subregions of the 3D region delineated in this study (17, 27, 30). All three eigenvalues and D_{av} were observed to decrease with increasing age. The primary eigenvalue decreased with age at a lower rate than the transverse eigenvalues, causing FA to increase with age. The increasing FA indicates that water diffusion is becoming increasingly hindered and/or restricted perpendicular to axonal fibers. Decreasing water content in the brain cannot account for all the changes in

diffusion (10). Increasing axonal density, premyelination (34) and myelination itself are factors likely contributing to increased anisotropy and decreased diffusivity. It has been reported with animal models that increases in the primary eigenvalue and transverse diffusion are correlated with axonal injury and demyelination, respectively (31). However, myelination of the sensorimotor tract does not begin until near term age so myelin cannot entirely account for the decrease in transverse diffusion observed in the premature neonates (2, 19). In this study, transverse diffusion was observed to decrease continuously from 28 to 43 weeks gestational age.

9.5.3 Comparison of Fiber Tracking Methods

Probabilistic and deterministic fiber tracking measurements of diffusion parameters were both able to detect maturation of white matter tracts and differences between the motor and sensory tracts. However, deterministic fiber tracking produced higher FA and λ_1 and lower D_{av} and transverse diffusivity values than probabilistic fiber tracking. These systematic differences can be attributed to the differences between the two fiber tracking algorithms. The streamline FACT algorithm only propagates along the best estimate of the fiber tract's direction while probabilistic PICO algorithm propagates along alternate pathways with lower likelihoods that tend to include partial volume voxels. Thus, the PICO algorithm produces more diffuse fiber tracks that may include adjacent, less mature pathways. The PICO algorithm also includes more voxels with contributions from both motor and sensory tracts, but the accuracy of this result

is unknown. The FACT algorithm may provide a more conservative estimate of the spatial extent of the tract and be limited to the tract's core. Unfortunately, it was not feasible to assess the accuracy of each fiber tracking algorithm in a cohort of premature infants.

A probabilistic framework for fiber tracking provides more options for evaluation of tracking results and tract quantitation. The confidence metric can provide a method of adjusting the size of the 3D tract ROI used for measurement by determining which voxels to include or exclude from the tract. In this study, the confidence metric was used to calculate a weighted average for tract measurements. However, constraints on the quantification procedure within the tract ROI can either remove real parts of the tract or retain voxels outside the tract. The accuracy of measurement ROIs with different constraints is not precisely known, however, age is expected to impact the accuracy of fiber tracks. Young infants have lower FA and higher eigenvector uncertainties that may result in erroneous fiber tracks outside the pathway of interest (1, 21, 22). Older infants have more complex white matter that may introduce erroneous fiber tracks in regions with crossing fibers. These expected errors highlight the importance of combining prior anatomical information and functional data with DTI fiber tracking (7, 9, 15, 32). In this study, multiple ROIs drawn in the internal capsule, precentral gyrus, and postcentral gyrus are expected to exclude many of the erroneous fiber tracks outside the boundaries of the pathway. However,

additional work on defining the accuracy of fiber tracking is necessary to determine the optimal measurement scheme for each pathway.

9.5.4 Region Specific Characteristics

In addition to tract-specific measurements from 3D ROIs, DTI fiber tracking enables neuronal tracts to be subdivided by level for more detailed study. Quantitative analysis with DTI fiber tracking revealed a diversity of structural characteristics within motor and somatosensory pathways. Axonal bundles within the internal capsule are compact and highly ordered, resulting in the highest FA values measured along the course of the motor and somatosensory tracts. In this study, fiber tracking was able to reveal decreased FA in the corona radiata and centrum semiovale as compared to the internal capsule. Superior to the internal capsule, motor and sensory tracts in the corona radiata and centrum semiovale are characterized by more dispersed fibers, and also by the development of crossing commissural and association fibers in the brains of the older infants. Previous studies have compared the FA in the centrum semiovale and the internal capsule; however, DTI fiber tracking can reveal the transition of FA values between these two regions (30).

The maturity of crossing fibers in the centrum semiovale was detected with a dip in tract FA in the older newborns (Figure 9-7). The presence of crossing fibers was confirmed with color overlays of the primary eigenvector showing longitudinal, association, and commissural pathways (Figure 9-8).

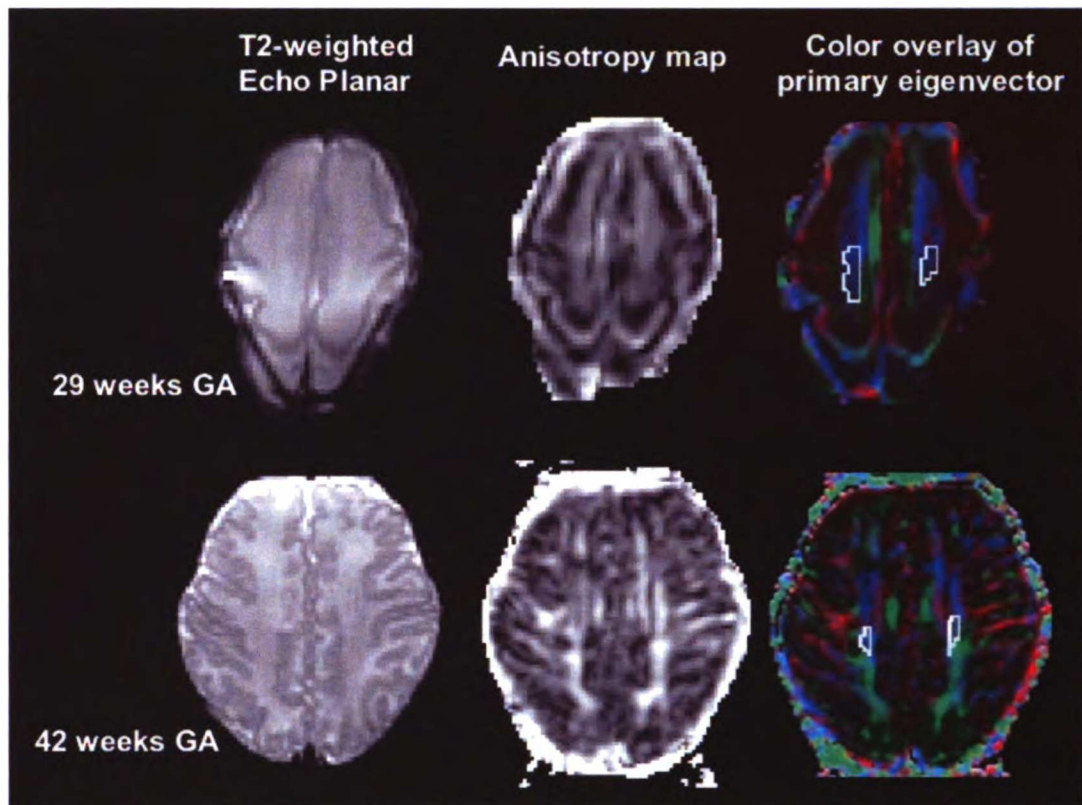


Figure 9-8: White matter complexity increases between 29 weeks and 42 weeks GA. The $b=0$ s/mm² echo planar image, fractional anisotropy map, and primary eigenvector color overlay map are shown for two infants at the level of the centrum semiovale. Delineated motor tracks are outlined in white on the color overlay maps. The 42-week GA infant has more cortical convolutions and association fibers. These later-developing neuronal fibers intersect the descending motor pathway at the level of the centrum semiovale, creating more complex white matter architecture than in the 29-week GA infant.

Subvoxel fiber populations of different orientations are averaged and decrease the anisotropy values measured by DTI in the motor and sensory pathways at the level of the centrum semiovale. The intersection of pathways such as the corpus callosum, pyramidal tract, and superior longitudinal fasciculus at the centrum semiovale has previously been observed in adults as a possible obstacle to DTI fiber tracking (7). Diffusion MR techniques with more than 6 diffusion gradient

directions have been able to reveal the multiple intravoxel neuronal pathways in the centrum semiovale (33).

9.6 Conclusion

In conclusion, this quantitative investigation using both deterministic and probabilistic DTI fiber tractography characterized the age-related trends in spatially-averaged diffusivity, fractional anisotropy, and the 3 diffusion tensor eigenvalues for preterm white matter development in the pyramidal tracts and somatosensory radiations. This study included analysis over the entire 3D volume of these tracts within the cerebral hemispheres, as well as regional analysis by axial level along the craniocaudal course of these sensorimotor pathways. These DTI fiber tracking techniques can be used to further investigate the relationship between white matter injury and subsequent motor and sensory impairments. Further research is ongoing to determine whether quantitative DTI fiber tractography may be superior to conventional MR imaging for the early detection of white matter injury of prematurity, and for predicting the neurodevelopmental outcome of infants born prematurely.

9.7 References

1. Anderson AW: Theoretical analysis of the effects of noise on diffusion tensor imaging. **Magn Reson Med** 46:1174-1188, 2001.
2. Barkovich AJ: Concepts of myelin and myelination in neuroradiology. **AJNR Am J Neuroradiol** 21:1099-1109, 2000.
3. Basser PJ, Mattiello J, LeBihan D: Estimation of the effective self-diffusion tensor from the NMR spin echo. **J Magn Reson B** 103:247-254, 1994.

4. Basser PJ, Pajevic S, Pierpaoli C, Duda J, Aldroubi A: In vivo fiber tractography using DT-MRI data. **Magn Reson Med** 44:625-632, 2000.
5. Basser PJ, Pierpaoli C: Microstructural and physiological features of tissues elucidated by quantitative-diffusion-tensor MRI. **Journal of Magnetic Resonance Series B** 111:209-219, 1996.
6. Beaulieu C, Allen PS: Determinants of anisotropic water diffusion in nerves. **Magn Reson Med** 31:394-400, 1994.
7. Berman JI, Berger MS, Mukherjee P, Henry RG: Diffusion-tensor imaging-guided tracking of fibers of the pyramidal tract combined with intraoperative cortical stimulation mapping in patients with gliomas. **J Neurosurg** 101:66-72, 2004.
8. Berman JI, Mukherjee P, Partridge SC, Miller SP, Ferriero DM, Barkovich AJ, Vigneron DB, Henry RG: Quantitative diffusion tensor MRI fiber tractography of sensorimotor white matter development in premature infants. **NeuroImage** 27:862-871, 2005.
9. Conturo TE, Lori NF, Cull TS, Akbudak E, Snyder AZ, Shimony JS, McKinstry RC, Burton H, Raichle ME: Tracking neuronal fiber pathways in the living human brain. **Proc Natl Acad Sci U S A** 96:10422-10427, 1999.
10. Dobbing J, Sands J: Quantitative growth and development of human brain. **Arch Dis Child** 48:757-767, 1973.
11. Dumoulin CL, Rohling KW, Piel JE, Rossi CJ, Giaquinto RO, Watkins RD, Vigneron DB, Barkovich AJ, Newton N: Magnetic resonance imaging compatible neonate incubator. **Magn. Reson. Engineering** 15:117-128, 2002.
12. Glenn OA, Henry RG, Berman JI, Chang PC, Miller SP, Vigneron DB, Barkovich AJ: DTI-based three-dimensional tractography detects differences in the pyramidal tracts of infants and children with congenital hemiparesis. **Journal of Magnetic Resonance Imaging** 18:641-648, 2003.
13. Gossel C, Fahrmeir L, Putz B, Auer LM, Auer DP: Fiber tracking from DTI using linear state space models: detectability of the pyramidal tract. **Neuroimage** 16:378-388, 2002.
14. Gudbjartsson H, Patz S: The Rician distribution of noisy MRI data. **Magn Reson Med** 34:910-914, 1995.
15. Guye M, Parker GJ, Symms M, Boulby P, Wheeler-Kingshott CA, Salek-Haddadi A, Barker GJ, Duncan JS: Combined functional MRI and tractography to demonstrate the connectivity of the human primary motor cortex in vivo. **Neuroimage** 19:1349-1360, 2003.
16. Hoon AH, Lawrie WT, Melhem ER, Reinhardt EM, van Zijl PCM, Solaiyappan M, Jiang H, Johnston MV, Mori S: Diffusion tensor imaging of periventricular leukomalacia shows affected sensory cortex white matter pathways. **Neurology** 59:752-756, 2002.
17. Huppi PS, Maier SE, Peled S, Zientara GP, Barnes PD, Jolesz FA, Volpe JJ: Microstructural development of human newborn cerebral white matter assessed in vivo by diffusion tensor magnetic resonance imaging. **Pediatr Res** 44:584-590, 1998.

18. Huppi PS, Murphy B, Maier SE, Zientara GP, Inder TE, Barnes PD, Kikinis R, Jolesz FA, Volpe JJ: Microstructural brain development after perinatal cerebral white matter injury assessed by diffusion tensor magnetic resonance imaging. **Pediatrics** 107:455-460, 2001.
19. Kinney HC, Karthigasan J, Borenshteyn NI, Flax JD, Kirschner DA: Myelination in the developing human brain: biochemical correlates. **Neurochem Res** 19:983-996, 1994.
20. Laird NM, Ware JH: Random-effects models for longitudinal data. **Biometrics** 38:963-974, 1982.
21. Lazar M, Alexander AL: An error analysis of white matter tractography methods: synthetic diffusion tensor field simulations. **NeuroImage** 20:1140-1153, 2003.
22. Lori NF, Akbudak E, Shimony JS, Cull TS, Snyder AZ, Guillory RK, Conturo TE: Diffusion tensor fiber tracking of human brain connectivity: acquisition methods, reliability analysis and biological results. **NMR Biomed** 15:494-515, 2002.
23. Miller SP, Vigneron DB, Henry RG, Bohland MA, Ceppi-Cozzio C, Hoffman C, Newton N, Partridge JC, Ferriero DM, Barkovich AJ: Serial quantitative diffusion tensor MRI of the premature brain: Development in newborns with and without injury. **Journal of Magnetic Resonance Imaging** 16:621-632, 2002.
24. Miller SP, Vigneron DB, Henry RG, Bohland MA, Ceppi-Cozzio C, Hoffman C, Newton N, Partridge JC, Ferriero DM, Barkovich AJ: Serial quantitative diffusion tensor MRI of the premature brain: development in newborns with and without injury. **J Magn Reson Imaging** 16:621-632, 2002.
25. Mori S, Crain BJ, Chacko VP, van Zijl PC: Three-dimensional tracking of axonal projections in the brain by magnetic resonance imaging. **Ann Neurol** 45:265-269, 1999.
26. Mukherjee P, Miller JH, Shimony JS, Conturo TE, Lee BCP, Almlı CR, McKinstry RC: Normal Brain Maturation during Childhood: Developmental Trends Characterized with Diffusion-Tensor MR Imaging. **Radiology** 221:349-358, 2001.
27. Neil JJ, Shiran SI, McKinstry RC, Schefft GL, Snyder AZ, Almlı CR, Akbudak E, Aronovitz JA, Miller JP, Lee BC, Conturo TE: Normal brain in human newborns: apparent diffusion coefficient and diffusion anisotropy measured by using diffusion tensor MR imaging. **Radiology** 209:57-66, 1998.
28. Pajevic S, Pierpaoli C: Color schemes to represent the orientation of anisotropic tissues from diffusion tensor data: application to white matter fiber tract mapping in the human brain. **Magn Reson Med** 42:526-540, 1999.
29. Parker GJ, Haroon HA, Wheeler-Kingshott CA: A framework for a streamline-based probabilistic index of connectivity (PICO) using a structural interpretation of MRI diffusion measurements. **J Magn Reson Imaging** 18:242-254, 2003.

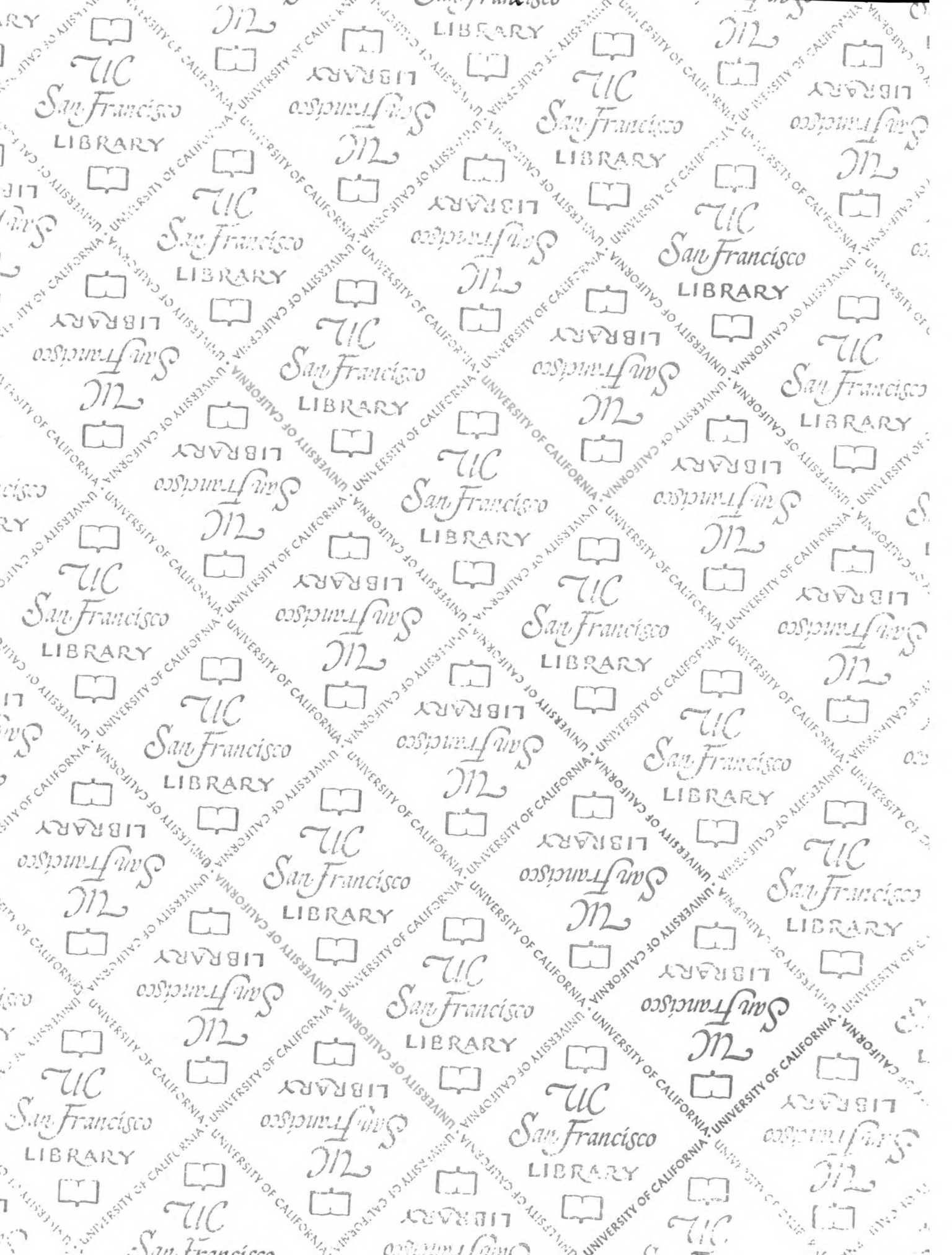
30. Partridge SC, Mukherjee P, Henry RG, Miller SP, Berman JI, Jin H, Lu Y, Glenn OA, Ferriero DM, Barkovich AJ, Vigneron DB: Diffusion tensor imaging: serial quantitation of white matter tract maturity in premature newborns. **NeuroImage** 22:1302-1314, 2004.
31. Song SK, Sun SW, Ju WK, Lin SJ, Cross AH, Neufeld AH: Diffusion tensor imaging detects and differentiates axon and myelin degeneration in mouse optic nerve after retinal ischemia. **NeuroImage** 20:1714-1722, 2003.
32. Toosy AT, Ciccarelli O, Parker GJ, Wheeler-Kingshott CA, Miller DH, Thompson AJ: Characterizing function-structure relationships in the human visual system with functional MRI and diffusion tensor imaging. **NeuroImage** 21:1452-1463, 2004.
33. Tuch DS, Reese TG, Wiegell MR, Wedeen VJ: Diffusion MRI of complex neural architecture. **Neuron** 40:885-895, 2003.
34. Wimberger DM, Roberts TP, Barkovich AJ, Prayer LM, Moseley ME, Kucharczyk J: Identification of "premyelination" by diffusion-weighted MRI. **J Comput Assist Tomogr** 19:28-33, 1995.
35. Woods RP, Grafton ST, Holmes CJ, Cherry SR, Mazziotta JC: Automated image registration: I. General methods and intrasubject, intramodality validation. **Journal of Computer Assisted Tomography** 22:139-152, 1998.
36. Woods RP, Grafton ST, Watson JDG, Sicotte NL, Mazziotta JC: Automated image registration: II. Intersubject validation of linear and nonlinear models. **Journal of Computer Assisted Tomography** 22:153-165, 1998.

Chapter 10: Main Findings and Conclusions

This thesis project investigated novel DTI fiber tracking protocols to assess their capabilities and clinical applications in patient populations. The project was completed in three successive parts. The first part of this project involved developing DTI fiber tracking and bootstrap analysis tools for feasibility studies. The quantitative fiber tracking tools were found to be sensitive enough to detect damage to motor tracts in patients with congenital hemiplegia. The second part of this project sought to validate DTI fiber tracking by correlating the technique with intraoperative stimulation, the gold-standard for functional localization. These validation studies were necessary before DTI fiber tracking can be relied upon for clinical applications and surgical planning. For the third and final part of the project, DTI fiber tracking was transitioned into a clinical tool for planning tumor resections and investigating newborn brain development. As a result of this thesis project, DTI fiber tracking is now routinely ordered at UCSF prior to resection of tumors close to the motor pathway. DTI fiber tracking was also used to perform a detailed, tract-specific examination of maturing white matter pathways in the preterm infant brain.

This thesis project has shown the value of DTI fiber tracking as a non-invasive tool for studying the human brain. Fiber tracking is a unique scientific tool because it bridges the gap between functional mapping techniques and traditional anatomical MR images. Future advances in diffusion MR will address

the limitations of current methods. The assumption that the DTI ellipsoid reflects the underlying axonal structure is not always true. Higher field strengths, larger gradients, and diffusion models beyond the tensor will close the gap between MR measurement and biological reality. Improved fiber tracking methods will lead to additional scientific and clinical applications.



7486833



3 1378 00748 6833

For reference

Not to be taken
from the room.

